

# Detection of Exoplanets with Spectral Observations of SPHERE/IFS

An Analysis and Expansion of Direct and Differential  
Imaging Techniques

**David PETIT**

Supervisor: Dr. Maddalena Reggiani  
Affiliation *KU Leuven*

Cosupervisor: *Sven Kiefer*  
Affiliation *KU Leuven, OEAW IWF,  
TU Graz*

Master thesis submitted in fulfillment of  
the requirements for the degree in Master  
of Science in Astronomy & Astrophysics

Academic Year 2022-2023

© Copyright by KU Leuven

Without written permission of the promoters and the authors it is forbidden to reproduce or adapt in any form or by any means any part of this publication. Requests for obtaining the right to reproduce or utilize parts of this publication should be addressed to KU Leuven, Faculteit Wetenschappen, Geel Huis, Kasteelpark Arenberg 11 bus 2100, 3001 Leuven (Heverlee), Telephone +32 16 32 14 01. A written permission of the promoter is also required to use the methods, products, schematics and programs described in this work for industrial or commercial use, and for submitting this publication in scientific contests.

# Preface

My most earnest, grateful, and sincere thank you goes out to my supervisors, Dr. Maddalena Reggiani and Sven Keifer. Their indefatigable efforts to teach me basic concepts on scientific inquiry have yielded a mind that can now perform such research.

I would like to extend a wholehearted thank you to the professors and supervisors who helped me both in understanding a variety of complex astrophysical phenomena, as well as in the attempts at obtaining scholarships, academic workshop attendances, and doctoral programs. Thank you Professors Alex de Koter, Conny Aerts, and Dr. Timothy Van Reeth. Additional thank-yous for the rest of the Institute of Astronomy faculty & staff who, often behind the scenes, made the implementation of the curriculum possible with their humble efforts.

A profound appreciation goes out to the KU Leuven masters student selection committee or chair. My background has been in Chemical Engineering, Economics, and Education; and it was a gamble for those who allowed me to come here and study. I guarantee this educational investment will provide broad and deep changes in the academic astronomy world and beyond. To any and all that were involved in such decisions, thank you.

I end this preface with quotes that have served to inspire me to go beyond the socially-sanctioned realms of legitimacy and hope that they may continue their work:

"Those who say, do not know; those who know, do not say" -Lao Tsu

"...there is as yet nothing found to take its place. The profit-and-loss philosophy of utilitarians & materialists finds favour among logic-choppers with half a soul." -Inazo Nitobe

"...and based on a tremendously alienating instrumentality, that's what science depends on now." -Terence McKenna

"From the bathtub, to the bathtub, I have uttered stuff and nonsense." -Anonymous

"The ultimate, hidden truth of the world is that it is something that we make, and could just as easily make differently." -David Graeber

# Summary

**Background:** A master thesis research project was conducted from 2021 to 2022 on improving the data reduction techniques used in the direct imaging of exoplanets.

**Goals:** The research conducted during this master's thesis provided the opportunity for the researcher to learn the flow of professional academic research endeavors in general, and become an expert on direct imaging of exoplanets to a master's degree level in particular.

**Methods:** This work has also allowed the growth and flourishing of a familiarity of particular science and software coming from:

- European Southern Observatory (ESO)
- Spectro-Polarimetric High-contrast Exoplanet REsearch (SPHERE)
- Atacama Large Millimeter Array (ALMA) data archive
- ESO Science Archive Facility's raw data
- Very Large Telescope (VLT)
- Numerous libraries in python
- ESOReflex
- PynPoint
- Shell scripting

The workflow of this research started by obtaining data taken with the SPHERE instrument at the VLT in Chile from the ESO data archive. This was accomplished with shell scripts and ESO Reflex. PynPoint was used to reduce the obtained data. Python was then used for a thorough analysis of the data. The ALMA archive was used as an aside to the main body of this research to complement the specialized knowledge acquired in the bulk of the work.

**Results:** With such tools at the disposal, various relationships between Principal Component Analysis (PCA) and the optimal wavelength detectors have been compared. This has allowed for optimal signal-to-noise ratios to be determined for different observations made of one star. The relationships between signal-to-noise have been compared for each of the wavelengths available in the data over multiple direct images and their regimes of: Coronagraphic speckle noise, planetary detection, and (distant) background noise. Initial attempts at negating the data reduction pipeline's automatic signal suppression artifact have been made; no definitive conclusions have been drawn from this line of research, but there is evidence that future work in this area might draw out useful parameters that could minimize the suppressive artifact and allow for smaller and more sensitive exoplanet detections. Lastly, the evolutions of wavelengths over planet position are analyzed with curve fitting models; patterns in the models' variations are regressed to make linear and polynomial models of the observed planet position's evolution; an error analysis is provided for the uncertainty of such models and regressions.

**Conclusion:** There are unique PCA combinations that yield optimal detection parameters. Mitigation of a suppressive data reduction artifact appears to be another worthwhile path of research that can be pursued with more time. The behavior of the movement or migration of the artifact can be well modeled in the case of clear observations, partially modeled in the case of semi-clear observations, and appears to be unmodelable in the case of obscured observations.

# Summary for general audiences

With clear skies and good timing, you can see five nearby planets at night; and yet we are aware of about 5000 more planets today (and the number keeps growing). Most of them are far away and require large telescopes to observe; even then we can often only infer their existence from indirect ways of seeing. This thesis is about the far away planets that are bright enough to actually be seen directly with modern technology.

Optical and telescopic technology is coupled with software and computational coding to make the best images. Here, we have investigated how different techniques of manipulating data obtained from the SPHERE telescope in Chile can lead to better and stronger seeing of a distant planet going around its host star.

The techniques used in this research are Angular Differential Imaging (ADI), Spectral Differential Imaging (SDI), Angular-Spectral Differential Imaging (ASDI), Spectral-Angular Differential Imaging (SADI), and Combined Differential Imaging (CODI). All of these can be coupled with Principal Component Analysis (PCA) which can help further simplify and reduce the large amount of data available.

ADI happens after a telescope tracks and captures multiple images of a star over a duration of time. It is the subtracting from each image the average of all images, and then the rotating and stacking of the differential images so that an exoplanet is located at the same place in those images (this is possible due to the Altitude-Azimuth mount that rotates SPHERE during its tracking and observations).

SDI is a similar process, where each of the (39) wavelengths images (except the largest) are expanded to the size of the largest; cropping away the outside portion of the smaller wavelength images allows for the creation of a standard or base image. This base image is then resized to each observed image and then subtracted out to leave the planet on the same spot in the new images.

ASDI is performing the methods of ADI followed by SDI on a set of observed images, while SADI is the same in reverse order. CODI is performing the two methods of ADI and SDI simultaneously on the observation's data.

Though the results are best seen graphically and require more than a few words to describe accurately, we can generalize or simplify the results by saying that using more complex data reduction tools (ASDI, SADI, and CODI) allows for better contrast between a host star and its observed exoplanet. This is further improved by the use of small, but not unary PCAs in the various reductions.

# List of Figures

1.1	Exoplanet Detections Over Time. Figure Credit: [NASA, 2022] . . . . .	1
1.2	Exoplanet Distribution on Mass and Period. Figure Credit: [NASA, 2022] . . .	3
1.3	Distributions of Exoplanets Plotted on Various Parameters. The <i>top left</i> plot shows radii on mass, with different material references (water, rock, iron). The <i>top right</i> plot shows radii on period for five detection methods. The <i>bottom left</i> plot shows irradiation on period for five detection methods. The <i>bottom right</i> plot shows radii on temperature; the inset zooms in on the planets with earth-like radius and temperature. Figure Credit: [NASA, 2022] . . . . .	4
1.4	Exoplanet regimes, based on mass and radius. Figure Credit: [Chen and Kipping, 2017] . . . . .	5
1.5	Diagram of the Radial Velocity method of exoplanetary detection. Figure Credit: [Ollivier et al., 2009] . . . . .	5
1.6	Fractions of detection methods that contributed to known planet discoveries from 1995-2018. Figure Credit: [Deeg and Alonso, 2018] . . . . .	6
1.7	Diagram of the Transits method of exoplanetary detection. Figure Credit: [Ollivier et al., 2009] . . . . .	7
1.8	Astrometric trajectory of motion in combination with the apparent motion and orbit of the earth. The system is at a distance of $d = 50$ parsecs, orbits with eccentricity $e = 0.2$ , and semi-major axis $a = 0.6 AU$ , and has a planet of mass $m = 15M_J$ , and a proper motion of $v = 50$ milliarcseconds $\cdot yr^{-1}$ . Figure Credit: [Perryman, 2018] . . . . .	8
1.9	Astrometric motion of (star) GJ 676A believed to be from a planet orbiting in a plane near-perpendicular to our line of sight. Measurements are black dots, the calculated orbit is a large black ellipse, the gray dashed lines connect to gray dots at the best planetary locations in time. Figure Credit: [Malbet and Sozzetti, 2018] . . . . .	9
1.10	Astrometric motion of the sun from a distance of 10 parsecs. There are thousands of celestial bodies within this distance [Reylé et al., 2021]; and any observer (looking at the solar system face-on) would see this much (or more, if closer) astrometric motion. Figure Credit: [Ollivier et al., 2009] . . . . .	9
1.11	Pulsar Timing Method of exoplanet detection. Radio emissions are rapidly rotated. The emission can be observed if the sweeping beam comes in contact with our detectors. Figure Credit: [Ollivier et al., 2009] . . . . .	10

1.12	Gravitation Lensing Diagram: Deviation of a light ray from the gravity of a massive body. The diagram simplifies the more complex behavior that would be exhibited in a curving light ray into a discretely redirected light ray; this is a reasonable approximation to make if the distances between the source, lens, and observer are far apart (with respect to the speed and travel time of light) Figure Credit: [Batista, 2018]. . . . .	11
2.1	Diagram of the Spectro-Polarimetric High-contrast Exoplanet REsearch (SPHERE). Figure Credit: [European Southern Observatory, 2021b] . . . . .	15
2.2	Diagram of the Integral Field Spectrograph (IFS) on SPHERE. Figure Credit: [European Southern Observatory, 2021b] . . . . .	15
2.3	Illustration of the development of phase distortion in light propagating through the atmosphere. Figure Credit: [Surdej, 2021] . . . . .	17
2.4	Block diagram of a simple AO system. Light from a reference source, such as a star, bounces off a deformable mirror and a portion enters a wavefront sensor. This control system generates a correction signal which moves the deformable mirror, reducing the error. The light leaving the deformable mirror is refocused onto a detector or science camera. Figure Credit: David Carter, Liverpool John Mores University [Carrasco, 2009]. . . . .	17
2.5	The right panel shows an image of the starburst galaxy NGC7469 taken in natural seeing (top) and with adaptive optics (bottom). The left panel shows the image of a star with and without AO. Figure Credit: Canada-France-Hawaii Telescope, [Graham, 2022] . . . . .	18
2.6	The ESO Raw Data Archive Database Portal. Currently, check-marked boxes indicate the type of data that was obtained for the use of this thesis. Figure Credit: European Southern Observatory [2021b] . . . . .	19
2.7	Rotation of viewing perspective of altitude-azimuth (Alt-Az) telescopes, which is caused by the apparent motion of the earth. Long-term viewing for small objects (stars) in the center of the field of view is a standard practice. Peripheral objects (exoplanets) appear to rotate around their stars from earth throughout the observational time. Figure Credit: [Gómez, 2016] and Christian Thalmann . . . . .	20
2.8	ADI descriptive diagram. The telescope and detector capture images $A_i$ . An average image from all $A_i$ forms image B. Each Image $A_i$ is subtracted by the B image, which forms $C_i$ . $C_i$ images are de-rotated an amount proportional to the time difference taken of the reference image (here $i = 1$ ), which forms $D_i$ . The $D_i$ images are stacked and averaged to form the final image, E. Figure Credit: [Gómez, 2016] and Christian Thalmann . . . . .	22
2.9	SDI descriptive diagram. Images $A_\lambda$ are taken, the high frequency images are stretched by a scaling factor inversely proportional to $\lambda$ making $B_\lambda$ . The stretched images' edges are cropped off. These are averaged to form a median image, $C_\lambda$ . This is shrunk to multiple sizes; the new set is $D_\lambda$ . The $A_\lambda$ images are subtracted by the $D_\lambda$ images, making $E_\lambda$ . A median of the $E_\lambda$ images cut to the smallest $E_\lambda$ image's size makes a final image, F. Figure Credit: Kiefer et al. [2021] . . . . .	23

- 3.1 Left: The 1984 discovery of a circumstellar disk around Beta Pictoris image. Figure credit: [Smith and Terile, 1984]. Right: An composite infrared image from 2008 with annotations of the Beta Pictoris system. Figure credit: [European Southern Observatory, a]. . . . . 25
- 3.2 Images of Beta Pictoris system taken over multiple years. Ordered left to right from top to bottom, as first to fourth, the planet beta Pic b is visible on the lower-right of the first image, has minimal SNR and no separate signal in the second image, is seen in the upper-left of the third image, and is most clearly visible in the upper-left of the fourth image. Note: The different colors of the backgrounds are primarily due to the depth of the largest minima in the speckle noise in each picture, each image's background color corresponds to slightly above zero in its own color bar. . . . . 28
- 3.3 Signal-to-noise ratios as functions of wavelength channel index for all possible combinations of ADI and SDI PCA up to 8 components each on the 2020 beta Pic observation. . . . . 30
- 3.4 Zoom in on peak region of previous Figure 3.3. The highest peak occurs at an SNR of  $\sim 128$ , while the lowest peak is at  $\sim 17$  a factor of  $\sim 7.5$ ). The highest peaks have combinations which are scattered around different PCA components. The many light yellow lines at the bottom of the peak come from high SDI PCAs; this is indicative of overfitting, and using such will lead to inferior models. . . . . 31
- 3.5 Signal plotted over parallactic angle at a radius=43 pixels. The small bumps about a zero value are typical background noise, the dips before and after the peak are the consequence of the (ADI) data reduction method, and the large peak is the planetary signal. Referencing Figure 3.2, the zero angle occurs towards the north/upwards direction, and then proceeds in a counterclockwise direction. . . . . 32
- 3.6 Signal plotted on distance/radius to the host star for a single wavelength channel in the 2020 Beta Pictoris observation. The signal around zero is thought to be speckle noise; the large peak at a distance of  $\sim 43$  pixels from the center is deemed the planet. The flattening of the signal near its ends suggests there are no more large or bright planets like Beta Pictoris b at larger orbits (within the orbital distance observed). The large drop in signal after the peak is an artifact of the data reduction (SDI) process. . . . . 32
- 3.7 A combination of a (data) reduced image from SPHERE and the calculated line intersecting the planet position (red dot) and central star (green dot). The pixels underneath the solid orange line are identified and used in the determination of signal behavior as a function of (linear) distance to the star. . . . . 33
- 3.8 Heat Maps of maximum Signal to Noise ratios for different combinations of PCA components in the ASDI and SADI data reductions of Beta Pictoris b during the four observations. Note: The Apparent lack of signal in the results of the 2018, 2016, and 2015 are caused by the range of the color bar, which is the same in all plots. Figure 3.9 shows the other observations' maximum SNRs by using unequal color bars. . . . . 35
- 3.9 Heat Maps of maximum SNR for varied PCA components in the data reductions of Beta Pictoris b over four observations. Unlike 3.8, this figure has unique color bars. . . . . 36

3.10	Areas used to calculate Signal to Noise Ratio (SNR). This example, from the 2015 Beta Pictoris observation, shows how the signal circle is captured (in the red circle) by the calculation algorithm and is compared to signal strength of the visually equivalent regions (in the white circles) around the star. The omissions of two would-be white circles adjacent to the red circle is due to the data reduction artifact that is generated during the ADI process. . . . .	37
3.11	Signal plotted on radius (or distance) to the host star for all wavelength channels. From the left to the right of the plot: There is low-level background noise at large negative radii, intense coronagraphic speckle noise around zero, the planet signal around 40, and low-level background noise beyond the planet. . .	38
3.12	A zoomed in plot around the planet position signal peak from the previous figure. Notice the differences in the position of the peak planet signal as functions of radius for the 39 different wavelength channel detectors. From Fig. 3.11. . . . .	38
3.13	Results of mitigating the suppressive artifact with the first cosine application. It is natural to compare this plot with the one seen in Figure 3.12. . . . .	39
3.14	Results of mitigating the suppressive artifact with the second cosine application. We can see that this second application pinches all of the signals to two common values of zero, showing off it's fundamentally artificial original design. Comparisons with Figures 3.12 and 3.13 show how there can be a sizable variety of ways to negate the data reduction artifact's signal suppression. . . .	40
3.15	Inferior technique results of mitigating the suppressive artifact. The difference between plots like 3.14 and this one show a range in the quality of our mitigation results. . . . .	40
3.16	Results of smooth curve fitting model with error bars on each signal maxima of the signal peak data for the 2020 observation. <u>Note</u> : Some error bars are too small to be seen apart from their local peak maxima; the error bars are seen (vertically) in the Position difference plots beginning with Fig. 3.20 below	42
3.17	Results of smooth curve fitting model with error bars on each signal maxima of the signal peak data for the 2016 observation. <u>Note</u> : Many error bars are wider than the entire signal range used for the fitting . . . . .	43
3.18	Results of smooth curve fitting model with error bars on each signal maxima of the signal peak data for the 2018 observation. <u>Note</u> : The horizontal bars on many peaks are somewhat longer compared to 3.16, which indicate larger uncertainties in the regression . . . . .	43
3.19	Results of smooth curve fitting model with error bars on each signal maxima of the signal peak data for the 2015 observation. <u>Note</u> : There is similarity between the 2015 and 2018 observations, like the similarity in their angular separations seen in Figure 3.2. . . . .	44
3.20	Difference and regressions between fitted smooth curve peak models with the literature value position of Beta Pic b for the 2020 observation. The blue data is seen with vertical error bars from the curve fitting parameter variances (the horizontal bars on peak maxima in the previous four figures); the solid orange line represents a 5th order polynomial OLS regression; and the broken green line represents a linear OLS regression. <u>Note</u> : The value differences are consistently positive between the planet position after the data reduction and the planet's literature position . . . . .	44

3.21	Difference and regressions between fitted smooth curve peak models with the literature value position of Beta Pic b for the 2018 observation. The blue data is seen with vertical error bars from the curve fitting parameter variances; the solid orange line represents a 5th order polynomial OLS regression; and the broken green line represents a linear OLS regression. . . . .	45
3.22	Difference between fitted smooth curve peak models with literature value position of Beta Pic b for the 2016 observation with regressions. The blue data is seen with vertical error bars from the curve fitting parameter variances; the solid orange line represents a 5th order polynomial OLS regression; and the broken green line represents the simple linear OLS regression. . . . .	45
3.23	Difference between fitted smooth curve peak models with literature value position of Beta Pic b for the 2015 observation with regressions. The blue data is seen with vertical error bars from the curve fitting parameter variances; the solid orange line represents a 5th order polynomial OLS regression; and the broken green line represents the simple linear OLS regression. . . . .	46
4.1	Histograms showing uncertainty of curve fitting mean standard deviation error margins. Note: Each plot (year) is on remarkably different Error Margin Values. The distribution on these four plots are compressed into a box plot in Figure 4.2.	50
4.2	Box plots of curve fitting mean standard deviation error margins. The accuracy of how the data reduction calculates the planet signal's mean value or location corresponds to the smallness of the box and whiskers. The bottom blue 2020 observation has the most accurate values, while the margin of error in the upper-middle green 2016 observation is so large outliers have been left outside the field of view shown in the plot (for ease of seeing more pertinent relationships in the data). More detailed distributions are independently plotted as histograms in 4.1 . . . . .	50
4.3	An example of data reduction method complexities. Here a peak is seen in many of the higher wavelengths at approximately 23 pixels from the host star. The thick black line shows the result of data reduction methods used for the first wavelength detector (shortest wavelengths). Though many data manipulation techniques could be used in this situation, all were deemed too unrealistic and or irrelevant to the scope of this thesis to pursue in great depth. . . . .	52
4.4	Future research into optimizing the signal profile (to resemble a normal PSF) might be accomplished with signal well modeled subtractions. Here, the red parabolas indicate how two different wavelength ranges near their minima can be modeled. These models can then be subtracted from the signal data. Optimal ranges and other parameters will be calculated in future investigations. . . . .	53
5.1	Data reduced direct image of Beta Pictoris. The opposite of a normal detection is manifest, as the planet is expected to create signal (white) instead of consuming it (black), but it appears to be consuming it in this reduced image . . . . .	56
5.2	ESA Mission Timeline. The recent and upcoming space missions are shown on a timeline. A more up-to-date figure would show a solid line between Cheops and Webb, as the latter was launch at the end of 2021. Currently, Plato and Ariel are planned for launch in 2026 and 2029 respectively. Figure Credit: esa [2020] . . . . .	58

5.3	A diagram of a star shade. The (unlabeled) details of the figure (i.e., telescope diameter, starshade diameter, telescope-starshade separation, planet-star separation or "inner working angle", wavelength sensitivity range, etc.) will determine what kind of planets will be detectable by the system. Figure Credit: Glassman et al. [2009] . . . . .	58
5.4	Simulated planet population of what is expected to be detected by radial velocity. Plots are after application of observational limits with the spectrographs HARPS/3.6 m (precision of 1 m/s) in the left panel, ESPRESSO/VLT (precision of 10 cm/s) in the middle panel, and CODEX/E-ELT (precision of 1 cm/s) in the right panel. Figure Credit: [Haehnelt and Pasquini, 2010] . . . . .	59
5.5	PLATO's designed sensitivity range. The left plot shows the left plot shows known (as of 2016) exoplanets and the habitable zone of semi major axes, given a stellar mass. There have already been exoplanets detected in habitable zones around other stars, but in comparison to the number of hot and small semi major axis planets, there are few known in habitable zones. The right figure shows the parameter space able to be investigated by PLATO, and how it is mostly distinct, but partially overlaps other space missions (i.e. TESS and K2). Figure Credit: the [2017] . . . . .	61
5.6	Future Roman telescope's exoplanet detection range (previously named WFIRST), with Kepler range as reference. Y-axis is Planet Mass. Figure Credit: Batista [2018] . . . . .	62
5.7	Transmission Spectroscopy Diagram: Transit and eclipse geometry showing how in more opaque atmosphere wavelengths (due to absorption by atoms or molecules), the planet blocks slightly more stellar flux. Figure Credit: Kreidberg [2018] . . . . .	62
A.1	Difference between fitted smooth curve peak models with literature value position of Beta Pic b for the 2018 observation. . . . .	74
A.2	Difference between fitted smooth curve peak models with literature value position of Beta Pic b for the 2016 observation. . . . .	75
A.3	Difference between fitted smooth curve peak models with literature value position of Beta Pic b for the 2020 observation. . . . .	75
A.4	Difference between fitted smooth curve peak models with literature value position of Beta Pic b for the 2015 observation. . . . .	76
A.5	6th order polynomial regression of 2018 observation. Difference between fitted smooth curve peak models with literature value position of Beta Pic b for the 2018 observation. . . . .	76
A.6	9th order polynomial regression of 2018 observation. Difference between fitted smooth curve peak models with literature value position of Beta Pic b for the 2018 observation. . . . .	77
B.1	Diagram of the Transit method of exoplanetary detection. Figure Credit: Deeg and Alonso [2018] . . . . .	78
C.1	Radial Velocity heat map of the visible material of the Beta Pictoris system. This paper makes use of ALMA data . . . . .	79

# List of Tables

3.1	Wavelength Detection Channel Ranges of the SPHERE instrument at the VLT. The numbers indicate the middle of the wavelength bin in micrometers; the difference between two numbers ( $\sim 10\mu m$ ) is the width of the bins. <u>Note</u> : The visible spectrum ends at $\sim 0.7\mu m$ ; SPHERE straddles the boarder between IR and microwave light. . . . .	26
3.2	Observation Times of Beta Pictoris made by the SPHERE instrument at the VLT. . . . .	27
5.1	Potential Targets of research. Though only the first target listed (Beta Pictoris) was investigated, the applicability of our research might extend to a range of exoplanetary systems that can be discovered with additional time. . . . .	57

# Contents

<b>Preface</b>	<b>i</b>
<b>Summary</b>	<b>ii</b>
<b>Summary for general audiences</b>	<b>iii</b>
<b>List of Figures</b>	<b>iv</b>
<b>List of Tables</b>	<b>x</b>
<b>Contents</b>	<b>xi</b>
<b>1 Introduction</b>	<b>1</b>
1.1 Planet Formation . . . . .	2
1.2 Types of Exoplanets . . . . .	2
1.3 Detection methods of exoplanets . . . . .	3
1.4 Open Scientific Questions . . . . .	13
1.5 Objectives . . . . .	13
<b>2 Methods</b>	<b>14</b>
2.1 SPHERE at the VLT – The Instrument of Choice . . . . .	14
2.2 ESO Archive . . . . .	16
2.3 ESO Reflex . . . . .	18
2.4 PynPoint . . . . .	18
2.5 Differential imaging: ASDI, SADI, CODI . . . . .	20
2.6 Principal Component Analysis . . . . .	23
<b>3 Results</b>	<b>25</b>
3.1 Interpreting SPHERE’s Data . . . . .	26
3.2 Observation Times and Parameters . . . . .	26
3.3 Spectral characteristics of signal and PCA . . . . .	27
3.4 Signal-to-noise and PCA – Heat Maps . . . . .	31
3.5 Signal, distance, and all wavelength channels . . . . .	34
3.6 Modeling and mitigating the suppressive data reduction artifact . . . . .	37
3.7 Curve fitting of signal peaks and error from literature position . . . . .	41
<b>4 Discussion</b>	<b>47</b>

4.1	Instrument considerations . . . . .	47
4.2	Target considerations . . . . .	47
4.3	Comparison of methods (ASDI & SADI) . . . . .	48
4.4	Comparison between times & angular separations . . . . .	49
4.5	Artifact reduction considerations . . . . .	51
<b>5</b>	<b>Conclusions</b>	<b>54</b>
5.1	Thesis Summary . . . . .	54
5.2	Outlook . . . . .	55
5.3	Ending thoughts . . . . .	61
	<b>Bibliography</b>	<b>63</b>
	<b>Appendices</b>	<b>73</b>
<b>A</b>	<b>Additional Results Plots and Figures</b>	<b>74</b>
<b>B</b>	<b>Additional Exoplanet Detection Method Diagrams</b>	<b>78</b>
<b>C</b>	<b>ALMA Based Research</b>	<b>79</b>

# Chapter 1

## Introduction

Exoplanets or extrasolar planets are any planets outside our solar system [NASA, 2022]. Though the thought of detecting them arose much earlier (in 1952, Otto Struve proposed to use the radial velocity and transit methods to detect short-period exoplanets [Struve, 1952]), the first exoplanet orbiting a solar-like star was discovered in 1995 [Mayor and Queloz, 1995], and over 5000 more have been discovered since [NASA, 2022]. This massive increase in less than 30 years is seen in Figure 1.1. The large jumps in Transit (green) cumulative detections

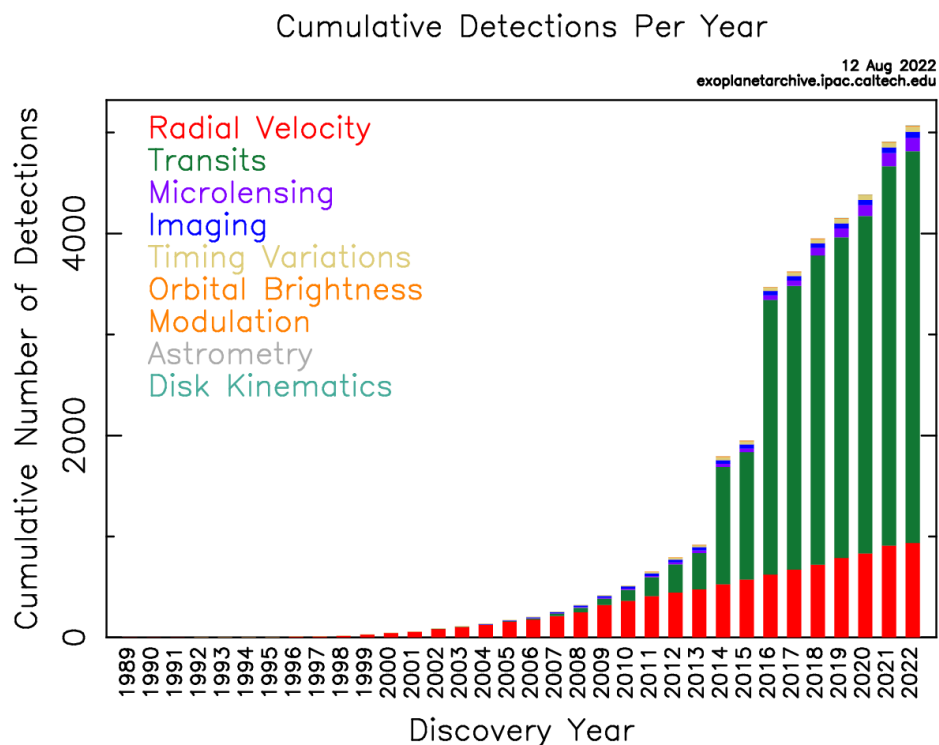


Figure 1.1: Exoplanet Detections Over Time. Figure Credit: [NASA, 2022]

in 2014 and 2016 were made primarily from the novel Kepler space telescope [Johnson, 2015], [NASA, 2022]. Increases in the detection rates of some of the currently less fruitful methods (colors) are expected in the next decade; this will be discussed more in the conclusion of the thesis.

## 1.1 Planet Formation

The field of star and planet formation is broad. The timescales of almost all astrophysical phenomena vastly exceeds a human life, and most are much longer than the age of modern astronomy. This means that we develop astrophysical models by looking at different systems and assuming they are undergoing the same process, but are only of different physical characteristics (i.e., mass) and at different parts of the process. The overarching model suggests that large clouds of (molecular) gas and dust fragment into smaller collapsing regions. This continues until the energy and density in a (central) region can begin to do nuclear fusion; a star is born. The heat, expansion, and rotation of the star lead the remaining gas and dust to vacate or collapse onto the plane of the star's rotation; a protoplanetary disk is born. Planetary growing is then accomplished in different phases [De Koter].

Collisions lead to aggregation of microscopic dust grains that stops when it reaches a size on the order of a centimeter. An intermediate regime is necessary (and an area of modern cutting-edge research) for the structures to grow into kilometer sized "planetesimals." After reaching this size, two (or more) planetesimals are massive enough to gravitationally attract each other through the protoplanetary (or soon to be *debris*) disk. At this point, collisions are not likely to cause a large decrease in total mass because even material ejected from surfaces is likely to still remain in the gravitational well of the now-one body and fall back down to it. Growth proceeds rapidly until the orbit is sufficiently cleared [De Koter], then the title of planet is given. Research is going into every part of this process; the research on the final planetary bodies is exoplanet research.

## 1.2 Types of Exoplanets

Planets similar to the solar system ones can be seen in other parts of the nearby galaxy, but planets that are distinctly different from anything nearby have also been detected. Especially in such a nascent field as exoplanet science, only a few quantities are known about the detected planets. The distribution of exoplanets detected with respect to their mass and period is seen in figure 1.2

The three dense clusters around 1 Jupiter mass, 5-day period; 5 Jupiter mass, 1000-day period; and 0.01 Jupiter mass, 10-day period show the prevalence of "hot Jupiters," "exo-jupiters," and "mini-Neptunes" or "super-Earths" respectively. Jupiter (and less so Saturn) is the most familiar analog that we can find in our solar system for most of today's known exoplanets. Kepler-20e might be the smallest exoplanet known to us [Kep]; the worlds that are smaller exist in an entirely unknown abundance. Naturally, The smaller the planet, the more difficult it is to detect; thus there might be billions of super-mercuries or even mini-mercuries and many earth-like planets in the Milky Way, but our ability to detect them is currently limited to the sensitivities of today's range of telescopes.

Significantly more information on the variety and distribution of exoplanet characteristics is available at NASA [2022]; some of the most insightful is seen in the plots of Figure 1.3. These include relationships between orbital period, planetary mass and radius, and irradiation and equilibrium temperature.

Mass and Radius (and thus density) confine exoplanets to falling on ranges within distinct

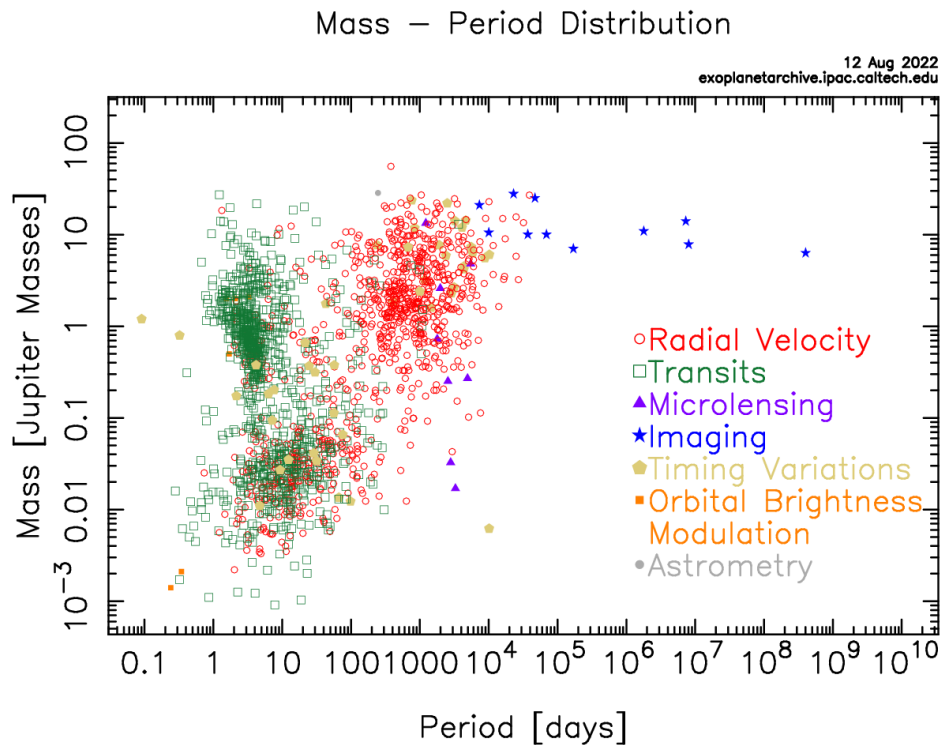


Figure 1.2: Exoplanet Distribution on Mass and Period. Figure Credit: [NASA, 2022]

(size) regimes. This is seen in Chen and Kipping [2017]’s Figure 1.4. The Earth lies in the left-most regime along with similarly small worlds (planets, sufficiently large moons, or other planet-like celestial bodies). Other bodies with relatively thin atmospheres can be found in this region. Only slightly more massive planets are going to contain a larger, more volatile envelope. This leads to the increase in slope seen in the Neptunian worlds’ regime compared to the Terran worlds. This continues for some time, but comes to an end when the additional mass makes for a gravitational strength that is sufficient to cause self-compression. This explains the inverse relationship between the mass and radius within the Jovian regime. Finally, with more mass, the gravitational energy in the center of a planet becomes strong enough that nuclear fusion can occur, the proportional relationship resumes (see right-most regime), and the world stops being a planet and becomes categorized as a star.

Though many more masses and periods of exoplanets have been detected than are observed in our solar system, many more may be present in the universe. Each detection method has a bias to observe a different type of exoplanet; with a variety of methods we are able to see more kinds of exoplanets, but still not all of them.

### 1.3 Detection methods of exoplanets

There are a variety of methods astronomers use to detect (and characterize) exoplanets. In this thesis, we will introduce the fundamentals behind the Radial Velocity, Transiting, Astrometry, (pulsar) Timing, Gravitational Microlensing, and Direct Imaging techniques. A more detailed emphasis will be provided for the last technique as it was used throughout our research.

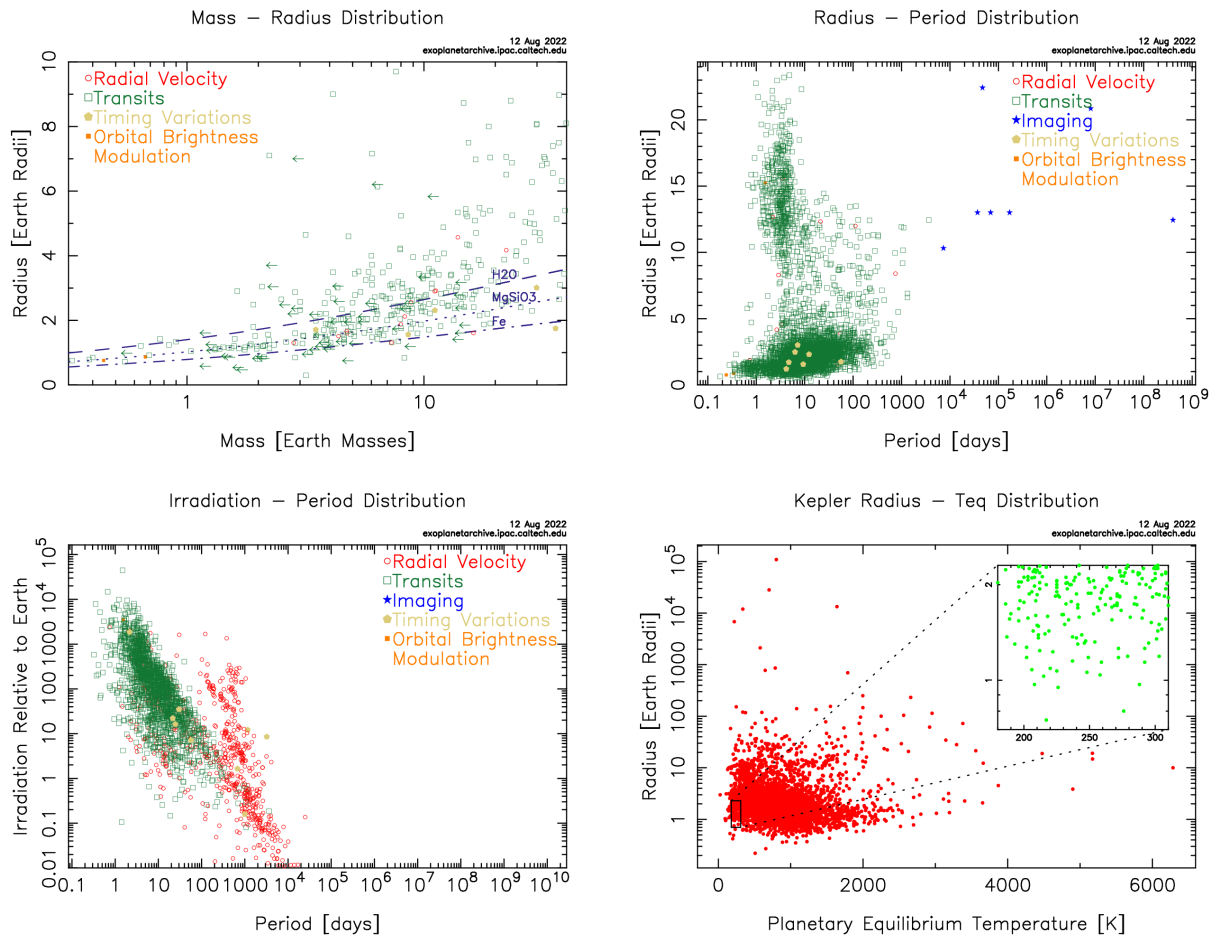


Figure 1.3: Distributions of Exoplanets Plotted on Various Parameters. The *top left* plot shows radii on mass, with different material references (water, rock, iron). The *top right* plot shows radii on period for five detection methods. The *bottom left* plot shows irradiation on period for five detection methods. The *bottom right* plot shows radii on temperature; the inset zooms in on the planets with earth-like radius and temperature. Figure Credit: [NASA, 2022]

## Radial Velocity

The Radial Velocity Method of detecting exoplanets is one of the most popular methods. It had tremendous initial success when it was used to find the first exoplanet around a solar-like star [Mayor and Queloz, 1995]. This finding led being awarded the 2019 Nobel Prize in Physics. Through the rest of the 1990s and the 2000s, Radial Velocities have accounted for the vast majority of exoplanetary detections (see Fig. 1.1).

Mechanistically, light emitted from a moving source is red-shifted or blue-shifted on the axis of its movement. A star emits light and moves around a center of mass that is shared between it and its exoplanet(s). If the plane of the stellar system is parallel (or rather, not perpendicular) to our line of sight, there will be red-shifted and blue-shifted oscillations in the light coming from that star. This is shown visually in Figure 1.5. Using this method, astronomers can extract parameters of the exoplanet, namely: the minimum mass and orbital period.

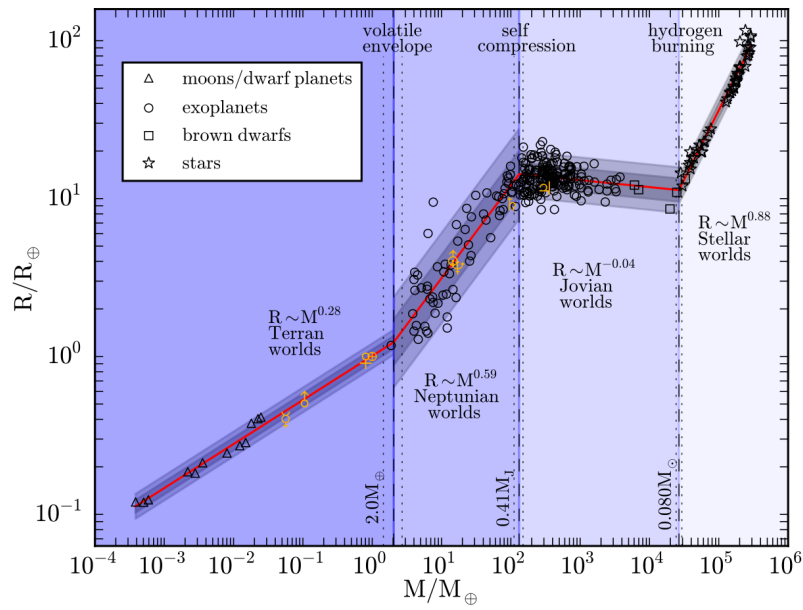


Figure 1.4: Exoplanet regimes, based on mass and radius. Figure Credit: [Chen and Kipping, 2017]

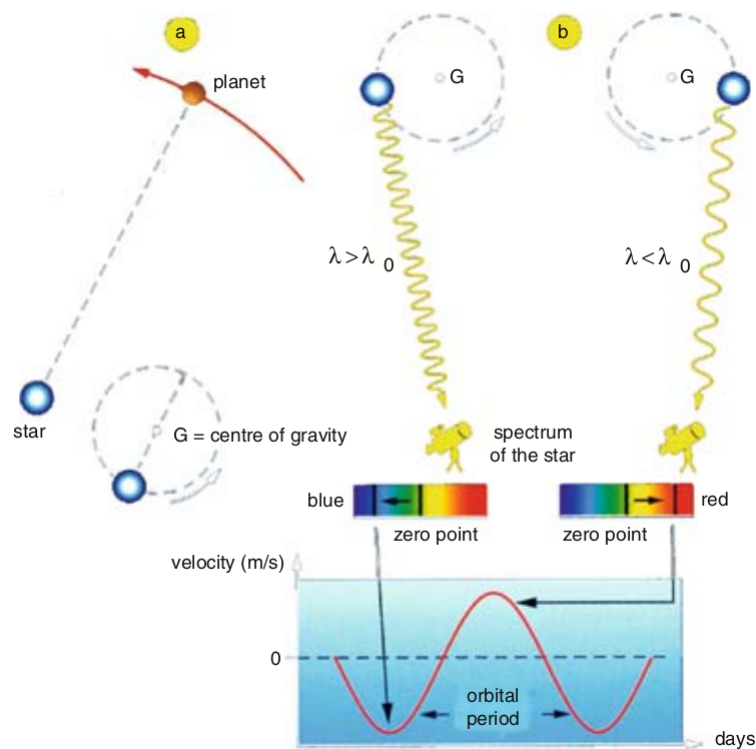


Figure 1.5: Diagram of the Radial Velocity method of exoplanetary detection. Figure Credit: [Ollivier et al., 2009]

More locally, the HERMES instrument at the Mercator Telescope has been recording astrophysical spectra since "the beginning of 2009" [Gielen, 2023] and will soon be joined by the MARVEL, which is an array of four 80 centimeter telescopes connected via optical fiber to a single high-resolution echelle spectrograph, which "builds on the heritage of HERMES." These future observations will be optimized for extreme-precision radial velocity measurements and should be on "a fast track to commissioning" this year. [Raskin et al., 2020].

## Transits

During the 2010s, the transit method of detecting exoplanets took the spotlight in the community. The space missions Kepler, K-2 [Borucki et al., 2008], and the more recent TESS [Ricker et al., 2014] have all relied on the transit method to detect most of the planets that we know of today. Its recent popularity is shown in Figure 1.6 The transit method detects

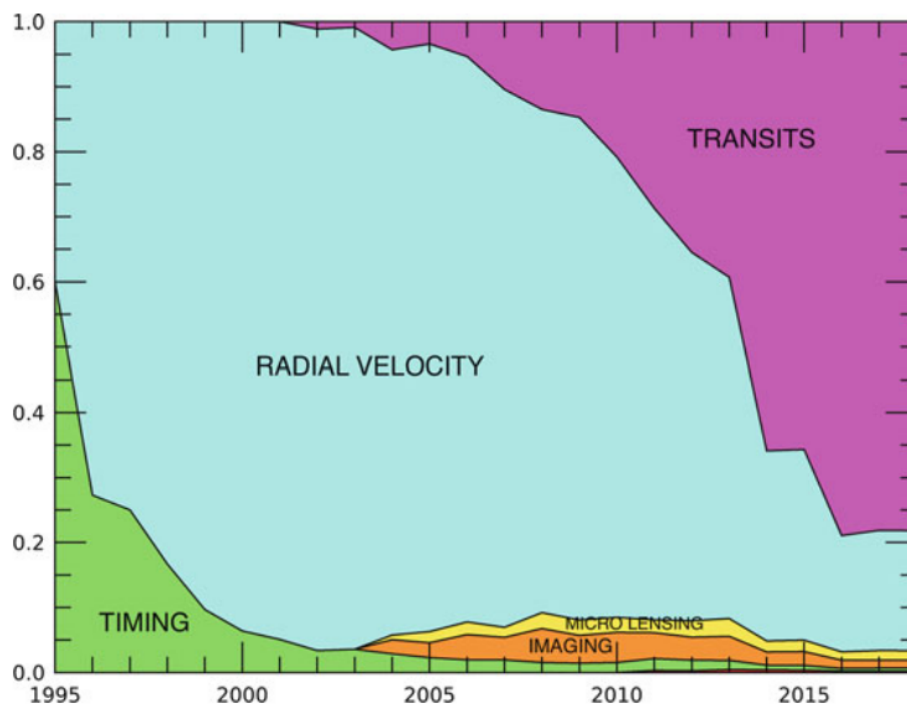


Figure 1.6: Fractions of detection methods that contributed to known planet discoveries from 1995-2018. Figure Credit: [Deeg and Alonso, 2018]

exoplanets by measuring the drop in light obtained from a star as an exoplanet passes between the star and the detector. The radial velocity method is most efficient when the plane of the stellar system is parallel to the line of sight, but it can still work when there are more than a few degrees of inclination between the plane of the system and our line of sight; this is not the case for the transit method, which relies on occultations (eclipses) for detections. This method most naturally finds planets that are large and close to their host star (small orbital period). The latter is partially because of a decrease in probability that the star-planet plane will be in an alignment with the line of sight as the separation between the two bodies grows. This probability decreases quickly as the period and orbital distance grow. By observing an exoplanet's transits of a star, detection will, be more favorable for planets at short distances from their host star; this is independent of detectability considerations [Ollivier et al., 2009].

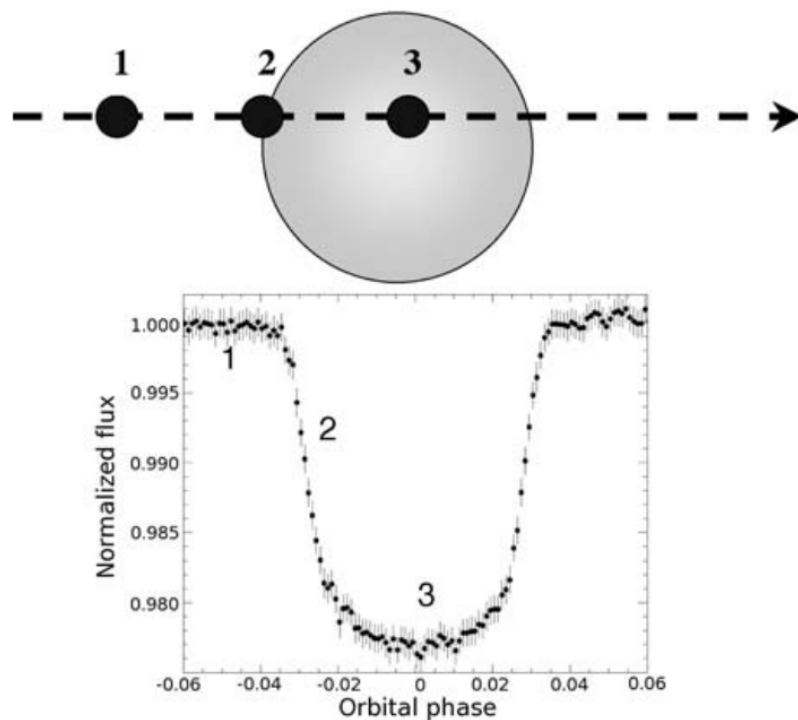


Figure 1.7: Diagram of the Transits method of exoplanetary detection. Figure Credit: [Ollivier et al., 2009]

Transit detections lead to estimates of the size (radius) of the exoplanets. If this size can be coupled with a mass estimate (see radial velocity), then a planetary density can be calculated.

## Astrometry

Astrometry is a detection method that observes the gravitational pull that an exoplanet exerts on its host star. In this regard, it is very similar to the radial velocity method, but the key difference between the two is the geometry that planets can most readily be detected in. Unlike the radial velocity method, where we see changes in the spectra of a star, the astrometry detection method observes changes in the location of a star. This is because astrometry works best when the plane of the exoplanet and host star is perpendicular to our line of sight. The orbit of the star around the system's center of mass makes a circle, which will not have significant red-shifting or blue-shifting of its light. Astronomers use the astrometry method, like the radial velocity method, to estimate the masses of orbiting exoplanets. The circular motion observed on the sky combines with the apparent motion of the earth's rotation. Thus, ground-based astrometry detections are made through the careful observations of spirals.

A spiral trajectory is seen in Figure 1.8; the dashed line is the system barycentric motion. The dotted line is the effect of earth's parallax. The solid line is the astrometric motion, the effect is magnified 30x for visibility. The dots are locations in time indicated in years (arbitrarily chosen to begin in April 2018). The system has been set up with a distance of 50 parsecs, a proper motion of,  $v = 50 \text{ milliarcseconds} \cdot \text{yr}^{-1}$ , and a planet of mass of,  $m = 15M_J$ , orbiting with eccentricity of,  $e = 0.2$ , and semi-major axis,  $a = 0.6 \text{ AU}$ . For observations that occur over substantial periods of a year (so the location of the earth is no longer approximately

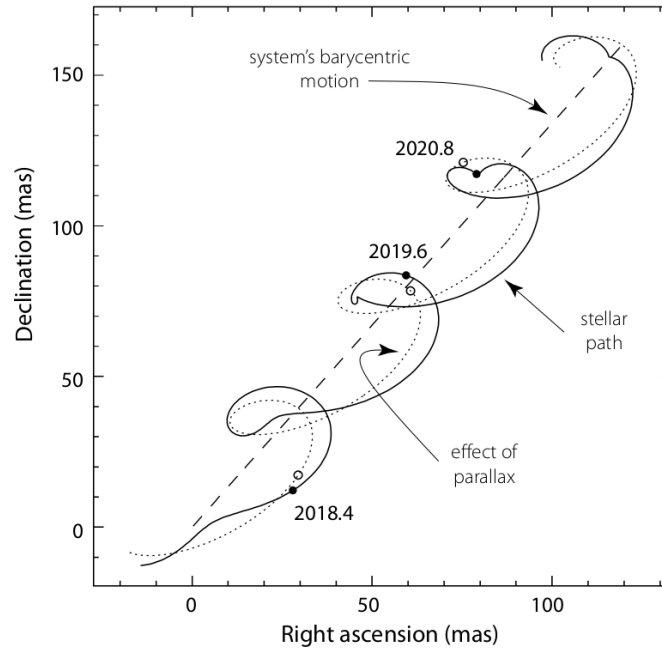


Figure 1.8: Astrometric trajectory of motion in combination with the apparent motion and orbit of the earth. The system is at a distance of  $d = 50$  parsecs, orbits with eccentricity  $e = 0.2$ , and semi-major axis  $a = 0.6 AU$ , and has a planet of mass  $m = 15M_J$ , and a proper motion of  $v = 50$  milliarcseconds  $\cdot yr^{-1}$ . Figure Credit: [Perryman, 2018]

constant), the parallax of the earth is to be considered as well. In the figure, the spiral loops can then be used, while compensating for earth's orbit, to extract properties of the exoplanet and its orbit [Perryman, 2018].

We see few detections made via the astrometry method in Figure 1.1. This is because the sensitivity of currently used instruments is lacking compared to what is necessary to make a detection using the transit and radial velocity methods. Astrometry is highly promising, but its relative slowness in reaching an advanced and prolific stage has made it one of the more obscure techniques. One can see some results of an observation and the associated error bars in Figure 1.9. The modeling of such orbital motion is complex, and even more so for many-body systems. In this figure's research, 21 free parameters were identified; most of which had stable solutions determined by using Markov chain Monte Carlo (MCMC) chains. The parameter estimates made quasi-Gaussian posterior distributions; which suggested that the model is well-constrained and the astrometric orbit was detected from their measurements (also made at the VLT). In order for us to detect exoplanets with the astrometry method, we can consider the influence of our neighboring planets on our G-type star. Figure 1.10 shows how the variations over 20 years would be seen in ( $\sim 1$  milliarcsec) astrometric movements around an average central location. Though it has not been as fruitful as other detection methods, the near-future is bright because GAIA's up-and-coming data releases are expected to provide many more astrometry detections [Gaia Collaboration, 2020]. See future investigations for details.

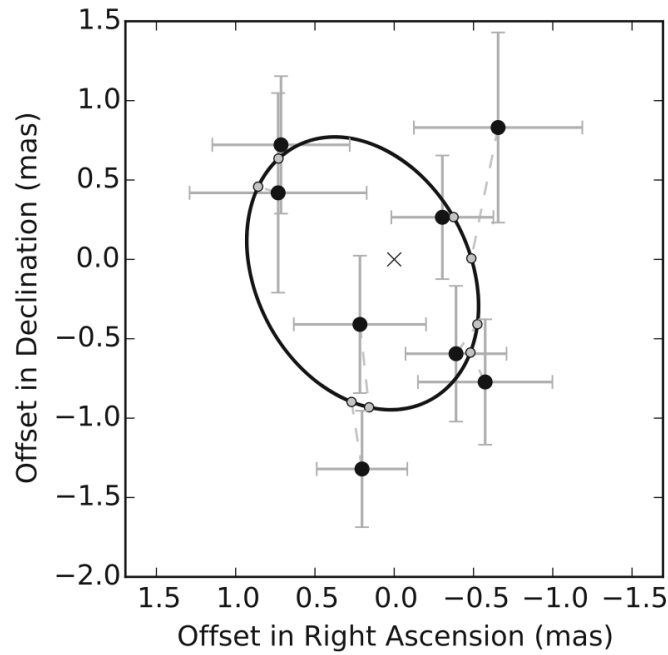


Figure 1.9: Astrometric motion of (star) GJ 676A believed to be from a planet orbiting in a plane near-perpendicular to our line of sight. Measurements are black dots, the calculated orbit is a large black ellipse, the gray dashed lines connect to gray dots at the best planetary locations in time. Figure Credit: [Malbet and Sozzetti, 2018]

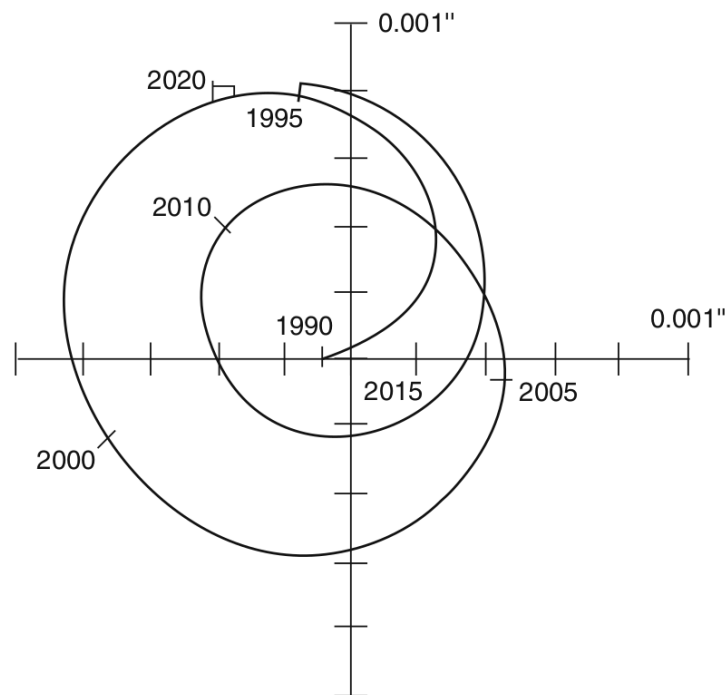


Figure 1.10: Astrometric motion of the sun from a distance of 10 parsecs. There are thousands of celestial bodies within this distance [Reylé et al., 2021]; and any observer (looking at the solar system face-on) would see this much (or more, if closer) astrometric motion. Figure Credit: [Ollivier et al., 2009]

## Timing (pulsar)

The first exoplanet orbiting a solar-like star was detected in 1995 [Mayor and Queloz, 1995], but the first true exoplanet was discovered slightly earlier by *pulsar timing* [Wolszczan and Frail, 1992]. Detecting small planets is always more difficult than large planets. However, with this particular, pulsar timing technique, it is theoretically so precise that it is able to detect planets with no more mass than that of a large asteroid. This detection method observes the extremely stable rotation of neutron stars to their corresponding pulse, as well as the subtle, small changes from uniform regularity. These are small changes in the time of arrival of pulsar signal; they are used to develop models of planetary orbits and thus allow for exoplanet detections [Seager, 2010]. This method's origins are seen in the Figure 1.11.

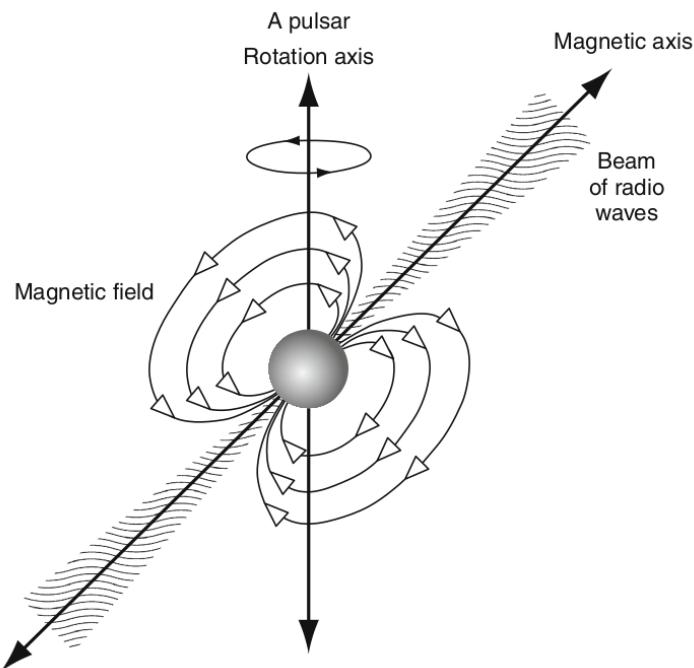


Figure 1.11: Pulsar Timing Method of exoplanet detection. Radio emissions are rapidly rotated. The emission can be observed if the sweeping beam comes in contact with our detectors. Figure Credit: [Ollivier et al., 2009]

## Gravitational microlensing

A famous quote of John Wheeler regarding General Relativity is that "Space-time tells matter how to move; matter tells space-time how to curve." This is shown in figure 1.12 where the light emitted by a source, S does not travel along the straight dotted line to the observer, but rather takes a path that is akin to the solid line because of the influence of the lens, L. This is depicted in Figure 1.12.

Though this technique has not provided an abundance of exoplanets to observe compared to the radial velocity and transits methods, it has the current capability of finding exoplanets that are far more distant than what other techniques are currently capable of. Future missions in the field of gravitational microlensing have very promising results. More information on

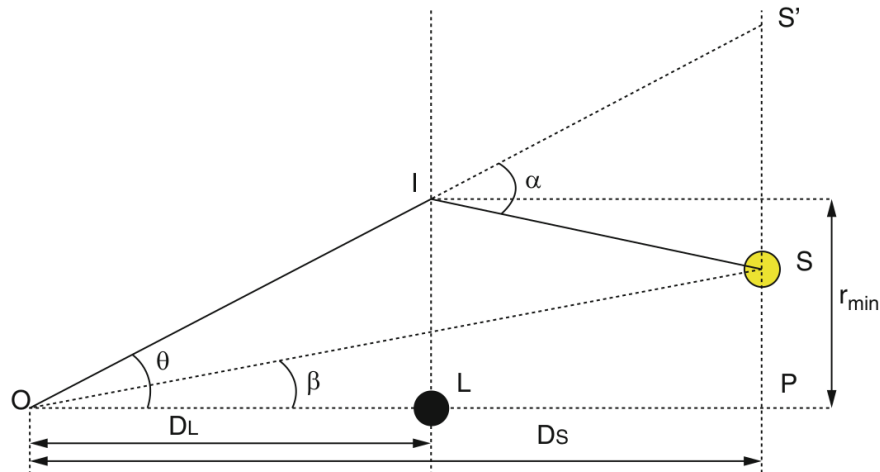


Figure 1.12: Gravitation Lensing Diagram: Deviation of a light ray from the gravity of a massive body. The diagram simplifies the more complex behavior that would be exhibited in a curving light ray into a discretely redirected light ray; this is a reasonable approximation to make if the distances between the source, lens, and observer are far apart (with respect to the speed and travel time of light) Figure Credit: [Batista, 2018].

the Nancy Grace Roman Space Telescope mission can be seen in the conclusion's future work section.

## Direct Imaging

The direct imaging technique of exoplanetary detection was analyzed extensively in the research of this thesis. It is also possibly the most familiar or intuitive detection method for most audiences: picture taking. Though portrait or landscape photography and direct imaging have some aspects in common, there are differences that separate the two procedures to think of them as unique. Because of these, the first direct images of exoplanets were published 12 years after exoplanets were first detected. The challenges with directly imaging an exoplanet are primarily the contrast difference between it and its host star and the angular separation between the planet and its host star [Seager, 2010]; and so special solutions are necessary to overcome these, which are not readily available in the common earthly photography market.

There are solutions to overcome the challenges posed to the direct imaging of exoplanets. During observations, instruments are to have the capabilities of suppressing the starlight, but not the emitted infrared or thermal light of the planet, and of suppressing scattered light entering the telescope. The thermal planet light comes from the contracting it, as a young planet, is still undergoing. Starlight has been suppressed through the use of interferometry and (in the case of SPHERE) coronagraphy. Scattered light can be suppressed by Adaptive Optics (AO), which uses guide stars (often artificially generated ones via lasers) and deformable mirrors [Seager, 2010].

Blocking the light from a star, but receiving the light of a planet, is necessary to directly image exoplanets. The technique of coronagraphy allows for valuable planetary photons to be insightfully isolated from the stellar light [Guyon et al., 2006]. Though the use of coronagraphy

is relatively new in the field of exoplanets, it has been in use elsewhere for almost a century. Bernard Lyot invented the coronagraph in the early 1930s. Its original purpose was to make observations of the sun's corona [Loyt, a] [Loyt, b]. The coronagraph was, and still is, to reach a maximal reduction of the light diffracted and scattered along the optical pathway. [Ollivier et al., 2009]. This method of observation has evolved of the last 90 years and is one of the key components of the Spectro-Polarimetric High-contrast Exoplanet REsearch (SPHERE), which made the observations that are analyzed throughout the body of this thesis [Beuzit et al., 2019]. A second approach to starlight suppression is through interferometry. SPHERE and the research of this thesis do not rely on traditional interferometric techniques, however this technique is and has been in use around the world for extensive periods of time. One of the famous workhorses of modern astronomy, the VLT in Chile, became the VLTI (VLT-Interferometer) on 17 March 2011 when it Combined Light from all Four VLT Unit Telescopes for the First Time [Berger et al., 2011]. Interferometry is a large and complex field, and so we will give it only a cursory introduction here by saying there are different types of interferometers, most notably nulling interferometers and imaging interferometers, and they suppress starlight by configuring the incoming light in multiple detectors to be out of phase and thus interfere (as the name suggests) destructively where the (central) starlight is coming from [Seager, 2010].

A third approach is to use external occulters, also known as, star shades [Seager, 2010]. This approach is beyond the scope of this thesis but is discussed briefly in the conclusion as a potential part to multiple upcoming space missions.

### **Differential Imaging: Angular, Spectral, and Combined**

The methods of Angular, Spectral, and Combined Differential Imaging (ADI, SDI, and CODI) are discussed individually and in detail in the methods section 2.5. We introduce them here as various techniques of data reduction that uniquely negate central starlight and stack peripheral planet light that is located at different pixel positions (due to observations made at different times or wavelengths). ADI, SDI, and CODI, are ways to organize photometric and spectroscopic data, after making an observation, they improve the detection of planet signal while incurring minimal additional error (for example, by assuming constant atmospheric conditions between two sequential exposures).

Much of the work done for this thesis was inspired by Kiefer et al. [2021], which showed that using SDI and ADI consistently yielded results with greater signal-to-noise ratios than the more traditional or classic approach of using ADI alone. The first steps of their work are expanded greatly in this thesis. The work of Flasseur et al. [2020] has shown one way of generating clear detection maps with adjustable thresholds for confidence intervals around a given detection. Their PACO ASDI method is sensitive to small variations in the data, robust against false detections, and capable of making smoothed spectra from observations. All of these detections methods, including the ones made in this research, form the basis for the closely related, but more difficult, practice of exoplanet characterization.

## **Characterization of Exoplanets**

After knowing that an exoplanet is around a nearby star, the natural follow-up is to ask, "what kind of planet is it?" There are few instruments available today that are sensitive

enough to accurately characterize complex parameters of exoplanets (for example, atmospheric composition); none of them have been analyzed in this research. Therefore, this topic goes beyond the scope of the research done here, despite the two fields of exoplanetary detection and characterization being closely related. Nevertheless, future missions are planned with state-of-the-art technology (often still in development) that will allow for characterization in ways we have never been able to do before; this will be revisited in the conclusion's future work section.

## 1.4 Open Scientific Questions

There are many exciting areas of modern exoplanet research; some are addressed in the research of this thesis. Fundamentally, the theme of most of the topics revolves around the question of how can we best detect exoplanets. This is a means to answering another pair of key questions: what can we learn from a greater understanding of exoplanet populations & characterizations, and how diverse are exoplanet systems. Perhaps the most inspirational to humanity is the big question of is there life beyond our planet. The research done in this thesis lends itself to the more practical question of how can we obtain a spectrum of an exoplanet (using SPHERE/IFS), and as the spectrum gets more accurate with better instruments, what can each step teach us along the way.

## 1.5 Objectives

The objective of this thesis is to discover the optimal combination (or combinations) of high-contrast imaging techniques for detecting an exoplanet as a function of the characteristics of the data-set: size, observing condition, and separation of the exoplanet. It is also to make a proof-of-concept investigation into the mitigation of suppressive data reduction artifacts, and compare preliminary results using different methodologies. The introduction and conclusion are broad, which are designed to bring people from outside astronomical circles up to date on many aspects in the field of exoplanetary astronomy.

# Chapter 2

## Methods

This chapter is organized into six parts. First and second are a discussion of data acquisition, which is accomplished with the **SPHERE** instrument and **ESO Archive**. The third part introduces **ESO Reflex** as a bridge between the raw data stored in the ESO Archive and functional data reduction software. We then discuss the workhorse software **PynPoint** fourth; this performs **differential imaging techniques**, which is the fifth part (and sub-parts) of this chapter. PynPoint can also perform reductions while applying a **principal component analysis**, which is the sixth and final part.

### 2.1 SPHERE at the VLT – The Instrument of Choice

This section introduces the physical characteristics of the SPHERE instrument and how it performs the techniques in section 1.3, provides a definition and short description of the coronagraph in it, clarifies contrast limit capabilities, and introduces the technique of adaptive optics, which works in conjunction with the instrument.

#### SPHERE Specifications

The observations that are analyzed in this thesis were obtained by the Spectro-Polarimetric High-contrast Exoplanet REsearch (SPHERE) at the Very Large Telescope (VLT) in Chile [Beuzit et al., 2019]. In particular, we used the Integral Field Spectrograph (IFS) [Claudi et al., 2008] [Mesa et al., 2015], which is an instrument that is capable of binning light into different pixels, and then subsequently, dispersing the light in each pixel in order to generate a spectrum for that pixel [European Southern Observatory, 2021b]. Diagrams of the two instruments can be seen in Figures 2.1 & 2.2. The IFS has as an output a data cube of 39 monochromatic images. The images have a spectral resolution of  $R \sim 50$  in light wavelengths between  $0.95 - 1.35 \mu m$  (Y-J bands) and a  $R \sim 30$  between  $0.95 - 1.65 \mu m$  (Y-H bands) [The European Southern Observatory, 2019]. The particular ranges of wavelengths that each channel is sensitive to is tabulated here 3.1.

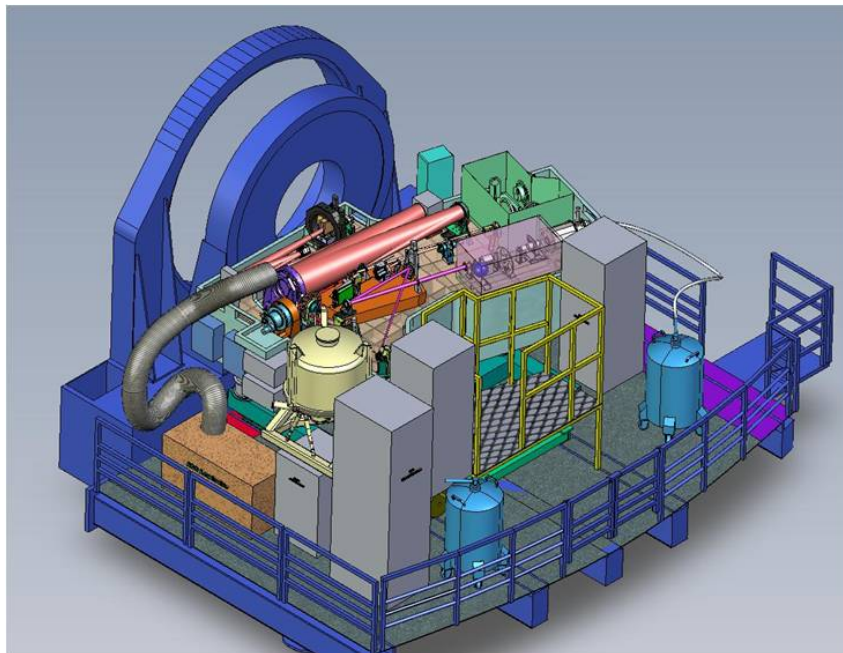


Figure 2.1: Diagram of the Spectro-Polarimetric High-contrast Exoplanet REsearch (SPHERE). Figure Credit: [European Southern Observatory, 2021b]

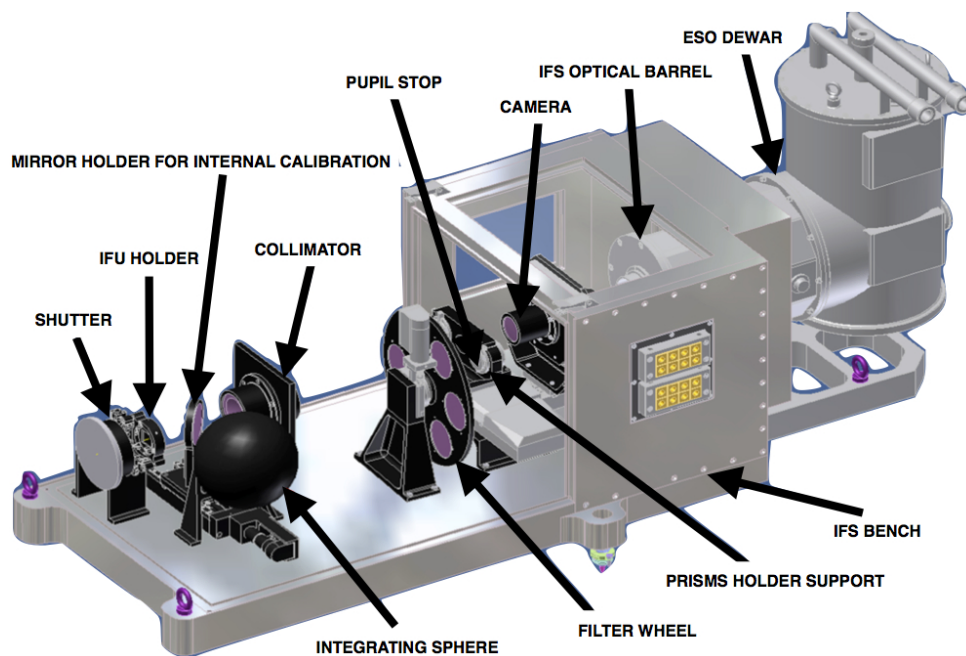


Figure 2.2: Diagram of the Integral Field Spectrograph (IFS) on SPHERE. Figure Credit: [European Southern Observatory, 2021b]

## Coronagraphy

The Common Path and Infrastructure of SPHERE obtains light from the VLT, and passes adaptive-optically focused, stable, and coronagraphic beams to the IFS (and to two other sub-instruments). The coronagraphs are configured by a mask in the focal plane, a Lyot stop in the downstream pupil, as well as an apodizer in the upstream pupil. Field stops are included in the wheels for the coronagraphs. [European Southern Observatory, 2021b].

## High-contrast imaging

Because of the advanced coronagraphy utilized by SPHERE, relatively large contrasts between stars and planets can be overcome. Design and use considerations were made during its construction, and to meet the required observing capability in both the visible and NIR, SPHERE has a limited ultimate performance. It has been estimated to remain tolerable up to a contrast of approximately  $10^{-6}$  times luminosity difference, it is believed that pushing for much higher contrasts would cause other parts of the system to begin to fail [Beuzit et al., 2019].

## Adaptive optics

For ground-based observations, the scattering of light in the layers of the atmosphere can significantly disturb the resolution of an image. This is a challenge that must be overcome to make direct imaging detections. A good, though not perfect, solution to dealing with these aberrations in light wavefront arrival is through Adaptive Optics (AO). AO intends to compensate for the fluctuations in the atmosphere in order to reach the resolution limited by diffraction across the pupil of a telescope [Perryman, 2018]. AO uses guide stars (often artificially generated by lasers) and deformable mirrors. The change in plane-parallel wavefronts of starlight is seen in Figure 2.3, the machinery used to deform the mirrors is shown schematically in Figure 2.4. This figure shows the path of the target's light and the reference star's light. The control system measures the departure of the received wavefront from a plane-parallel wave. Throughout the observation, the reference light is used to deform the mirror for the science light. The feedback cycle continues until the wavefront error is reduced to a limit imposed by noise. When the loop is closed, the image of the reference star, and those of all objects near it, are continuously corrected.

An example of the results that can be obtained with AO is shown in Figure 2.5. Though a numerical scale is missing from the figure, we can see the large comparative advantage AO has over non-AO with respect to capturing the natural point spread function of a distant object.

## 2.2 ESO Archive

Data from the observations of SPHERE are sent to the ESO Archive and made publicly available after one year [European Southern Observatory, b]. The data used here was obtained from a query of the data from: SPHERE/VLT on Spectroscopy, the Science (and if necessary Calib) category, and the IFU mode. The target was chosen to be the Beta Pictoris system (more systems are discussed in future investigations). Those seeking confirmation of the methodology may examine Figure 2.6, which shows the current layout of ESO Archive and how data, in particular how science IFU SPHERE data, can be obtained. Those wishing to

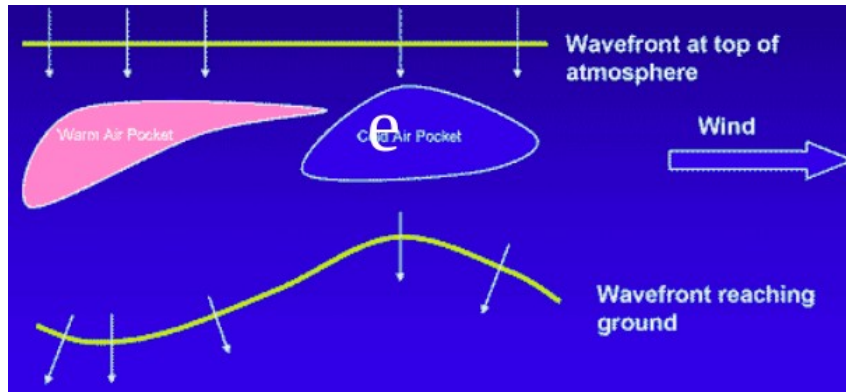


Figure 2.3: Illustration of the development of phase distortion in light propagating through the atmosphere. Figure Credit: [Surdej, 2021]

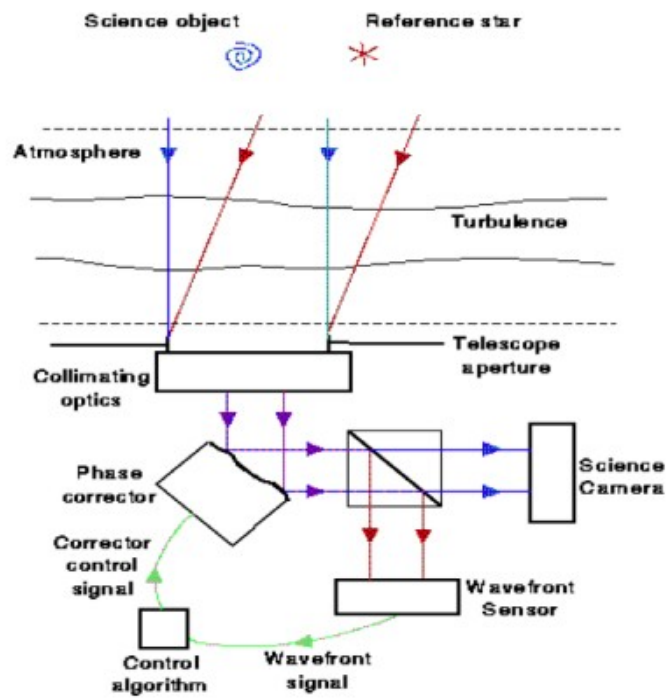


Figure 2.4: Block diagram of a simple AO system. Light from a reference source, such as a star, bounces off a deformable mirror and a portion enters a wavefront sensor. This control system generates a correction signal which moves the deformable mirror, reducing the error. The light leaving the deformable mirror is refocused onto a detector or science camera. Figure Credit: David Carter, Liverpool John Mores University [Carrasco, 2009].

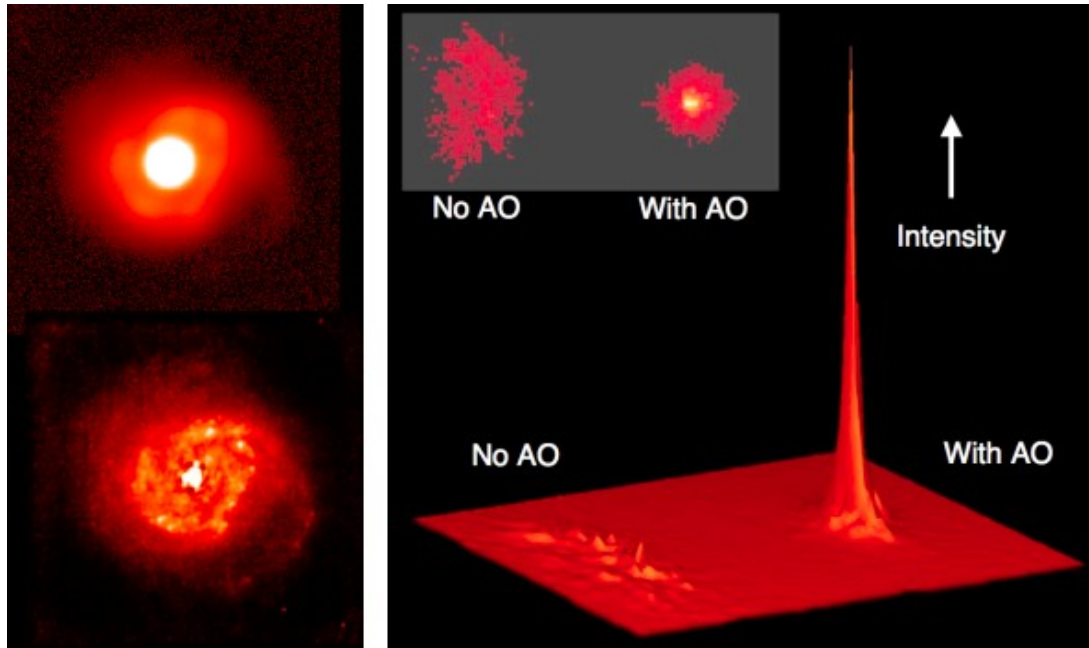


Figure 2.5: The right panel shows an image of the starburst galaxy NGC7469 taken in natural seeing (top) and with adaptive optics (bottom). The left panel shows the image of a star with and without AO. Figure Credit: Canada-France-Hawaii Telescope, [Graham, 2022]

familiarize themselves with the archive can follow this link: [ESO Archive](#) For those endeavoring to replicate or extend the line of this research, more technical or detailed steps are as follows: [Download](#), [unpack](#), and [save](#) the data files. **Downloading** is accomplished after selecting the nights, targets, and other search parameters, in the datasets page. We marked the datasets for our request, ran association for calibration files and marked them as well. Finally, we downloaded the request in a shell script file. The **unpacking** and **saving** were accomplished by standard terminal commands (i.e., `uncompress *.Z`) and the PynPoint pipeline, see section 2.4.

## 2.3 ESO Reflex

After obtaining the data from the ESO Archive, it is to be reduced. This was partially accomplished by ESO Reflex, which can be described as a tool capable of reducing VLT-I data easily and flexibly using ESO pipelines. [European Southern Observatory, 2021a] [Freudling et al., 2013]. ESO Reflex is the necessary bridge between the ESO's data, and the particular specialized data reduction software used to perform the various differential imaging techniques called PynPoint.

## 2.4 PynPoint

PynPoint is an astronomical pipeline that reduces and analyzes high-contrast imaging data for exoplanets [Amara and Quanz, 2012] [Stolker et al., 2019]. It uses principal component analysis (PCA) to subtract out stellar PSFs; and it can readily perform image post-processing

**Observational Raw Data Query Form**

How to use? | Instrument-specific Interfaces | ESO Archive Overview | Archive FAQ | Archive Facility HOME | ESO HOME

This query interface allows to search and to request raw observational data taken by telescopes of the La Silla Paranal Observatory.  
 New features 9 November 2020:

- You can now limit your queries to either optical or infrared instruments using the MarkOptical and MarkInfrared buttons in the instrument blue panel
- When looking for images in a certain bandpass, constraints can now be provided using wavelengths in nm, or standard bandpass name (see [help page](#))
- At request time, you can decide whether to download any of the following:
  - the selected raw data,
  - the raw or processed calibrations needed to process the selected raw data,
  - the pipeline-processed data generated out of the selected raw data (if they exist)

Read more...

Search [Reset] Output preferences: html table Return max 20000 rows. All Fields Syntax Help

**Target, Program, and Scheduling Information**

Target Name  Beta Pictoris Resolved by SIMBAD  
 RA  DEC  J2000  
 Search Box  Input RA(h) DEC(deg)  
 Output  Sexagesimal (h, deg)  
 List of Targets Choose File No file chosen

Night  (YYYY MM(M) DD)  
 Otherwise give a query range using the following start/end dates:  
 Start 2020 02 07 12 hrs [UT] End 2023 02 09 12 hrs [UT]  
 Program ID  Program Type  Any  
 PI  SY  Any  
 Title

**Observing Information**

MarkOptical MarkInfrared

**Imaging** ALL NONE  
 EFOSC2/LaSilla  
 EMMI/LaSilla  
 FORS1/VLT  
 FORS2/VLT  
 HAWKI/VLT  
 GROND/LaSilla  
 ISAAC/VLT  
 NACO/VLT  
 OMEGACAM/VST  
 SOFI/LaSilla  
 SPHERE/VLT  
 SUSI2/LaSilla  
 TIMMI2/LaSilla  
 VIMOS/VLT  
 VIRCAM/VISTA  
 VISIR/VLT  
 WEI/LaSilla  
 XSHOOTER/VLT

**Spectroscopy** ALL NONE  
 CES/LaSilla  
 CRIRES/VLT  
 EFOSC2/LaSilla  
 EMMI/LaSilla  
 ESPRESSO/VLT  
 FEROS/LaSilla  
 FORS1/VLT  
 FORS2/VLT  
 GIRAFFE/VLT  
 HARPS/LaSilla  
 ISAAC/VLT  
 KMOS/VLT  
 MUSE/VLT  
 NACO/VLT  
 SINFONI/VLT  
 SOFI/LaSilla  
 SPHERE/VLT  
 TIMMI2/LaSilla  
 UVES/VLT  
 VIMOS/VLT  
 VISIR/VLT  
 XSHOOTER/VLT

**Interferometry** ALL NONE  
 AMBER/VLT  
 GRAVITY/VLT  
 MATISSE/VLT  
 MIDI/VLT  
 PIONIER/VLT  
 VINCI/VLT  
**Polarimetry** ALL NONE  
 EFOSC2/LaSilla  
 FORS1/VLT  
 FORS2/VLT  
 ISAAC/VLT  
 NACO/VLT  
 SOFI/LaSilla  
 SPHERE/VLT  
**Coronagraphy** ALL NONE  
 EFOSC2/LaSilla  
 NACO/VLT  
 SPHERE/VLT  
 VISIR/VLT

**Other** ALL NONE  
 APICAM/Paranal  
 BQL/APEX  
 HET/APEX  
 LGSE/VLT  
 MAD/VLT  
 MASCOT/Paranal  
 WFCAM/UKIRT  
**Sparse Aperture Mask** ALL NONE  
 NACO/VLT  
 SPHERE/VLT  
 VISIR/VLT

Category   
 SCIENCE  
 CALIB  
 ACQUISITION

**Data Product Info**  
 Type  Any  
 User defined input:   
 Mode  IFU  
 User defined input:   
 Dataset ID   
 Orig Name   
 Release Date   
 OB Name   
 OB ID   
 TPL START   
**Instrumental Setup**  
 TPL ID   
 Exptime   
 (imaging only) Filter bandpass   
 (imaging only) Bandpass FWHM   
 Grism   
 Grating   
 Slit

Instrument & Mode  ((ins\_id like 'SPHERE%' AND ((dp\_tech like 'IFU%' OR dp\_tech like 'SPECTRUM%') OR (dp\_cat != 'SCIENCE'))))

Figure 2.6: The ESO Raw Data Archive Database Portal. Currently, check-marked boxes indicate the type of data that was obtained for the use of this thesis. Figure Credit: European Southern Observatory [2021b]

with ADI, RDI, and SDI techniques [Soummer et al., 2012]. It is stable, extensively tested, and actively maintained. We have used it in this project to analyze the data obtained by SPHERE, but its capabilities extend to other imagers' data, for example the NaCo Nasmyth Adaptive Optics System (NACO) [Lenzen et al., 2003] [Rousset et al., 2003].

## 2.5 Differential imaging: ASDI, SADI, CODI

The work done in this thesis builds on the work of others. ADI, SDI, and PCA have been present in the literature for several years. The novelty of this project has been to combine these practices and determine the effectiveness of ASDI and SADI both while using PCA. This kind of combination relies on performing observations over sufficiently broad durations of time or wavelengths. Figure 2.7 shows how observations of a (central) star and its environment will appear to rotate because of the configuration of altitude-azimuth telescopes and the rotation of the earth. This research and the individual imaging techniques capitalize on these types of phenomena.

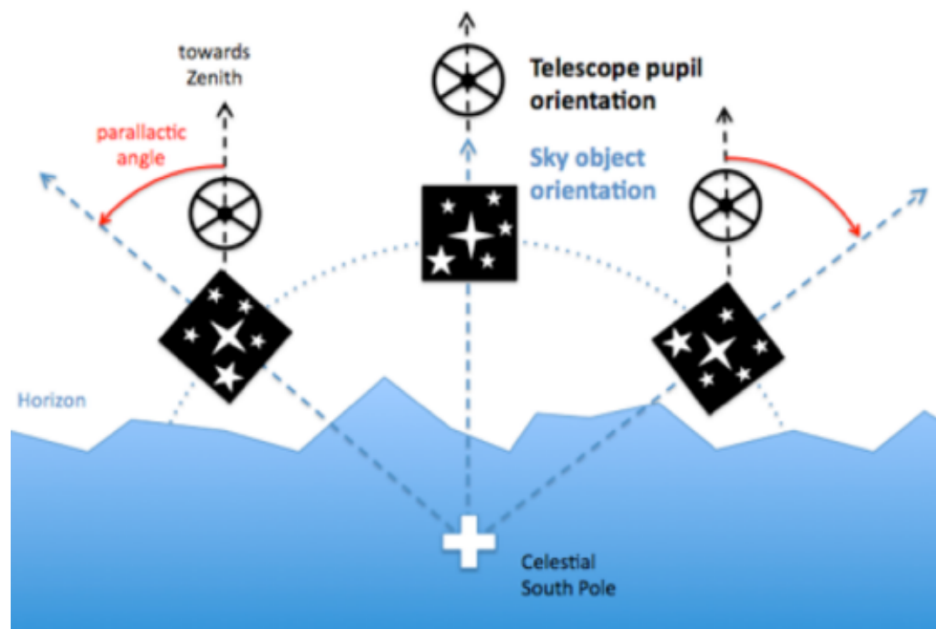


Figure 2.7: Rotation of viewing perspective of altitude-azimuth (Alt-Az) telescopes, which is caused by the apparent motion of the earth. Long-term viewing for small objects (stars) in the center of the field of view is a standard practice. Peripheral objects (exoplanets) appear to rotate around their stars from earth throughout the observational time. Figure Credit: [Gómez, 2016] and Christian Thalmann

### ADI

Angular Differential Imaging (ADI) is a method of combining the light from multiple exposures or images such that in the resulting images, starlight is suppressed, and planet light is captured. The work of Marois et al. [2006] provides a wealth of information on ADI, and only a brief summary is given here. Due to the rotation of the earth and apparent motion, an altitude-azimuth telescope, or a telescope in an altitude-azimuth configuration, over time will capture

images with angular rotation within them. At the exact center, there is no rotation; as a planet's radial separation from an image center increases, so does the extent of rotation in images. Therefore, any companion body would also appear to rotate around the star over time. This means that if an average image of all images is obtained, it will have the signal from the planet spread or smeared over some degree of arc around the star. This average signal can be used to make a series of new images, which show the difference between any one image and the average of all images. At this point, we have relatively little starlight and a hint of a planet's signal in a different place on an arc of each different image. Finally, if we assume the orbital motion of a planet around a star is negligible on the timescale of a single night of observations, then we can calculate the amount of rotation that has occurred during the image exposures. Backtracking, or de-rotating, this makes the images line up on the same spot. Stacking these de-rotated images then allows the planet signal from each picture to grow to be the planet signal for all pictures [Marois et al., 2006]. A visualization of ADI is shown in Figure 2.8 in the methodology section.

Various complexities will make this data reduction less than perfect. AO is capable of improving ground-based detections, but optical path aberrations and vibrations persist and observations from space will always be superior. Yet even from space, other phenomena like stellar winds, space weather, and astroseismologic effects can increase the amount of stellar light in one or two exposures, while leaving the others relatively unaffected. This means the average image used as a subtraction for all of the images will be insufficient for the one or two exposures mentioned, and excessively bright in all of the other images. This in turn can result in modest swings in the luminosity of the planet and an uneven weighting of individual exposures in the making of average exposures (in the final set of images).

## SDI

Whereas ADI functions on the basis of planetary position changing within a field of view with respect to time, Spectral Differential Imaging (SDI) functions on the basis of wavelength. Stars are large massive objects, but their distances to us, even for the closest ones, are so great that the light coming from all known stars behaves as if it is from a point source. Whether it is with our eyes or with the photodetectors that technology has to offer, the light from this point-like source appears to have an actual area on the sky. This area is the distribution of diffracted light, and the distribution is referred to as the Point Spread Function (PSF). Objects that emit light at multiple wavelengths will have PSFs for each wavelength emitted. The shape of PSFs is approximately equal for each wavelength; but the wings will change. That is, low-energy long-wavelength light will be detected broadly around the star, while high-energy short-wavelength light will be detected only relatively close to the star. Given a constant telescope diameter, there is a proportional relationship between the size of a PSF and the wavelength one is observing at:

$$PSF \propto \lambda \quad (2.1)$$

This can be used to manipulate images so that they can form a single image with minimal stellar light and planetary signal additively stacked in one location.

The figure 2.9 shows the process of SDI data reduction. It begins by expanding or stretching all of the exposure images (except the largest wavelength's image) by a factor that varies with wavelength. This allows alignment of the spectral noise from each observation to occur within the same radius on each new image. Furthermore, this will separate (spread out) any and

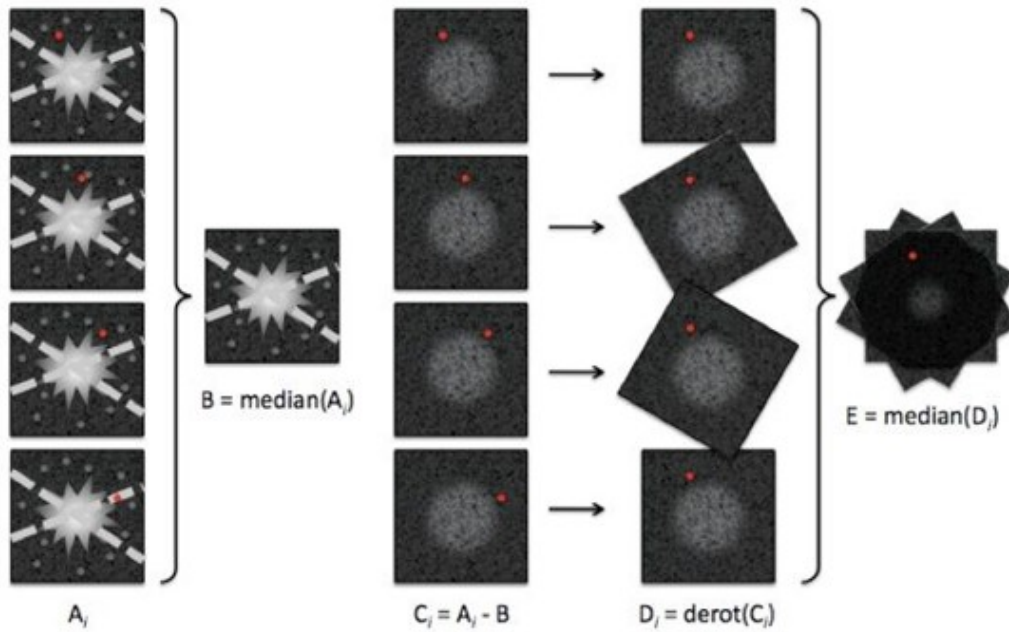


Figure 2.8: ADI descriptive diagram. The telescope and detector capture images  $A_i$ . An average image from all  $A_i$  forms image  $B$ . Each Image  $A_i$  is subtracted by the  $B$  image, which forms  $C_i$ .  $C_i$  images are de-rotated an amount proportional to the time difference taken of the reference image (here  $i = 1$ ), which forms  $D_i$ . The  $D_i$  images are stacked and averaged to form the final image,  $E$ . Figure Credit: [Gómez, 2016] and Christian Thalmann

all signal from a planet onto different radii for each of the new images. An average picture is obtained after cropping the outer edges of all pictures that were expanded. This average picture is then compressed down to the sizes of the original images (based on their observational wavelength). This average image at each wavelength's dimensions is subtracted from each of the original images, leaving a set of images with very little starlight, but with the planet's position still spread out over a different radius for each image. Finally, the low starlight images are expanded by the same wavelength-dependent factor as before, resulting in the frames of each image aligning to form a final image with the planet light all at the same point [Kiefer et al., 2021].

Because SDI works on the basis of radiance, it becomes a function of radius to the star. This is in contrast to ADI, which operated on field of view changes over time and were thus a function of angle or  $\theta$ , and time itself. Because SDI relies on a set of images taken during a single exposure of time, it is a superior technique for making exoplanet detections close to a star. This is because stellar speckles will change over the course of time, and cause many false positives or negatives when using the ADI technique. The weakness of SDI is that the expansion, averaging, compression, subtraction, and expansion again means that the edges of the field of view will be cropped off. Thus, it might be effective enough to detect a planet with large separation, but it might not because the planet would be in the region that is outside of the maximum image radius.

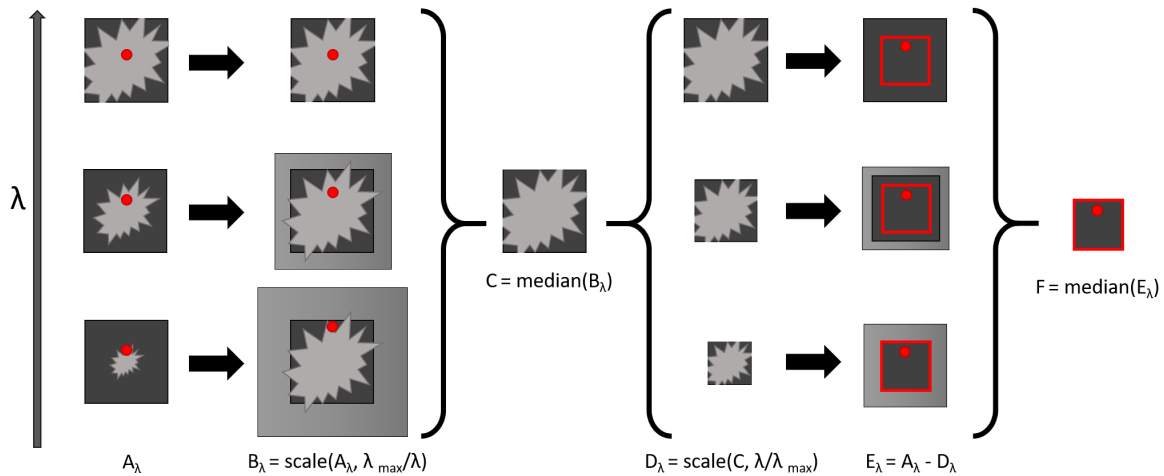


Figure 2.9: SDI descriptive diagram. Images  $A_\lambda$  are taken, the high frequency images are stretched by a scaling factor inversely proportional to  $\lambda$  making  $B_\lambda$ . The stretched images' edges are cropped off. These are averaged to form a median image,  $C_\lambda$ . This is shrunk to multiple sizes; the new set is  $D_\lambda$ . The  $A_\lambda$  images are subtracted by the  $D_\lambda$  images, making  $E_\lambda$ . A median of the  $E_\lambda$  images cut to the smallest  $E_\lambda$  image's size makes a final image,  $F$ . Figure Credit: Kiefer et al. [2021]

## Combined Differential Imaging

As the name suggests, this technique combines aspects of ADI and SDI. Initially, an SDI-like approach is performed: All exposures are expanded by a scaling factor which is proportional to the ratio between each wavelengths' exposure and the maximum wavelength's exposure. An average image of the PSFs (now all being on the same order of visible size) is obtained. The average image is subtracted from each of the images, and then all images are returned to their original sizes by an inverse of the scaling factor from the beginning. Subsequently, an ADI-like technique is applied: These equivalent images are de-rotated and stacked to create the finished image [Kiefer et al., 2021].

## 2.6 Principal Component Analysis

Principal Component Analysis (PCA) is a tool to reduce all exposures from a dataset by modeling the stellar PSF and then subtracting it out of the images that are given to it. In PynPoint, PCA computations are done by the program Scikit-learn [Pedregosa et al., 2011]. Mathematically, PCA is accomplished by generating an orthonormal basis,  $B$ :

$$B = B_1, B_2, \dots, B_N \quad (2.2)$$

The pieces of the basis are called principal components. The first component ( $B_1$ ) characterizes the direction of maximum variance in the basis. The second component ( $B_2$ ) corresponds to the direction of maximum variance orthogonal to the first component. More and more  $B_i$  terms are added to the basis until an orthonormal basis is established. The usefulness of this

method arises because an exoplanet (or any other companion body) migrates between the exposures, and will thus not contribute to the variance of the PSF significantly. This means that the first principal components will only reduce the stellar PSF, and leave the planetary signal alone in the vast majority of situations. This means if the basis is truncated as:

$$B' = B_1, B_2, \dots, B_n \quad (2.3)$$

where  $n \ll N$  then  $B'$  is a model of the stellar PSF, which can be used to subtract out speckles and other stellar light contaminants. With the speckle noise reduced by the subtraction, the images can be de-rotated and stacked to augment the signal of collected of the planet. When  $n$  is very small, the stellar noise dominates and PCA might as well not be done, no change is made, and no improvements will be seen. When  $n$  is large, or as  $n$  approaches  $N$ , the PSF of the star will be effectively removed, but much if not all of the planetary signal will also be removed. This means that some intermediate value should optimize the detection scheme of an exoplanet (given the conditions of a particular observation). The size of the best basis to use for detections has been studied in this research; the plots in the results section show what PCAs are best, but we have found that the best intermediate values usually range between two and six.

# Chapter 3

## Results

We present the findings of our data and results for the Beta Pictoris system. Beta Pictoris (beta Pic), also known as HD 39060, is a stellar system that lies approximately 60 light-years (20 parsecs) away Gaia Collaboration [2020]. The discovery of its circumstellar disk is seen on the left in Figure 3.1. The star's known planets orbit within 11 AU, and are not seen in the wide angle (left) figure image, but the planet b is seen in the newer (right) figure image. Attendance at the 2022 ALMA Archive Science School led to a personal Beta Pic image generation based on radial velocity measurements of the disk, which is seen in the appendix (C.1).

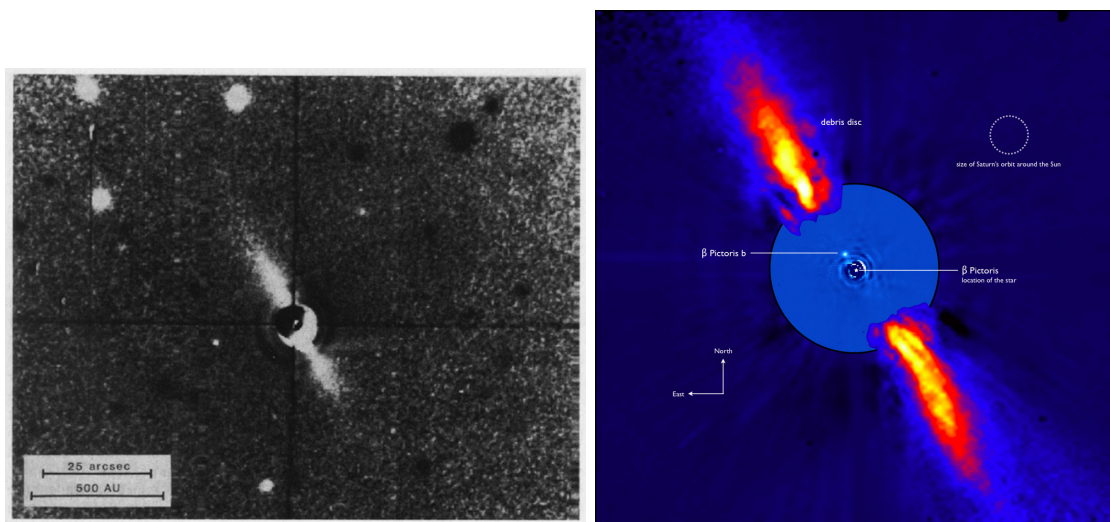


Figure 3.1: Left: The 1984 discovery of a circumstellar disk around Beta Pictoris image. Figure credit: [Smith and Terrile, 1984]. Right: An composite infrared image from 2008 with annotations of the Beta Pictoris system. Figure credit: [European Southern Observatory, a].

In this chapter, we first discuss how SPHERE's saved data is to be understood; then we discuss the nature of the observations analyzed; the heart of the research is in sections on the spectral characteristics, signal-to-noise, and principal component analysis of the different observations; finally modeling of the results is shown, which uniquely quantifies many of the

previous results and highlights the efforts of characterizing and possibly mitigating a data artifact of signal suppression.

### 3.1 Interpreting SPHERE's Data

Figures in this thesis use wavelength channels (or index numbers) on the x-axis frequently. These numbers come from the SPHERE instrument at the VLT, discreetly from 1 to 39. This ease of viewing is supported by table 3.1 as the numbers of wavelength detector channels are matched with their corresponding wavelength sensitivity ranges. The 39 wavelength channels denote the middle of the wavelength bin; the difference between two numbers ( $\sim 10\mu m$ ) is the width of the bins.

Wavelength Channel Index Numbers & Wavelength Ranges			
Wavelength Channel No.	Wavelength [ $\mu m$ ]	Wavelength Channel No.	Wavelength [ $\mu m$ ]
1	954.3	21	1159.4
2	962.6	22	1169.3
3	971.8	23	1179.4
4	981.9	24	1189.4
5	991.6	25	1199.5
6	1001.7	26	1209.9
7	1012.7	27	1220.0
8	1023.3	28	1230.0
9	1033.6	29	1240.6
10	1043.9	30	1250.6
11	1054.2	31	1261.0
12	1064.9	32	1271.4
13	1075.5	33	1281.9
14	1085.5	34	1291.7
15	1095.4	35	1300.6
16	1105.1	36	1309.6
17	1115.2	37	1318.8
18	1127.1	38	1327.1
19	1138.8	39	1333.6
20	1149.4		

Table 3.1: Wavelength Detection Channel Ranges of the SPHERE instrument at the VLT. The numbers indicate the middle of the wavelength bin in micrometers; the difference between two numbers ( $\sim 10\mu m$ ) is the width of the bins. Note: The visible spectrum ends at  $\sim 0.7\mu m$ ; SPHERE straddles the boarder between IR and microwave light.

### 3.2 Observation Times and Parameters

Throughout this thesis we will discuss Beta Pictoris and its exoplanets; especially with regard to four observations made of it in 2015, 2016, 2018, and 2020; exact dates are tabulated in

3.2.

Times of Beta Pic Observations		
Date	Time	Exposures
2015-11-30	5:18:29-6:51:36	10
2016-11-18	5:42:12-6:06:14	25
2018-12-15	4:26:36-5:33:46	32
2020-02-08	0:40:47-1:26:53	32

Table 3.2: Observation Times of Beta Pictoris made by the SPHERE instrument at the VLT.

Physically, beta Pic b is compared to Jupiter as it has a mass of  $M = 13M_{Jup}$ ,  $T_{eff} = 1724K$ ,  $R = 1.46R_{Jup}$ , and  $\log(g) = 4.18$  Chilcote et al. [2017]. However, given that Jupiter is (by definition)  $1M_{Jup}$  and significantly cooler than 1724 K, as calculated by,

$$T_{eff} = \sqrt[4]{\frac{L(1-a)}{16\pi\sigma D^2}} \quad (3.1)$$

where  $L$  is the star's luminosity,  $a$  is the planetary albedo,  $\sigma$  is the Stefan–Boltzmann constant, and  $D$  is the distance between the star and the planet; Jupiter has a  $T_{eff} = 90K$ , while its (thermal) surface temperatures with respect to atmospheric depth have been approximated as  $T_{(P=0.1 \text{ bar})} = 130 \text{ K}$  and  $T_{(P=1 \text{ bar})} = 170 \text{ K}$  Stevenson [2020]) we can fairly say that even though Jupiter is the most similar, our solar system does not contain a planet quite like beta Pic b.

The plane of its debris disk and exoplanetary orbits is almost edge-on or perpendicular to the plane of the sky; its exoplanets beta Pic b and beta Pic c orbit with an inclination of 89 degrees Feng et al. [2022]. As such, long-term direct imaging observations should show the host star's planets disappearing and appearing from in front or behind the star and then moving away until the visual separation is maximized (before moving in again). We believe this is happening in the images obtained from PynPoint as seen in Figure 3.2. The fourth image of the figure will be the topic of much analysis in this thesis. The images were generated from the raw data using PynPoint performing an ASDI reduction of a median wavelength scaling. The image shows the light signals received in the 1276-1286  $\mu m$  wavelength region of light (the 33rd wavelength channel). Later figures (3.5 & 3.6) illuminate why this bin of light was selected.

### 3.3 Spectral characteristics of signal and PCA

The signal-to-noise ratio is a parameter that is commonly used to quantify how good a detection is.

$$\frac{Signal}{Noise} = S/N = SNR \quad (3.2)$$

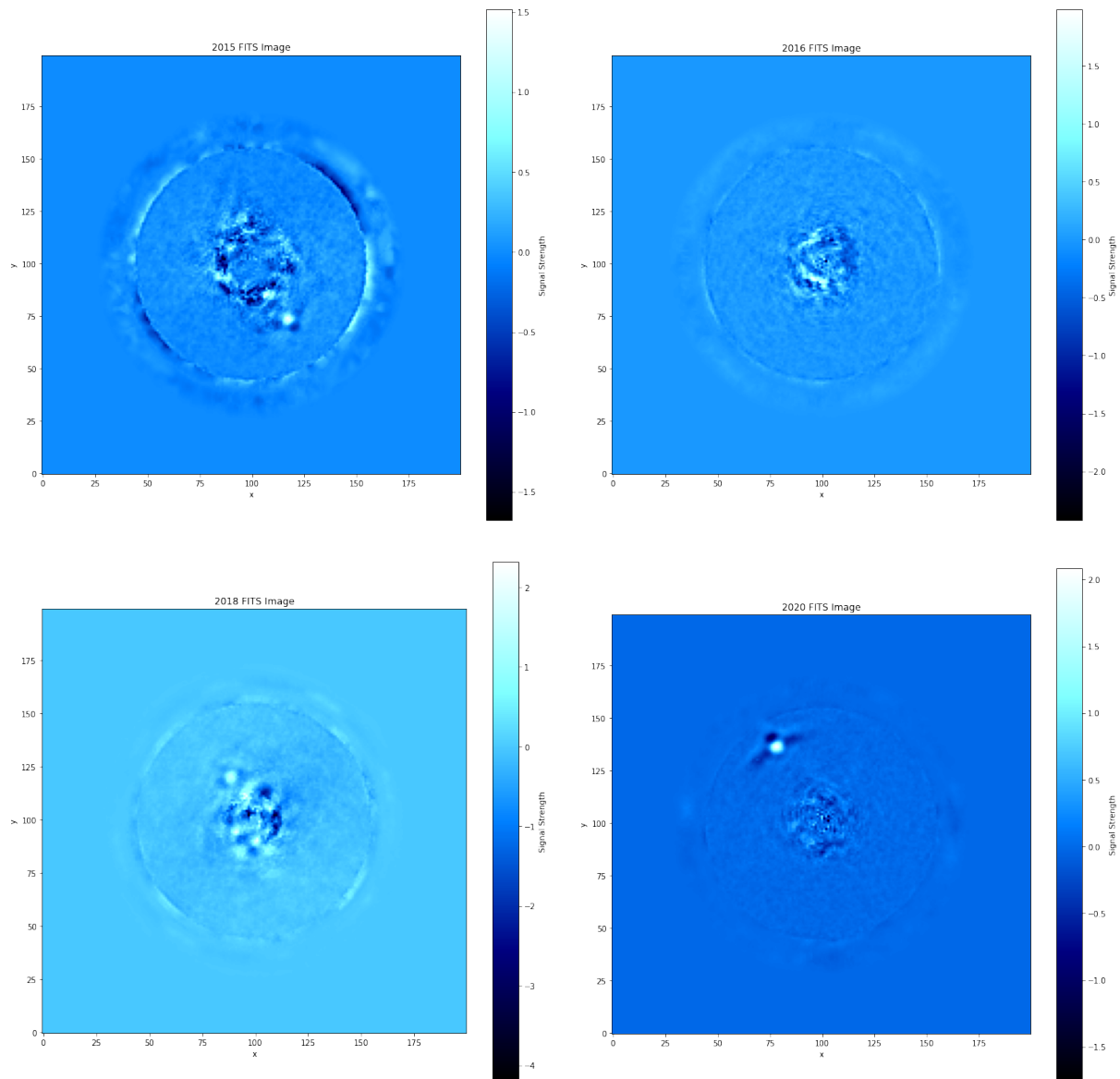


Figure 3.2: Images of Beta Pictoris system taken over multiple years. Ordered left to right from top to bottom, as first to fourth, the planet beta Pic b is visible on the lower-right of the first image, has minimal SNR and no separate signal in the second image, is seen in the upper-left of the third image, and is most clearly visible in the upper-left of the fourth image. Note: The different colors of the backgrounds are primarily due to the depth of the largest minima in the speckle noise in each picture, each image's background color corresponds to slightly above zero in its own color bar.

Like the standard distribution in statistics, the signal-to-noise ratio (along with other metrics) is used to determine if some object or phenomena is really present, or if some kind of random or systematic error is occurring in the telescope, local environment, or other outside influence. In this research, SNR is calculated from the ratio of the flux of the pixel element encapsulating the planet with respect to the average flux from pixel elements at the same radial separation.

$$SNR_p = \frac{\text{average flux from planetary pixels}}{\text{average flux from background pixels at equal separation}} = \frac{\Phi_p}{\Phi_{bg}} \quad (3.3)$$

Analogous to the use of the popular "6-sigma ( $6\sigma$ )" in industrial quality assurance and control, a large signal-to-noise ratio indicates that the likelihood of something (i.e., a planet) being there is high.

There is useful information that is not clearly captured from a single image in a single observation. Figure 3.3 shows the signal-to-noise ratios of the planet on wavelength channel for all possible PCA combinations up to a  $10 \times 10$  matrix for ADI and SDI on the observation made in the year 2020. The data reductions possible from different PCA combinations lead to different signal intensities for each wavelength (index). Peaks and troughs will align (approximately) for all different wavelengths and PCAs. However, the height of peaks and troughs at one wavelength will vary with respect to PCAs. Likewise, the height of peaks and troughs at one PCA will vary with wavelength. The result is similar, but not the same as, a (partial) spectra of the planet.

The known planet position was obtained in 2015 from Lagrange et al. [2019] Later observations were published in Lagrange et al. [2020]; separation in the units of pixels was accomplished by converting right ascension and declination given in the literature into x and y pixel positions.

Figure 3.4 shows a zoomed in cut of the highest peak's signal-to-noise ratio. Regardless of the PCA applied to the data, these high wavelength channels capture the greatest SNR of Beta Pictoris b. Interestingly, we can see that the differences in PCA done result in significant differences between the SNRs' peak heights. At the highest point of the strongest peak, the PCA combination can yield an SNR of approximately 128, while at the highest point of the weakest peak, the SNR falls off after reaching 17. This factor of 7.5 indicates PCA is indeed a method that can be useful in data reduction techniques.

If we select the channel for which we obtain the highest SNR, we can study the dependence of the SNR or the signal with the azimuthal angle. Figure 3.5 shows the relationship between signal and azimuthal angle (of the 2020 observation's 33rd wavelength channel). The vibrating noise along most of the plot is to be expected. The dips before and after the peak, and the peak's shape and height are of great interest in this, and potentially future, research. The peak height is so much more than the noise around before and after, as expected in the case of a real detection. This is not possible in an earlier (2016) observation, where the conjunction makes the noise as large as or larger than any signal detection.

Complementary to the signal detected over varying angles, Figure 3.6 shows the signal detected over increasing radius. Naturally, the angle of the radius line has been chosen to match the angle that corresponded to the peak angle of the previous (graph and) analysis. Here in the 2020 observation, we find chaotic behavior in the radii close to the star, a large peak at a middle distance to the star, and then a noise close to 0 signal far away from the

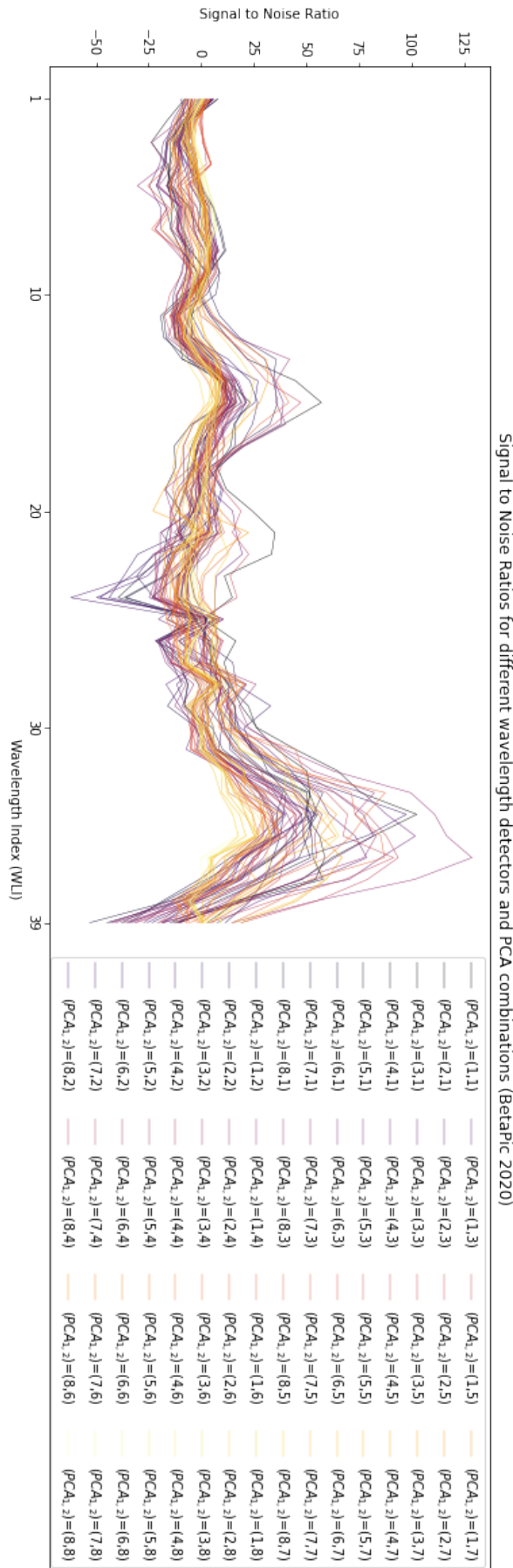


Figure 3.3: Signal-to-noise ratios as functions of wavelength channel index for all possible combinations of ADI and SDI PCA up to 8 components each on the 2020 beta Pic observation.

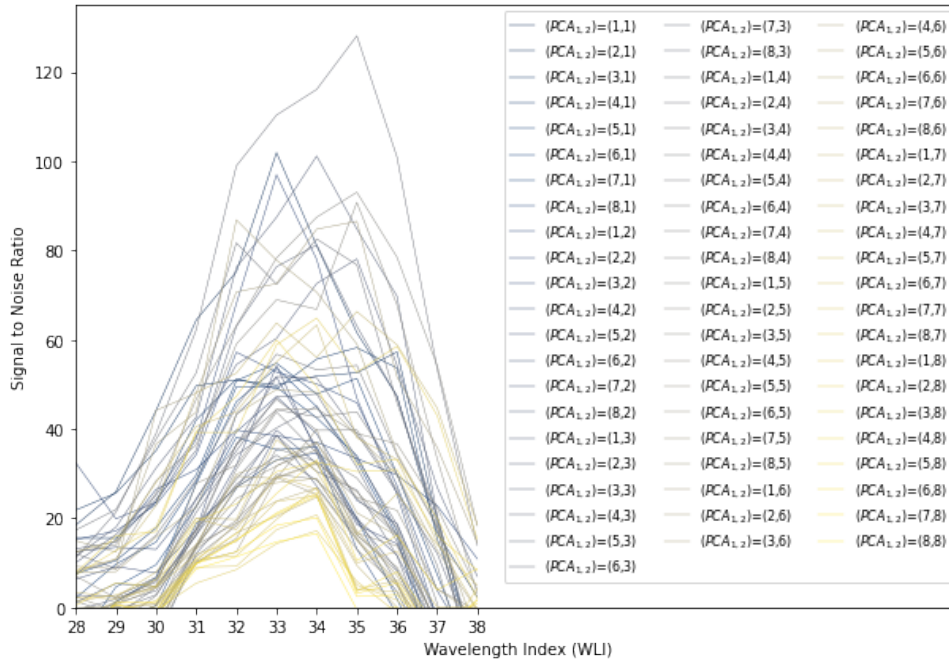


Figure 3.4: Zoom in on peak region of previous Figure 3.3. The highest peak occurs at an SNR of  $\sim 128$ , while the lowest peak is at  $\sim 17$  a factor of  $\sim 7.5$ ). The highest peaks have combinations which are scattered around different PCA components. The many light yellow lines at the bottom of the peak come from high SDI PCAs; this is indicative of overfitting, and using such will lead to inferior models.

star. These three phenomena can be interpreted as the speckle noise of the star that arises from a bleeding of the stellar light around SPHERE's coronagraph, the signal of the planet in a clearly high-quality detection, and the background noise or apparent nothingness that is below SPHERE's detection limits. The maxima of the radius and angle provide a coordinate for the observed position of the planet.

Using the observed planet position from the maximum signal strengths from the previous two plots and the images in 3.2 we can visually verify that the lines passing through the peak maxima are in fact the lines that run between the star and planet. This is seen in Figure 3.7. The line connects the star (center of the image) with the maximal peak signal of the planet, but we can see that in this image (at this wavelength range) the planet's demarcated position is located slightly outside of the visual center of the signal (PSF). This will be analyzed in great depth in upcoming sections: We will plot planetary signal peaks over all wavelengths with respect to angular separation, make continuous curve fitted models of planet signal from the relatively discrete or distantly connected data (points), and compare our models' planet locations with the known literature values.

### 3.4 Signal-to-noise and PCA – Heat Maps

Much of the inspiration of this research comes from Kiefer et al. [2021]. One area of research that was only very briefly investigated there was the scope and optimization of PCAs in the data reduction. This work has expanded such earlier results. It is important to determine

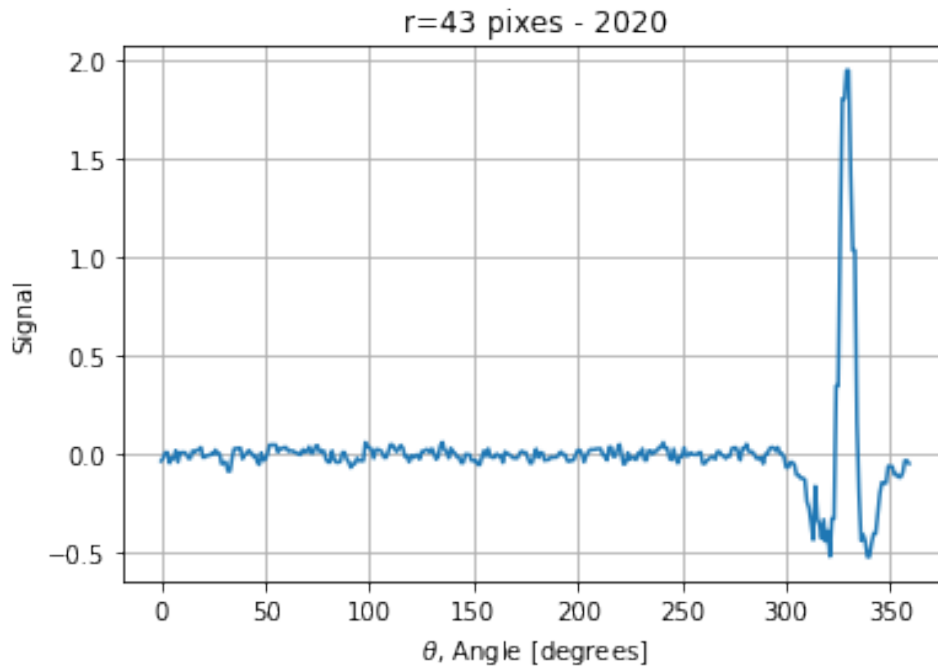


Figure 3.5: Signal plotted over parallactic angle at a radius=43 pixels. The small bumps about a zero value are typical background noise, the dips before and after the peak are the consequence of the (ADI) data reduction method, and the large peak is the planetary signal. Referencing Figure 3.2, the zero angle occurs towards the north/upwards direction, and then proceeds in a counterclockwise direction.

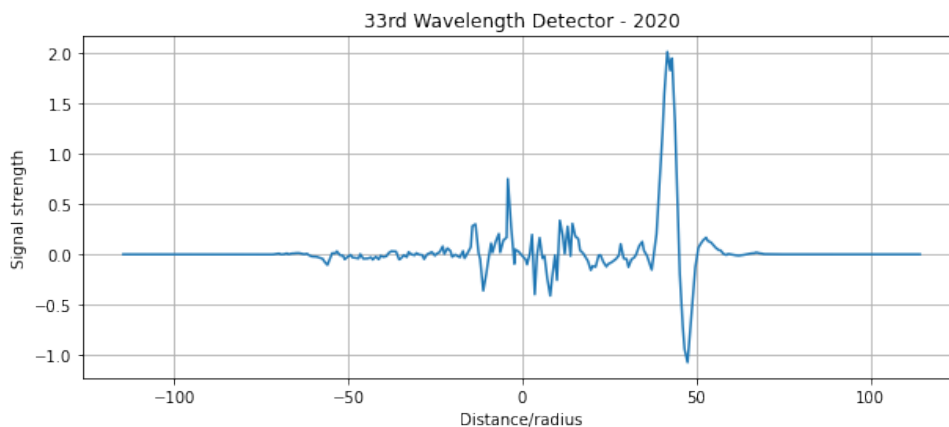


Figure 3.6: Signal plotted on distance/radius to the host star for a single wavelength channel in the 2020 Beta Pictoris observation. The signal around zero is thought to be speckle noise; the large peak at a distance of  $\sim 43$  pixels from the center is deemed the planet. The flattening of the signal near its ends suggests there are no more large or bright planets like Beta Pictoris b at larger orbits (within the orbital distance observed). The large drop in signal after the peak is an artifact of the data reduction (SDI) process.

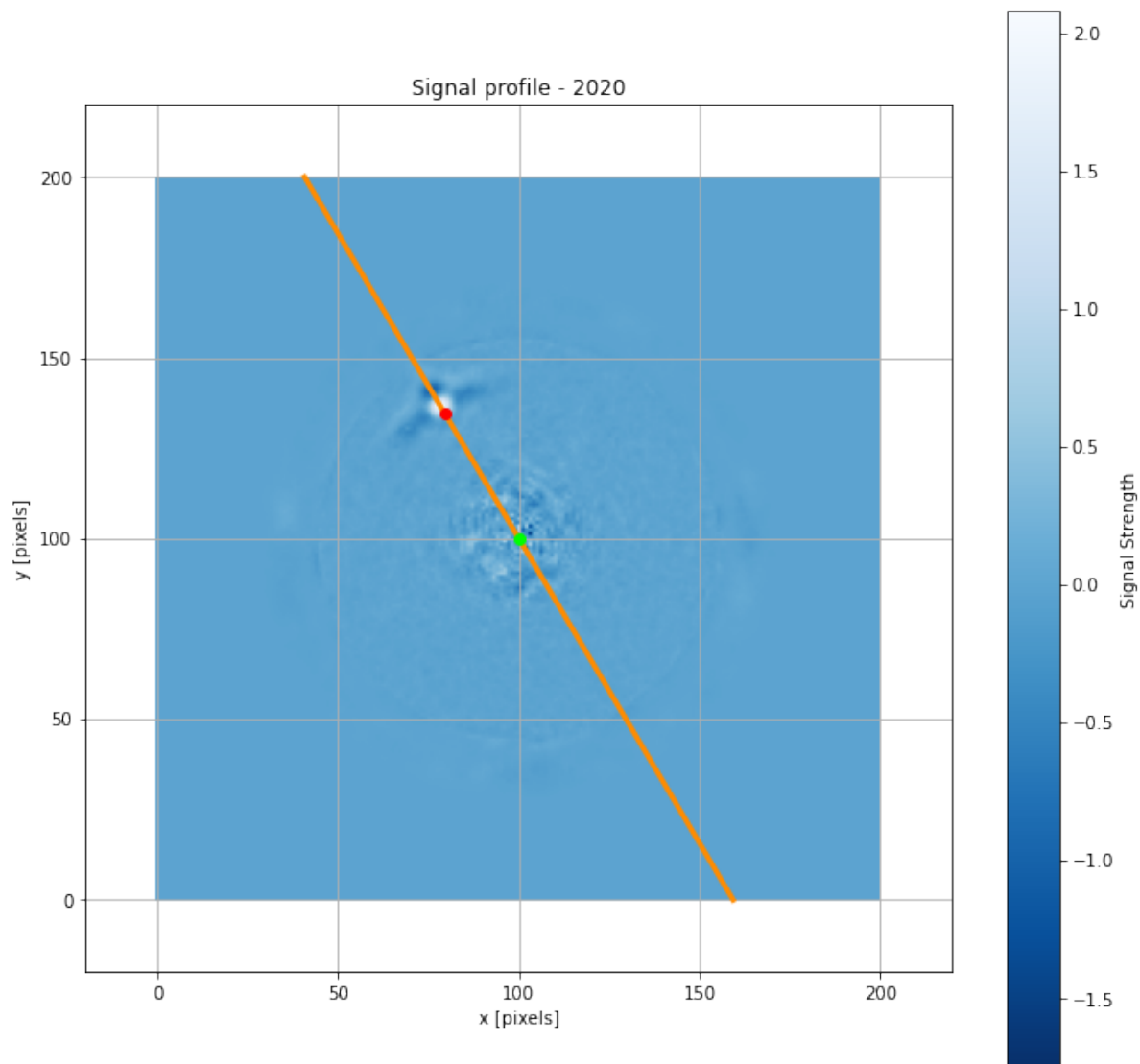


Figure 3.7: A combination of a (data) reduced image from SPHERE and the calculated line intersecting the planet position (red dot) and central star (green dot). The pixels underneath the solid orange line are identified and used in the determination of signal behavior as a function of (linear) distance to the star.

which combination of PCAs is optimal because it leads to a maximization of the SNR. This allows for tighter constraints on parameters, like mass and semi-major axis, to be placed on the planet and its spectrum. Figure 3.8 shows the relationship between three variables (PCAs of ADI, PCAs of SDI, and maximal SNR) in what is called a heat map. The figure's signal-to-noise ratios are seen as changing gradations of color (yellow being largest); they are functions of different combinations of ASDI and SADI principal components. We see that in the best detection (2020) that using 6 ADI and 2 SDI PCAs provides the largest signal-to-noise ratio. Having a maximum is a good way to begin, but the decay beyond the maximum is a particularly useful result, as it suggests that we have covered the entire relevant parameter space in this research.

The slight difference in Figure 3.8 between the axes of the 2015 (bottom) observation compared to the other years. This is because the data available in the ESO Archive for this earliest observation limits performing data reductions with maximum PCAs of  $n - 1$ , where  $n = 10$ , so nine, where  $n$  is the number of observations made (see the 10 exposures in Table 3.2).

These heat maps are a useful way to display many comparisons between PCAs, but it homogenizes a distribution of signal data into a simple maximum. Therefore, some diverse data sets are now investigated in their own rights.

Considering the wavelength dependence of signal-to-noise for different PCAs is a valuable line of inquiry and study. If optimization is the goal, and a comparison of the best that each PCA combination can provide is sought, then the maximum of the dispersed SNR information is selected and plotted in a heat map with respect to the different possible PCA combinations. The results of this are seen in Figure 3.8.

Of the many possible ways, this research approached calculating signal-to-noise ratios by comparisons of similarly defined planet position areas in what we call the ring of circles method. A picture is worth a thousand words here, and is located in Figure 3.10. This circles within ring approach allows us to define the signal all around the edge of the naturally occurring point spread function (PSF). It also uses the noise that naturally occurs at the level of separation between the host star and exoplanet; except for the rare case of a system that is perfectly perpendicular to our line of sight, this distance and thus ring (in which there are circles) grow, shrink, and can change dramatically with time.

Thoroughness and the most robust testing would compare the signal-to-noise ratios obtained from the ring of circles method to other methods. Though different results might be obtained by performing a fragment within solid ring method, a planet circle within local environmental circle method, or a circle within (extra) thick semi (or quarter) circle method, these methodologies have been tabled for future investigations that are beyond the scope of this project.

### 3.5 Signal, distance, and all wavelength channels

The simpler and more intuitive plots of signal with respect to angle and radii seen in Figures 3.5 and 3.6 are the basis of studying how radii is a key component in SDI data reduction. Recall how the method of SDI expands and shrinks multiple wavelength-based exposures, which leads to radial migration of the planetary signal between them. A more complex plot of

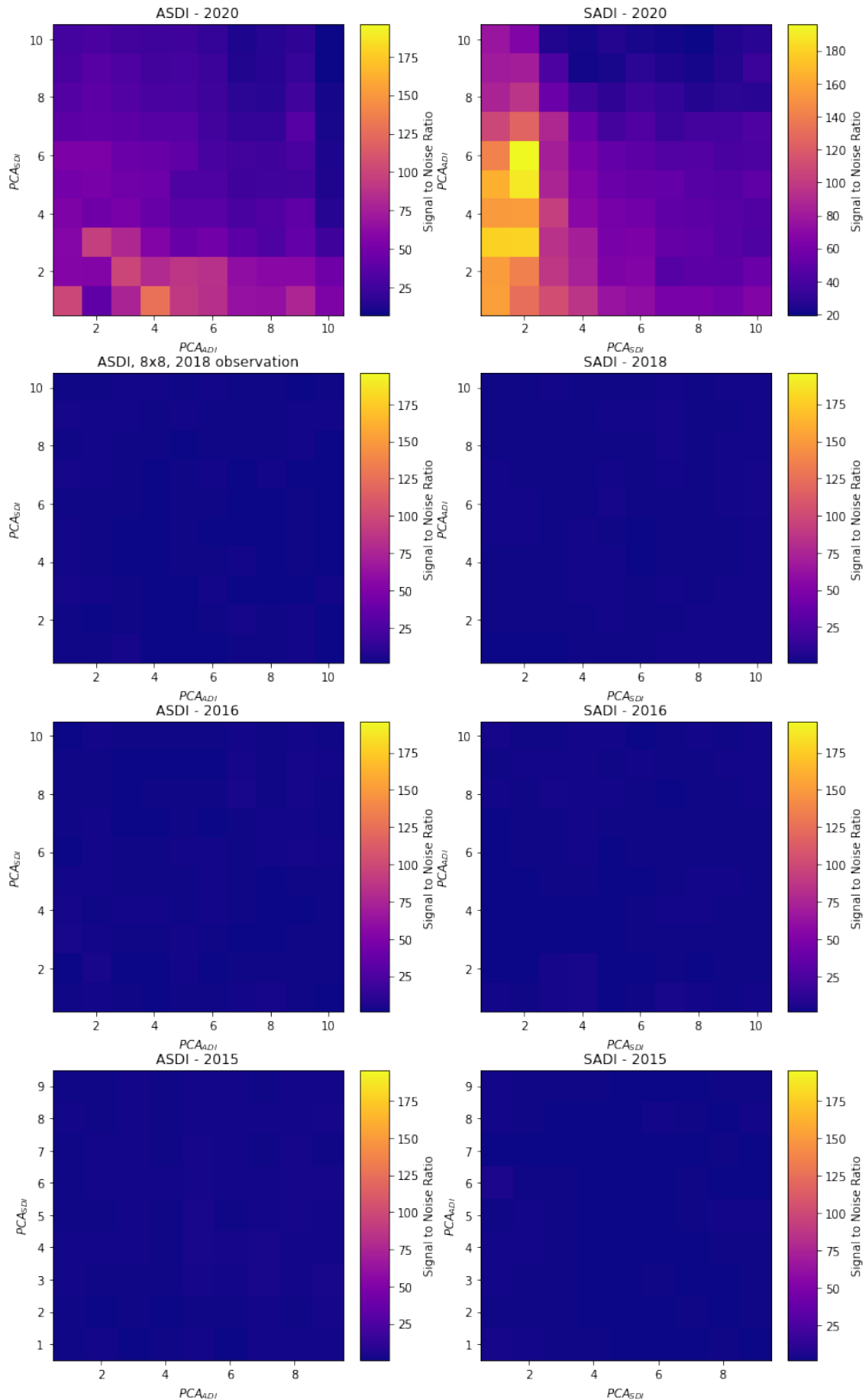


Figure 3.8: Heat Maps of maximum Signal to Noise ratios for different combinations of PCA components in the ASDI and SADI data reductions of Beta Pictoris b during the four observations. Note: The Apparent lack of signal in the results of the 2018, 2016, and 2015 are caused by the range of the color bar, which is the same in all plots. Figure 3.9 shows the other observations' maximum SNRs by using unequal color bars.

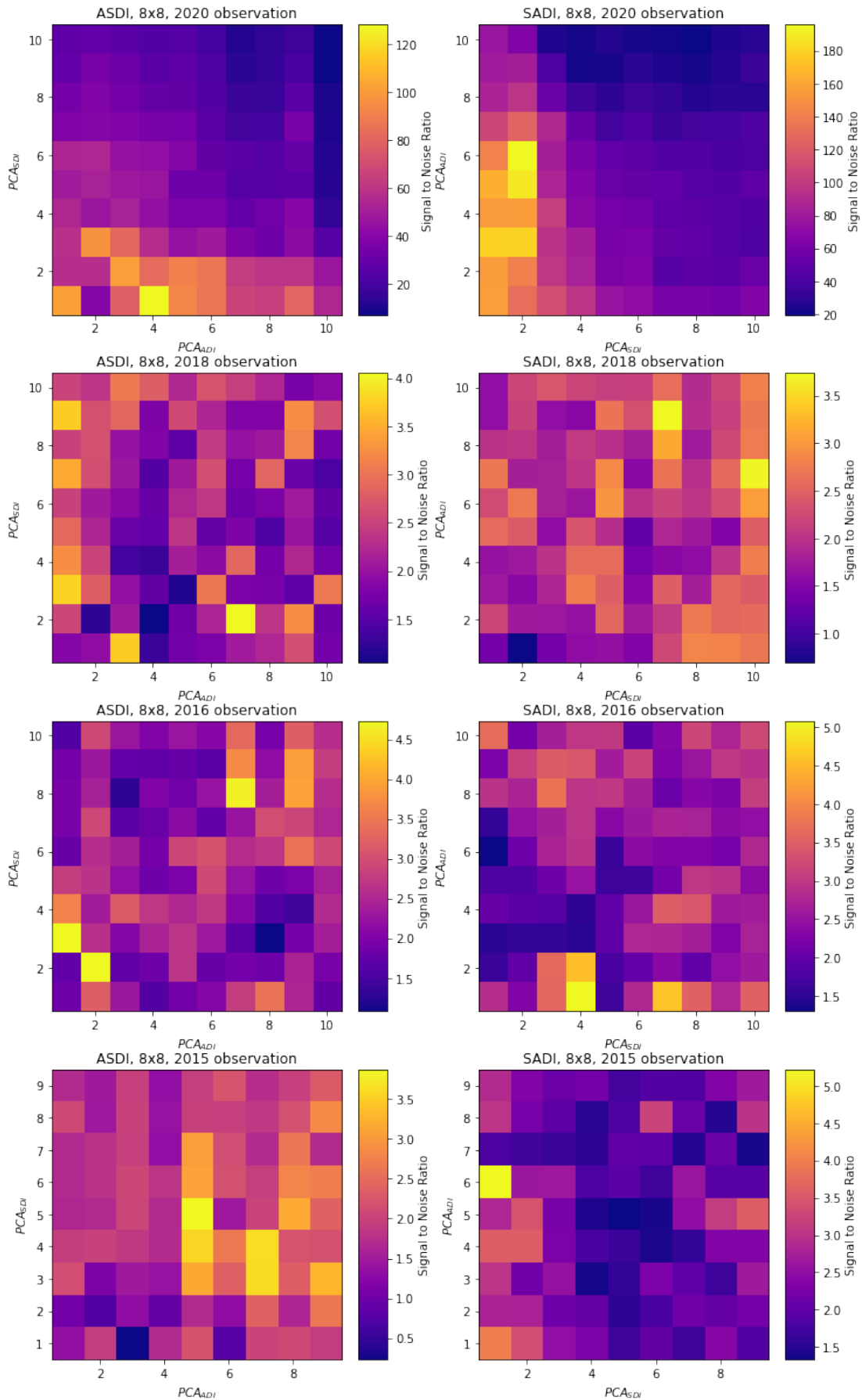


Figure 3.9: Heat Maps of maximum SNR for varied PCA components in the data reductions of Beta Pictoris b over four observations. Unlike 3.8, this figure has unique color bars.

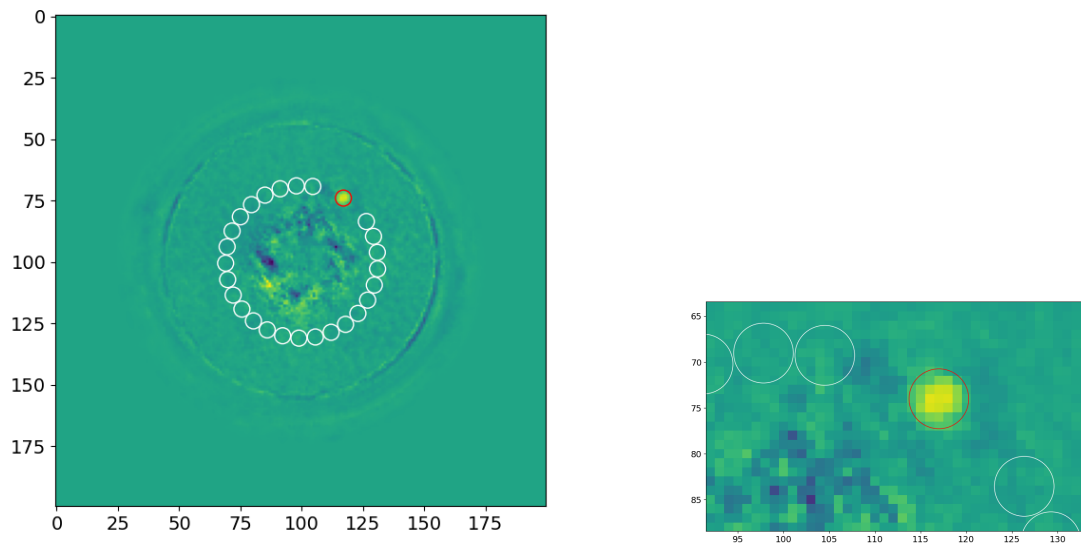


Figure 3.10: Areas used to calculate Signal to Noise Ratio (SNR). This example, from the 2015 Beta Pictoris observation, shows how the signal circle is captured (in the red circle) by the calculation algorithm and is compared to signal strength of the visually equivalent regions (in the white circles) around the star. The omissions of two would-be white circles adjacent to the red circle is due to the data reduction artifact that is generated during the ADI process.

the signal with respect to radii for all wavelengths is seen in Figure 3.11. We are again able to see a pattern like before: coronagraphic speckles around radius equal to zero, a planetary signal peak further out (for 2020, the peak at radius equal to approximately 40 [pixels]), and low-level oscillations extending to the edges of the plot that are believed to arise from background and instrument noise. We can focus in particular on the data reduction's creation of a suppressive artifact of signal around the signal center. The dips in signal that drop below the zero threshold are nonphysical, and the ones that do so before and after the signal peak maximum are a systematic effect or the *artifact* of the data reduction accomplished by PynPoint in this research. These can be more readily seen in Figure 3.12, which zooms in on the planet position area, showing the signal peak's distinct shape.

### 3.6 Modeling and mitigating the suppressive data reduction artifact

The scope of this research includes a brief foray into possible methods of removing the artifact from the reduced data. An approach that considers first principles and the steps undertaking within the data reduction itself was said to be excessively complex and is not considered within this thesis. After the completion of the data reduction and the size, shape, and locations of the artifact are deemed given, we looked into overlaying signal peak regions (on radial signal cuts, see Figure 3.7 for orientation) with simple cosine functions for multiple observations.

This research applied cosine functions to the 39 wavelengths' signal as functions of radii. This was done by locating the planetary signal peak, and then defining a range around it,

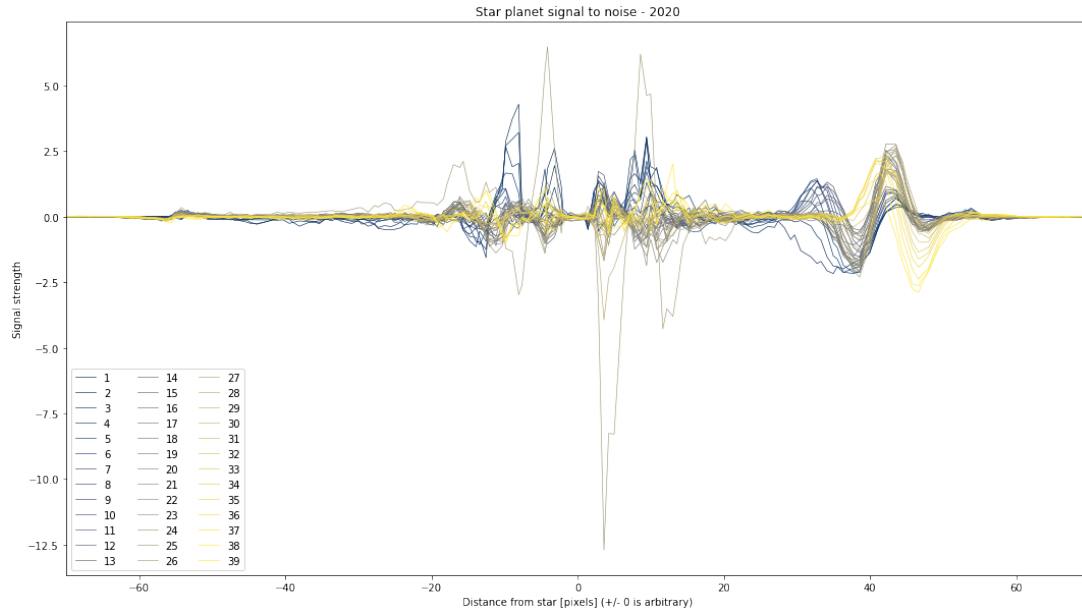


Figure 3.11: Signal plotted on radius (or distance) to the host star for all wavelength channels. From the left to the right of the plot: There is low-level background noise at large negative radii, intense coronagraphic speckle noise around zero, the planet signal around 40, and low-level background noise beyond the planet.

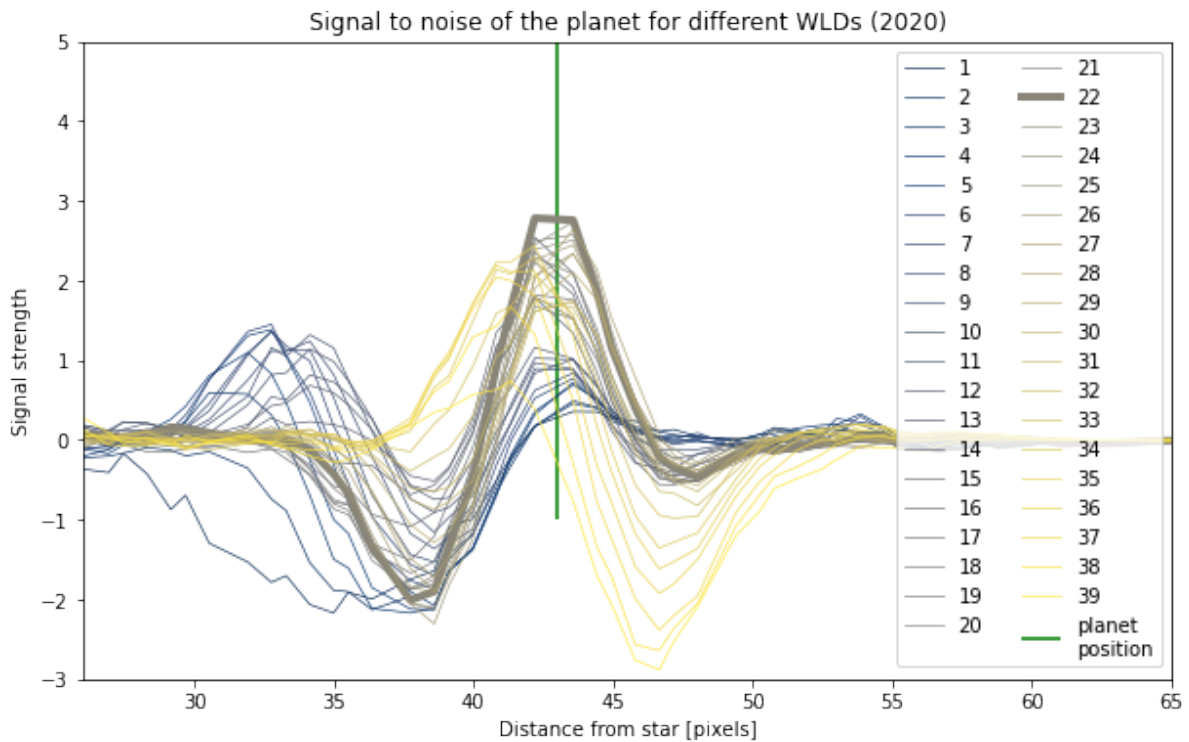


Figure 3.12: A zoomed in plot around the planet position signal peak from the previous figure. Notice the differences in the position of the peak planet signal as functions of radius for the 39 different wavelength channel detectors. From Fig. 3.11.

multiplying by a single period cosine function.

$$signal_{modified}(r_{min} < r_{peak} < r_{max}) = signal_{original}(r_{min} < r_{peak} < r_{max}) \cdot \cos(\theta) \quad (3.4)$$

Where  $r_{min}$  and  $r_{max}$  are some equal distance below and above the  $r_{peak}$  value (usually  $\sim 10$  pixel lengths), and  $\theta$  is bound between  $-2\pi$  and  $2\pi$  while spanning the radius range. This equation was applied in two ways. The first was simplest; the radial distance between the artifact's minimal trough and the signal's maximal peak was calculated. This distance was doubled to the left and right of the signal peak, which effectively isolated a range of radii for our consideration. This range starts at the inside edge and ends at the outside edge of the artifact, planet, and detection. The inside artifact suppression is in the first quarter of the range, the signal peak at one half the range, the outside artifact suppression is at three quarters the range, and the outside of the artifact is at the end of the range. The second application of the cosine function began in the same way as the first, but instead of using the maximal signal peak for all wavelengths, each wavelength's maximum was found, and then the cosine was applied in the same way to the several peak maxima locations.

The results are varied. The 2020 observation and the second application (for each wavelength maximum) were the most promising initially; this is seen in Figure 3.13. The Many

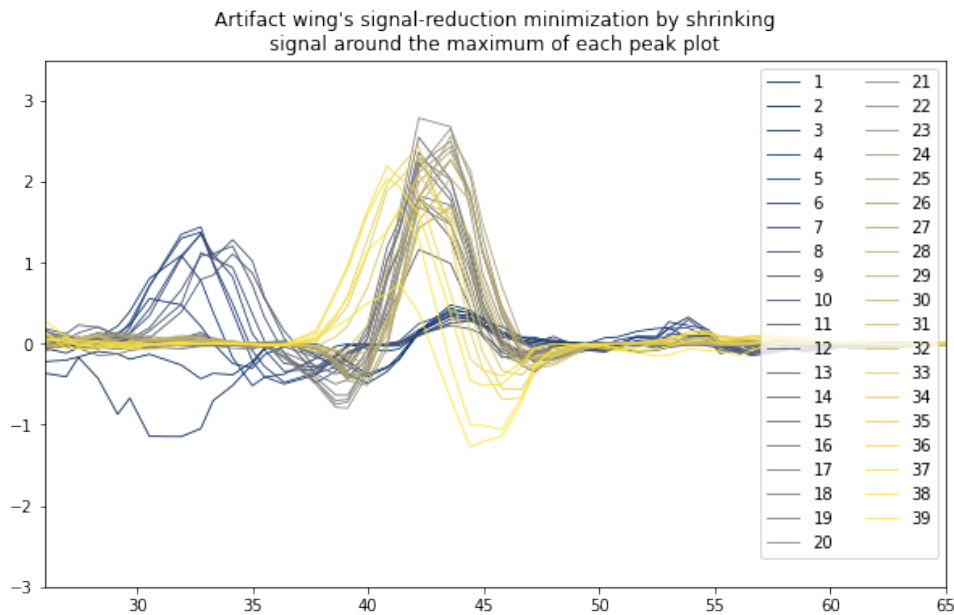


Figure 3.13: Results of mitigating the suppressive artifact with the first cosine application. It is natural to compare this plot with the one seen in Figure 3.12.

troughs dipping far below zero (often between -1 and -3) are pushed upward, creating a more normal distribution function (often between 0 and -1) between the planet and the background. This is one piece of evidence that this approach might be useful for exoplanet detection with direct imaging; however, it is far from a durable, robust, or even recommended approach given the immense lack of testing. If we pick unfavorable parameters, like the 2018 observation and the first application on the cosine function, then we see that the shifting of the original signal becomes partially deleted, instead of partially reshaped into a normal distribution (function). This is seen in 3.15.

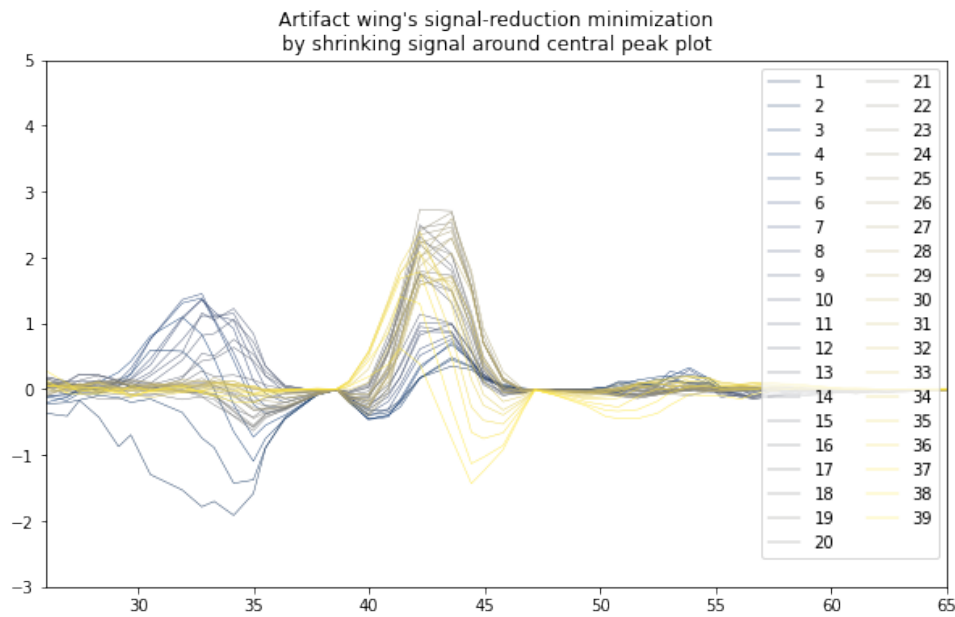


Figure 3.14: Results of mitigating the suppressive artifact with the second cosine application. We can see that this second application pinches all of the signals to two common values of zero, showing off it's fundamentally artificial original design. Comparisons with Figures 3.12 and 3.13 show how there can be a sizable variety of ways to negate the data reduction artifact's signal suppression.

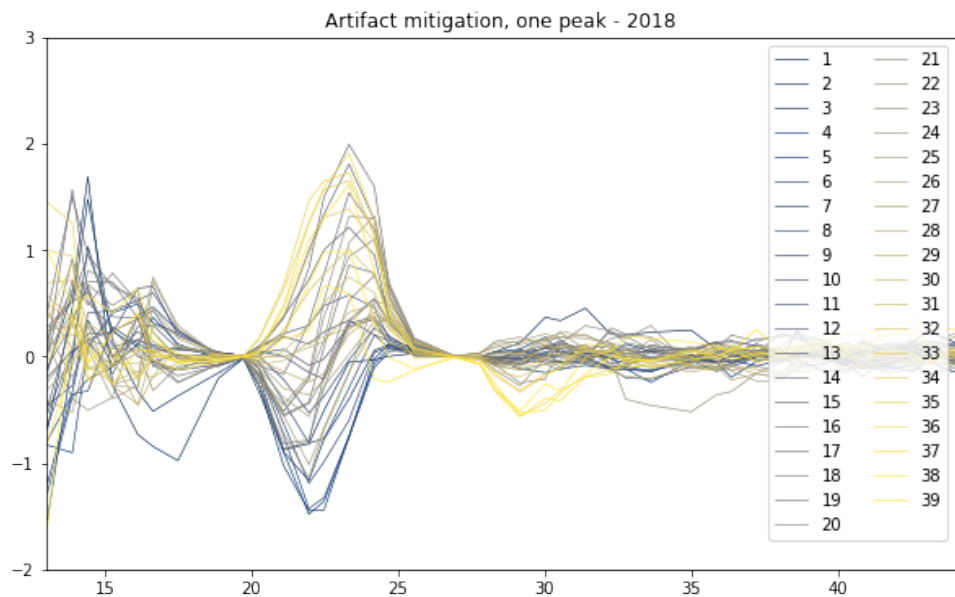


Figure 3.15: Inferior technique results of mitigating the suppressive artifact. The difference between plots like 3.14 and this one show a range in the quality of our mitigation results.

In summary, applying a cosine function over a range of angular separations around a planetary signal peak might be a worthwhile avenue of research. We have taken the first steps to analyze techniques that work on both a global peak maxima and on a set of wavelength dependent maxima. Results, for some situations, might be promising, but only with much more research will we be able to determine.

### 3.7 Curve fitting of signal peaks and error from literature position

In order to determine the accuracy of our calculated planet position with respect to different wavelength channels, we use the discrete data around a signal peak to make a PSF model of the exoplanet. The smaller the error associated with the terms in the PSF model, the higher the quality of the detection. This section shows the literature locations of the exoplanet, presents the Gaussian curve equation used for the PSF models, and then discusses the error bars in the models and regressions for them over the 39 wavelength channels.

From before, The 2015 planet position came from Lagrange et al. [2019]; later observations used Lagrange et al. [2020]. This research endeavors to capture where each wavelength channel's peak signal is in relation to all of the other wavelength channel peaks and the known (literature) planet position. The somewhat discrete and jagged local planet signal peak regions seen in Figure 3.4 are fitted to normal Gaussian curves using Python's Curve\_Fitting library and the equation,

$$f(x) = \frac{A}{\sqrt{2\pi}} \cdot e^{-\frac{1}{2} \cdot \frac{1}{B} \cdot (x-C)^2} - D \quad (3.5)$$

where  $x$  is  $r$ , the radius between the star (image center) and the planet. The constants  $A$ ,  $B$ ,  $C$ , &  $D$  are regressed by the fitting function and correspond to the amplitude, standard deviation, mean (as a horizontal/radial distance from zero), and (vertical) displacement from zero of a normal distribution. The first analysis is done on the parameter  $C$ , the mean. This value corresponds to the estimated peak location for a smooth function, given the discrete data regarding the peak. The variance of the mean ( $C$ ) also provides a basis for an error analysis when performing statistical regressions.

#### Error bars & regressions

How the data reduction creates an artifact at different locations is of keen interest to those intending to perform more exoplanetary detections by direct imaging. If we consider the data of 2016, we find that the planet is in greater alignment with its host star, and thus its signal is mixed in with the speckle noise in the former. If we consider the data of 2020, the planetary signal clearly stands apart from the star. This should and does indicate that signal peaks (for each wavelength) are less Gaussian, and their curve fitting has larger errors in the 2016 observation than in 2020. The error bars on the most probable planet location (the mean,  $C$ ) term are plotted horizontally on the location of their means in Figures 3.16, 3.18, 3.17, and 3.19; these, by definition, correspond to the location of the functions' maximum heights.

In Figure 3.16, some error bars in the 2020 observation are clearly visible on their peak maxima, while others are so small they are indistinguishable from the peak maxima on which they rest. It would be possible to see them if the line width of the peak curve was smaller,

but their lack of visibility here has been taken to mean that this model is well suited for the data. Standing in stark contrast to the 2020 observation, we see error bars in the 2016 Figure

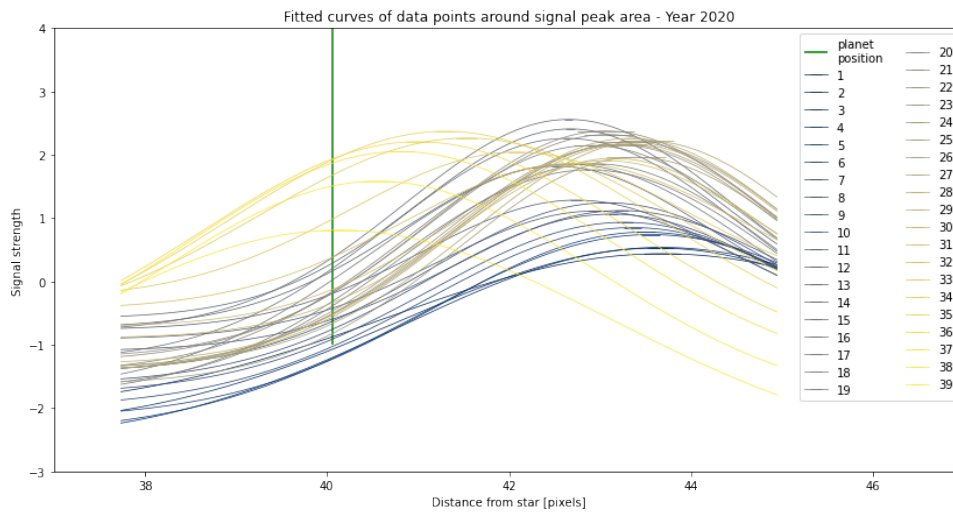


Figure 3.16: Results of smooth curve fitting model with error bars on each signal maxima of the signal peak data for the 2020 observation. Note: Some error bars are too small to be seen apart from their local peak maxima; the error bars are seen (vertically) in the Position difference plots beginning with Fig. 3.20 below

3.17 observation that exceeded the plot's entire frame. Not surprisingly, there seems to be a range in the star-planet separation where this model of planetary signal is accurate, and then another part where it is inaccurate. Determining this drop-off in accuracy with respect to angular separation would be a natural follow-up to the research done for this thesis.

Isolating the location of the peak heights (with their margins of error) and ignoring the variance and vertical displacement of the distributions allows us to more clearly see the trends, apparent movement, or "rolling" of the data reduction's artifact. An example of this is seen in Figure 3.20. Take note that is it the variance or error, which was plotted horizontally on the location of the signal peak maxima before, is plotted vertically on the wavelength index number axis here. No simple (linear or polynomial) function, consistent across observations, modeled the artifact's migration. Various linear and higher order polynomial fits were made on the models; some fit better than others, but a clear, consistent, and easily modeled regression has not been found in our research—see Figures 3.21 and 3.22.

More possible models from different regressions, and for different observation times are located in the appendix and seen in Figures A.4, A.2, A.1, and A.3. Any future efforts to pre-calculate mitigating factors for the artifact will have to be done with great care and undertaken with regard to the different contexts planets can be found.

The migration of the artifact in 2020 and 2015 can be modeled with a degree of predictability that is absent in the 2016 and 2018 observation. When the data points with error measurements that are at least one order of magnitude more than the collective average are given rather insignificant weight (or outright omitted), as is the case for the 11th wavelength channel in the 2018 observation, slightly more robust predictions can be drawn. Procedures for selecting curve fitted models with amplitudes significantly over a positive minimal value

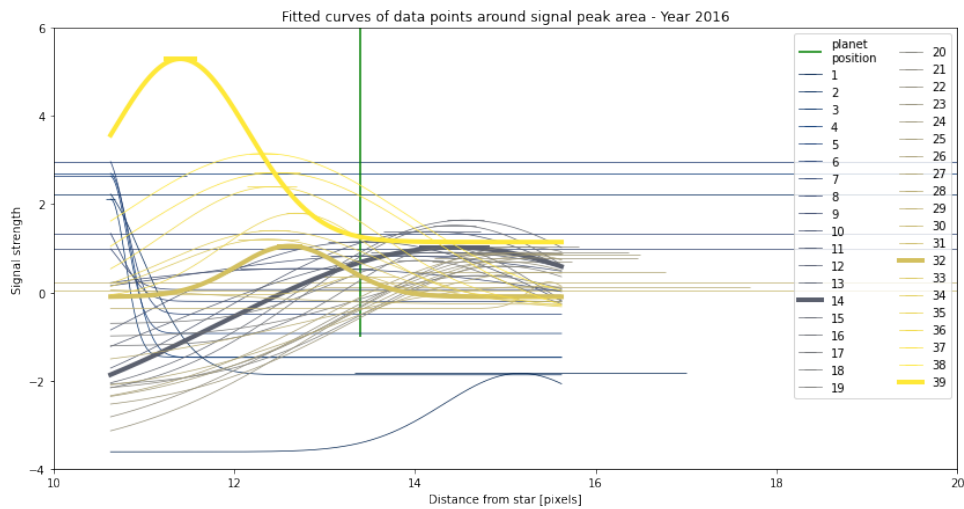


Figure 3.17: Results of smooth curve fitting model with error bars on each signal maxima of the signal peak data for the 2016 observation. Note: Many error bars are wider than the entire signal range used for the fitting

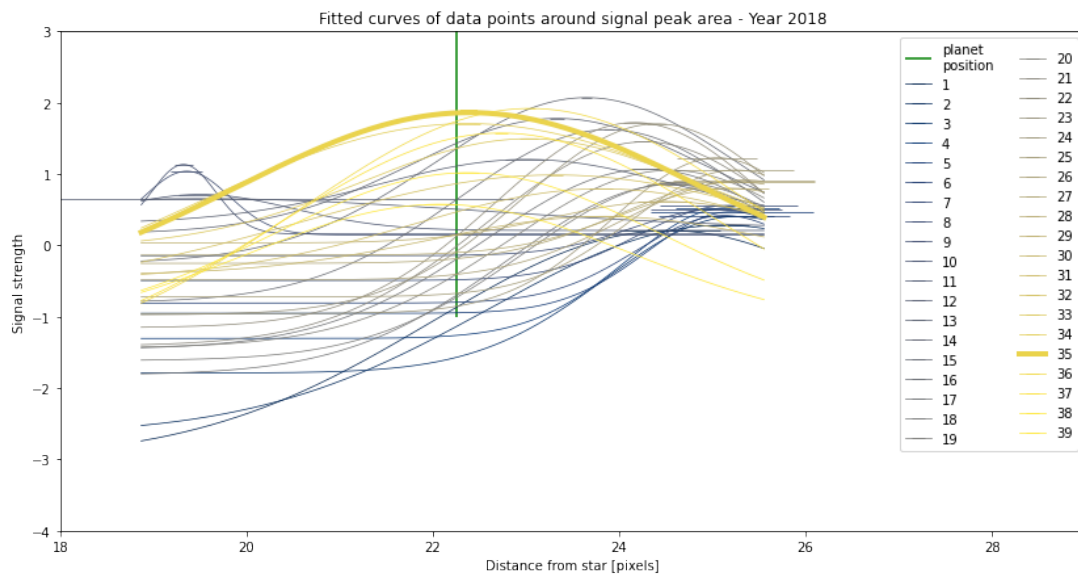


Figure 3.18: Results of smooth curve fitting model with error bars on each signal maxima of the signal peak data for the 2018 observation. Note: The horizontal bars on many peaks are somewhat longer compared to 3.16, which indicate larger uncertainties in the regression

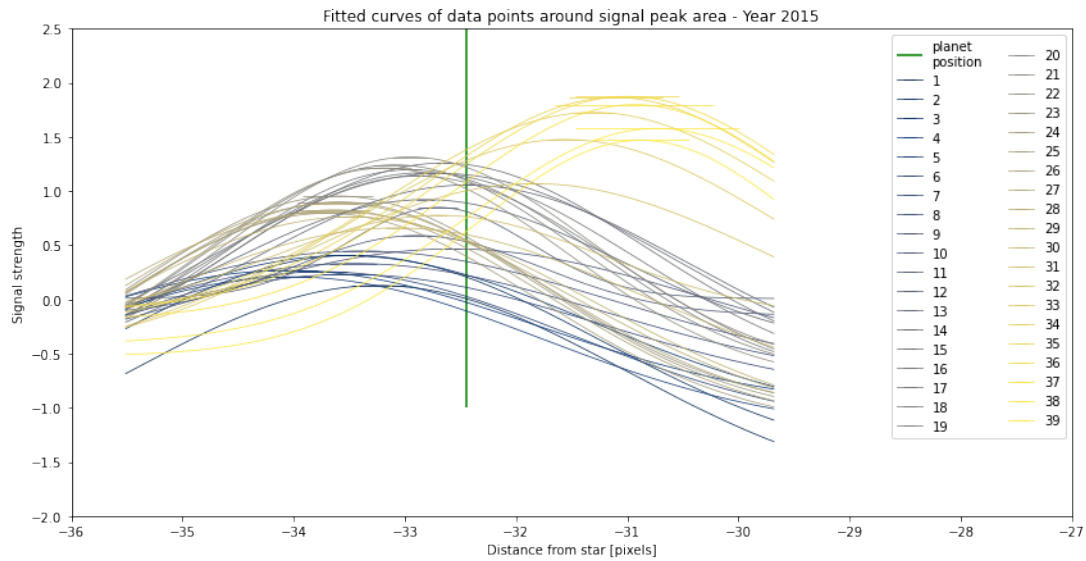


Figure 3.19: Results of smooth curve fitting model with error bars on each signal maxima of the signal peak data for the 2015 observation. Note: There is similarity between the 2015 and 2018 observations, like the similarity in their angular separations seen in Figure 3.2.

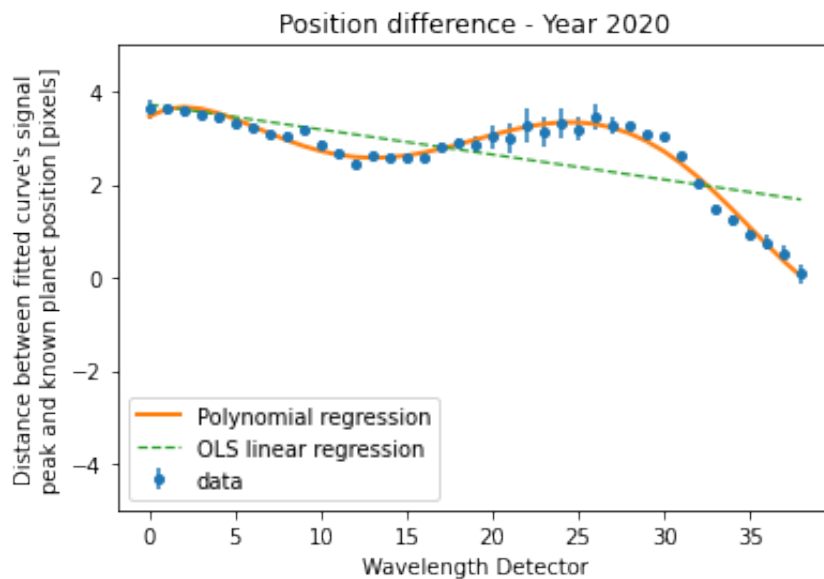


Figure 3.20: Difference and regressions between fitted smooth curve peak models with the literature value position of Beta Pic b for the 2020 observation. The blue data is seen with vertical error bars from the curve fitting parameter variances (the horizontal bars on peak maxima in the previous four figures); the solid orange line represents a 5th order polynomial OLS regression; and the broken green line represents a linear OLS regression. Note: The value differences are consistently positive between the planet position after the data reduction and the planet's literature position

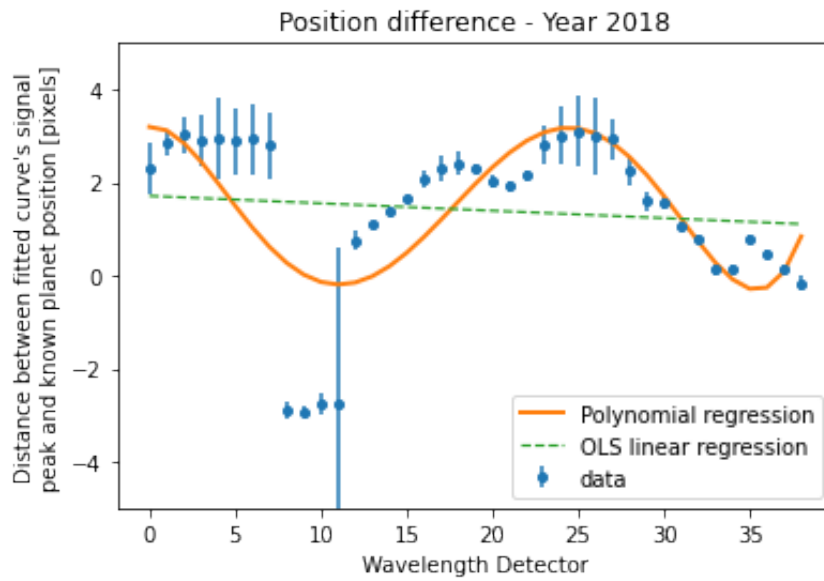


Figure 3.21: Difference and regressions between fitted smooth curve peak models with the literature value position of Beta Pic b for the 2018 observation. The blue data is seen with vertical error bars from the curve fitting parameter variances; the solid orange line represents a 5th order polynomial OLS regression; and the broken green line represents a linear OLS regression.

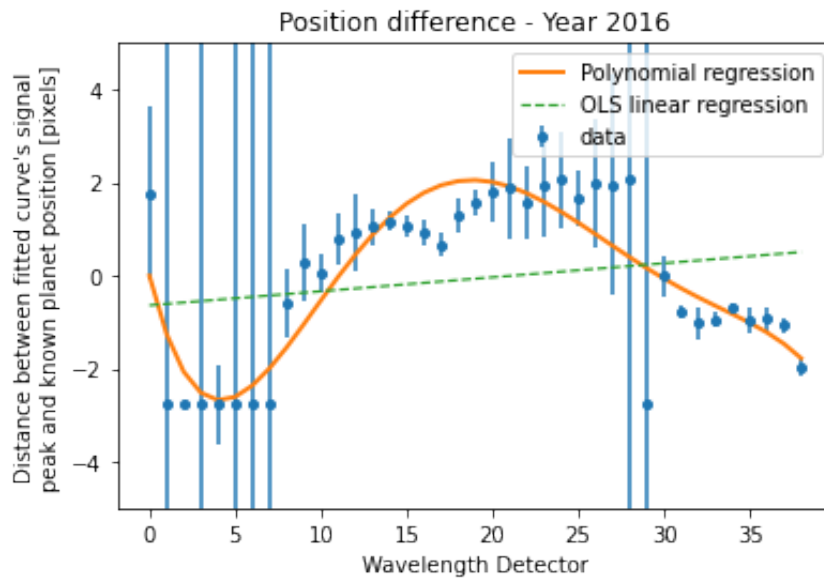


Figure 3.22: Difference between fitted smooth curve peak models with literature value position of Beta Pic b for the 2016 observation with regressions. The blue data is seen with vertical error bars from the curve fitting parameter variances; the solid orange line represents a 5th order polynomial OLS regression; and the broken green line represents the simple linear OLS regression.

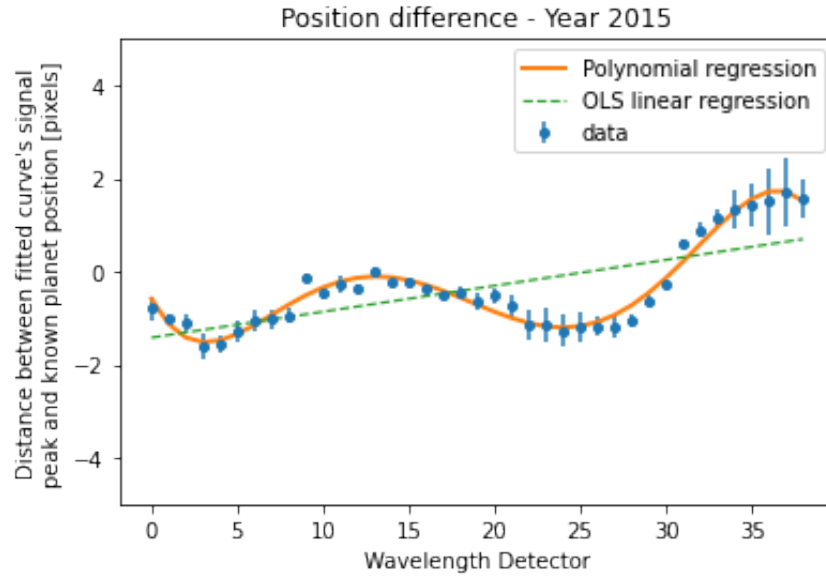


Figure 3.23: Difference between fitted smooth curve peak models with literature value position of Beta Pic b for the 2015 observation with regressions. The blue data is seen with vertical error bars from the curve fitting parameter variances; the solid orange line represents a 5th order polynomial OLS regression; and the broken green line represents the simple linear OLS regression.

( $\sim 3\%$  of an observation's maximum planet signal for any wavelength channel) and neglecting the remainder would also help to illuminate patterns in the trends of well-behaved data.

# Chapter 4

## Discussion

This discussion is organized into five parts: A discussion about observation *instruments*, and another about *targets*; a comparison between differential imaging *techniques*; a comparison between imaging at different angular *separations* (and times); and theoretical and practical methods of mitigating the suppressive data reduction *artifact*. The first part focuses on the combination of angular and spectral differential imaging and discusses optimal detections from such parameter bases. The second part illuminates how the best results come from the 2020 observation, and the rate at which the methods used in this research lose their applicability as the planet (nearly) aligns with us and its host star in 2016. The third part discusses the ability to track the planet position based on the location of the brightest signal and migrating data reduction artifact. In particular, we examine how the fitting of Gaussian curves to the signal peaks over all wavelength channels can be used to distinguish between the quality of planet position models. We also look at some of the challenges we face in the data and novel methods to possibly make more sophisticated models of their behavior.

### 4.1 Instrument considerations

The work of Christiaens et al. [2019] shows results analogous to ours for the planet, PDS 70 b, using the SINFONI (Eisenhauer et al. [2003], Bonnet et al. [2004]) instrument on the VLT. Using data from SPHERE's observations of Beta Pictoris b expands the scope of differential imaging applications. Moreover, the methodology was designed differently in this research as our aim was directed more towards signal enhancement and peak migration with respect to wavelength instead of their emphasizing of signal contrasts and software comparisons (a new algorithm vs. ANDROMEDA).

### 4.2 Target considerations

Our research gathered, analyzed, and modeled various aspects of observations made of Beta Pictoris. The plethora of other nearby stars are potential candidates for making exoplanetary detections with SPHERE; some particular objects of interest are seen in the conclusion (Table 5.1). Research done in Samland et al. [2017] used SPHERE's observations of 51 Eridani b; which yielded the first spectrophotometric measurements in the Y and K bands for the planet,

and evidence of a uniformly cloud-covered atmosphere. Beyond their routine data reductions of "background subtraction, flat fielding, bad pixel removal, centering, and spectral calibration," they used the ADI and then after the SDI method. Our research used spectral data, while theirs involved full spectral extraction, we both overlapped in using the PCA reduction approach [Amara and Quanz, 2012]; they compared their PCA results with two other spectral extraction reduction methods, namely TLOCI [Marois et al., 2014] and ANDROMEDA [Cantalloube et al., 2015].

### 4.3 Comparison of methods (ASDI & SADI)

The classic direct imaging data reduction method, ADI, was introduced well in Marois et al. [2006]. Much research has gone into other techniques since then; this includes SDI, ASDI, SADI, and CODI. This work has been state of the art as it has analyzed these techniques while using a both broad and deep range of PCAs.

The heat maps in Figures 3.8 and 3.9 provide invaluable insight into the usefulness of the optimization of PCA. The best results possible have been obtained with an SADI data reduction with  $PCA_{ADI} = 2$  and  $PCA_{SDI} = 6$ . Increasing the number of SDI components (3+) extremely quickly leads to a sharp drop in the SNR, another rather fast decline occurs when the number of ADI components increases (7+). Two much slower declines occur in the opposite directions, as the ADI and SDI PCA components move towards one.

The ASDI reduction technique also produces high signal-to-noise ratios, though they are less than the SADI technique. Perhaps the most interesting finding was the favoring of the ADI PCAs in this instance. Seemingly, which ever data reduction is performed first will naturally lead to ADI PCAs having the larger and more dominant position in the optimization of the SNR. This can suggest that the variables and degree of dimensionality in the ADI reduction are greater than in SDI. Here we found the best SNR obtained when  $PCA_{ADI} = 4$  and  $PCA_{SDI} = 1$ . The work of Christiaens et al. [2019] is in accord, as their optimum PCA combination is also a set of small, unequal whole numbers. The difference between their optimal numbers and ours is incomparable, due to the different instruments and targets used for observations.

The earlier detections in 2018, 2016, and 2015 might contain worthwhile and insightful discoveries. If they do, they will be uncovered during future investigations, as their relative planetary signal intensities compared to either of the 2020 data reductions has led their analysis to be postponed to beyond the submission of this work. The first approach for this future line of inquiry will involve a statistical comparison to a random distribution of SNRs that have no relationship to the PCAs that go into them. This is possible and would limit the application of our results to instances with significantly clear and high-quality detections, such as is seen in the 2020 observation.

The work on Kernel Phase Interferometry by Chaushev et al. [2022] uses SDI as a calibration method that hopes to achieve photon noise limited kernel phase observations by mitigating the residual systematic errors in the kernel phases using information available in adjacent wavelength bands. When large and sensitive enough telescopes are able to collect data, SDI will be able to detect chemical species from the planet. Other current research is also being done on reducing the data artifact and deblurring images using ASDI techniques [Flasseur

et al., 2022].

## 4.4 Comparison between times & angular separations

Research more recent than Marois et al. [2006], has shown significant improvements in the application of the ADI method [Vigan et al., 2015]; where sensitivities are up to a 50 % detection probability of an  $8M_{Jup}$  planet orbiting the star Sirius at a separation of  $1AU$  (and intuitively, a greater degree of certainty in the observation for larger planets and uncertainty for smaller planets).

The unique orientation of the Beta Pictoris system allows astronomers a great wealth of phenomena to investigate. The inclination of the system (see Beta Pictoris in Results section) allows for regular observations over different angular separations on the sky. We have seen that the angle approach zero, and the exoplanet and host star are nearly aligned in the 2016 observation. In contrast, we have also seen a wide berth between the star and planet, as most evident in the 2020 observation. The useful question to ask is, how insightful are the techniques we have developed (on the clearest and best observation) for the smaller exoplanet separation observations. We will continue the discussion assuming the simplest case: all observations were made under equal conditions (except for star-planet separation). However, it is important to note that there could be many more factors than just angular separation that can be scrutinized here; for example, different exposure times or atmospheric conditions made during the four analyzed observations could be contributing to the differences in the results as well.

The question is an issue with not a straight-forward answer. In analyzing the heat maps located in Figures 3.8 and 3.9 we find that the best that any data reduction can do to an intermediate observation truly pales in comparison to the results of the best observation. Numerically, the best SNR obtained was 195.8. Excluding the 2020 observation, the best SNR was 5.22. If we define a variable for the quality,  $Q$ , of an observation with respect to a reference (best) observation as,

$$Q_i = \text{Quality} = \frac{\text{Maximum SNR of the } i^{\text{th}} \text{ observation}}{\text{Maximum SNR of all observations}} \quad (4.1)$$

This difference implies that for our work,  $Q_i \leq 0.0266$ , or secondary observations have less than 3% of the sensitivity of the optimal observation (except for the trivial case of analyzing the reference quality).

One might be apt to think that all work should then go into determining the best time to make observations because they appear to be so much more fruitful in terms of SNR. This is likely a naive jumping to conclusions, as it can be very difficult to predict when to observe a system before observing it. This is especially true when one does not know if there is a planet before observing. The scope of this research limits its recommendations to: Determine the best combination of PCAs for ADI and SDI for one's dataset; not for observational planning and considerations.

Despite their lower SNR, the observations from 2015 and 2018 were very robust when it came to modeling their signal peak curves for the exoplanet Beta Pic b, and had standard

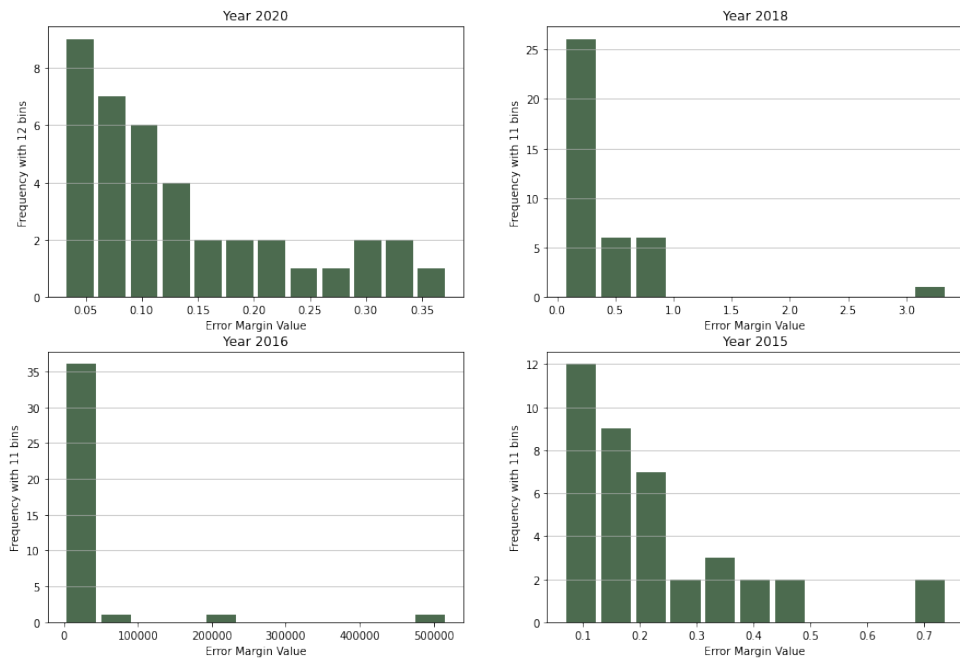


Figure 4.1: Histograms showing uncertainty of curve fitting mean standard deviation error margins. Note: Each plot (year) is on remarkably different Error Margin Values. The distribution on these four plots are compressed into a box plot in Figure 4.2.

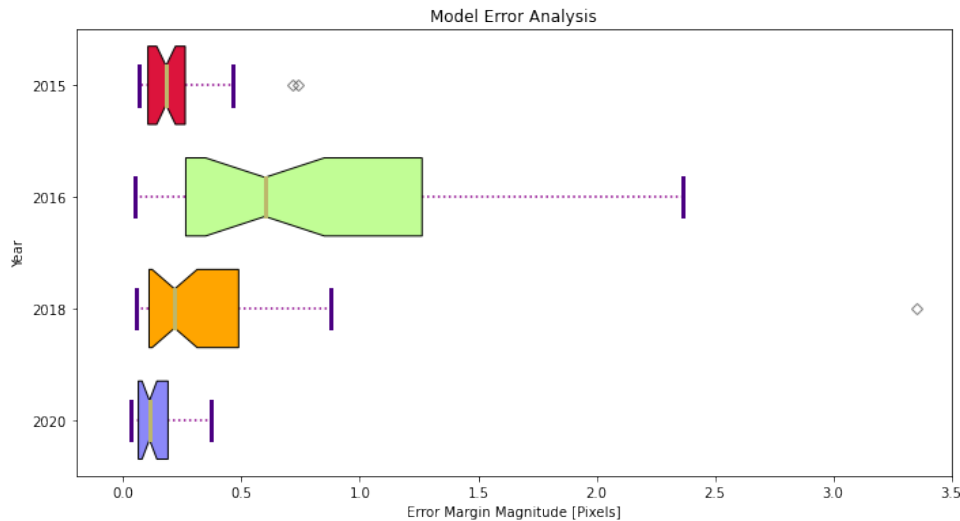


Figure 4.2: Box plots of curve fitting mean standard deviation error margins. The accuracy of how the data reduction calculates the planet signal’s mean value or location corresponds to the smallness of the box and whiskers. The bottom blue 2020 observation has the most accurate values, while the margin of error in the upper-middle green 2016 observation is so large outliers have been left outside the field of view shown in the plot (for ease of seeing more pertinent relationships in the data). More detailed distributions are independently plotted as histograms in 4.1

deviations or model margins of error not significantly larger than the ones for the 2020 observation. This is seen in Figures 4.1 and 4.2. Despite the significantly lower signal-to-noise ratios that can be obtained by the various data reduction PCA components in the 2015 and 2018 observations, it is sufficiently high for us to perform curve fitting with a degree of accuracy that is almost as good as when observing at the best time studied herein. The quality or accuracy of the curve fitting is seen visually in the box plot 4.2. Numerically, we find that the average degree of uncertainty increases from 0.14 pixels to 0.22 and 0.38 pixels when comparing the 2020 observation to 2015 and 2018 respectively; increases in uncertainty by factors of 1.6 and 2.7. The 2016 observation is omitted from this discussion because all numbers indicate the planet is completely indistinguishable from the speckle noise that was observed during this night.

## 4.5 Artifact reduction considerations

One of the attempts of this work has been preliminary endeavors to reduce the large negative signal dips that are common around processed images. This is an active area of research. One month before the deadline of this thesis, Samland et al. [2022] published an open-source new data-reduction pipeline for spectral data cube reconstruction from raw SPHERE Integral-Field Spectrograph data. It touts the improvement in sensitivity as being on the median 80% and 30% better than previously analyzed 2015 & 2017 data on a different stellar system (51 Eri b).

From a purely speculative beginning, our mathematical manipulations were made to the data in order to see if there were simple and arbitrary methods that could be used to mitigate the artifact. This would mean elevating the signal wells next to the central peak made by the artifact during data reduction; effectively reshaping the (signal) peak to more of a Gaussian function instead of a Bessel function.

The first idea tested was to find the local maximum of a known planetary signal peak, and then define a range around it, which was then multiplied by a single period cosine function on using the signal peak as the reference zero mark. See the equation in 3.4. The results can be seen in Figure 3.13. This shows that a more Gaussian curve can be obtained. However, this does by no means indicate we have created a superior reduction method; it solely indicates there is a whole field of research that is open down this line of thinking.

The unique nature of the signal location in the highest wavelength channels (yellow lines) is their peaks and troughs are shifted radially inwards. The original cosine multiplication around the highest peak has the effect of reducing these high wavelength detector's radially-closer peaks, and doing relatively little to their slightly earlier troughs (which are closer to the highest peak's location than other troughs). Figure 3.14 shows another method of artifact reductions suppression that is no longer applied using the location of the peak signal of all wavelengths, but rather using the peak signal of each wavelength. This allows the cosine function to start and stop over small ranges of each wavelength's radius, depending on where that peak radius is. We can see that the artifact's suppressive reduction is mitigated more efficiently in this second case. Also, the peak of all wavelengths is broadened by the preservation of the highest wavelengths' peaks being unchanged. More investigations are necessary to indicate whether this has a beneficial bearing on exoplanetary detection and characterization or not.

Issues with this method of artifact signal suppression compensation arise with signals that are highly suppressed (to the point of being deeply negative) and having no relative augmentation or isolation of a peak anywhere around it. It is likely that signal emitted by the planet will approach zero at certain wavelengths, but negative signal is nonphysical and comes from human or systematic error; in this case, they are errors introduced by the data reduction methods. An example of this error is seen in Figure 4.3 where the artifact deeply suppresses signal, but does not show any significant locations of actual signal that the planet might be located at. Methods to create signal in or around the wells of the suppressive artifact were

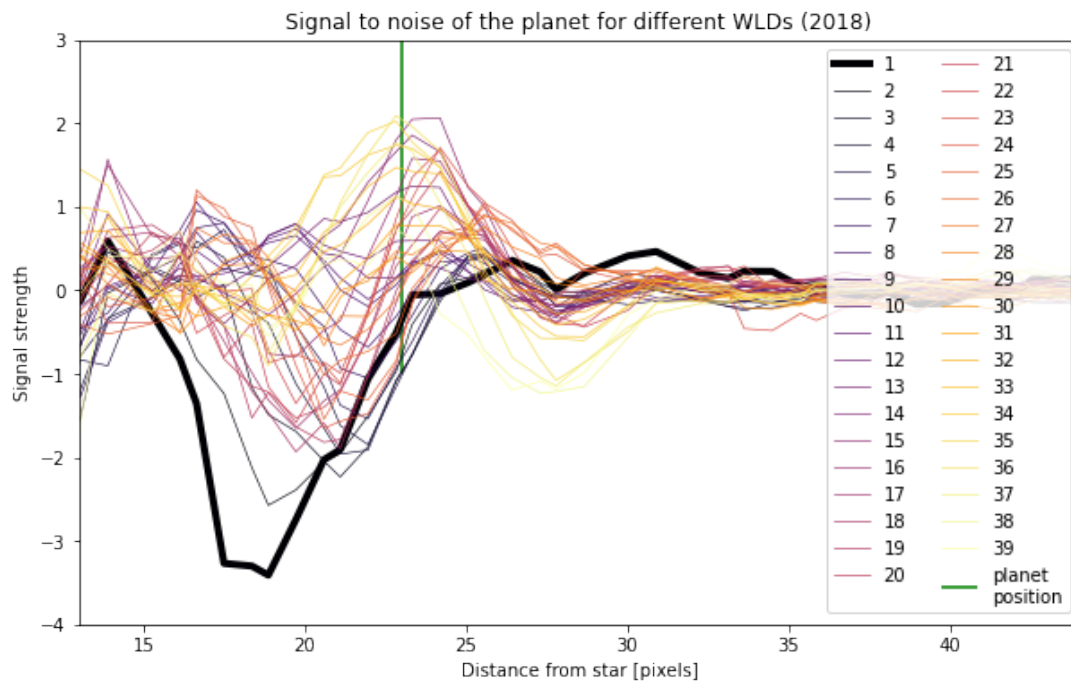


Figure 4.3: An example of data reduction method complexities. Here a peak is seen in many of the higher wavelengths at approximately 23 pixels from the host star. The thick black line shows the result of data reduction methods used for the first wavelength detector (shortest wavelengths). Though many data manipulation techniques could be used in this situation, all were deemed too unrealistic and or irrelevant to the scope of this thesis to pursue in great depth.

considered, but their implementation and model optimizing was deemed beyond the scope of this research.

There was a surprising variety and complexity in the movement of the suppressive artifact between different wavelengths and observation times. One of the simplest solutions to modeling this diversity of results was to make regressions with very high order polynomials. We attempted to accurately fit the 2018 year's observation in this way. The 6th and 9th order regressions were insignificantly better than the 5th order, see the appendix A.1; beyond 9th order the end behavior of the regression caused strong diverge from quality and have been omitted.

## Artifact reduction alternative methods

The research done in this project used an overlaying cosine function to discover if mitigation could be possible in attempts to restructure the planet's signal into a standard PSF. A second method has been considered and will be implemented if time permits; this will use a subtracting parabola function. This method would be based on modeling the wells of the artifact as two unique parabolas with a domain that is centered on the minimal signal point, see Figure 4.4. Optimizing this avenue of research will determine if it is best to isolate the space around the

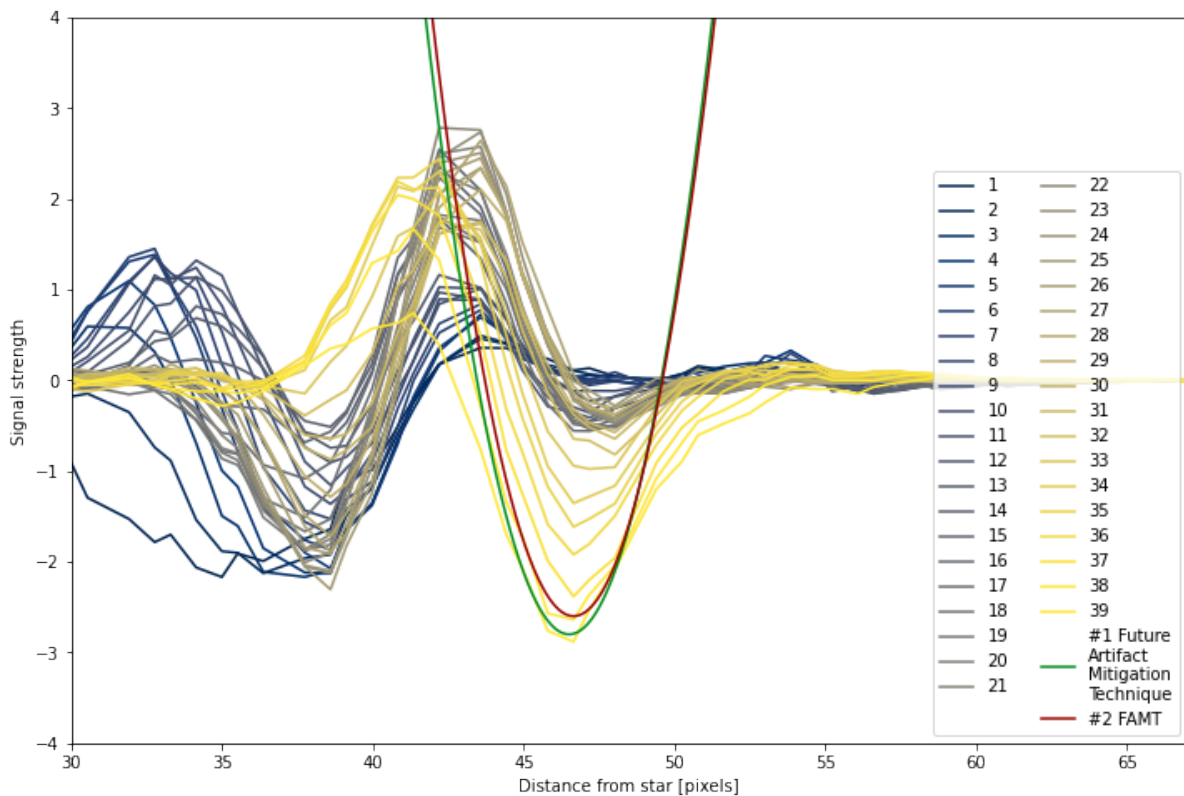


Figure 4.4: Future research into optimizing the signal profile (to resemble a normal PSF) might be accomplished with signal well modeled subtractions. Here, the red parabolas indicate how two different wavelength ranges near their minima can be modeled. These models can then be subtracted from the signal data. Optimal ranges and other parameters will be calculated in future investigations.

minimum, which the model is derived from, by using the distance to the peak height, to the first positive signal value on the stellar side, the planet side, or a combination of both.

# Chapter 5

## Conclusions

This chapter is structured by beginning with a summary of the work done, and then ending an outlook from the work, and parting thoughts. The outlook has the more narrow future perspectives of where this line of research can go, as well as the broadest goals of many others on the future of exoplanet science for the next decade or two.

### 5.1 Thesis Summary

This thesis has provided the author with an invaluable opportunity to learn about professional research in general and direct imaging of exoplanets in particular. Our results have drawn upon detailed analysis of the Beta Pictoris system.

The time dedicated to this research has used the data from the SPHERE instrument at ESO's VLT. The reduction of the data was accomplished with ESO Reflex and PynPoint, and took the form of Angular Differential Imaging and Spectral Differential Imaging. Four observations were studied in detail, one with large separation, one nearly in occultation, and two more intermediate ones (but on opposite sides of the host star). We used Principal Component Analysis in the data reduction and found their optimal combinations in different reductions for an observation of the Beta Pictoris system. We saw that the brightest peak in SPHERE's sensitivity range occurs during the 2020 observation, with a maximal PCA that has an SNR 7.5 times greater than that of the minimal PCA. This finding was supported with heat maps of all the observations showing maximal SNR as functions of PCA combinations.

The methods for calculating SNR were discussed and further avenues of research were considered in possibly improving the approach to their calculation. We investigated the small difference between the brightest planet signal with the calculated literature value for planet position. This literature value was compared to the signal maxima of angular and radial profile cuts.

Preliminary efforts were made to mitigate the suppressive artifact's effect during the data reduction. This is a wide open field of research, and our findings are only potential ideas that can be robustly researched and tested in the future. We have found that one model (cosine function overlay) applied in two different ways to different observations will have a varied, but often positive, influence on mitigating the artifact. We discussed another model as a parabolic

bowl to use for mitigation, but this was beyond the scope of this thesis's research.

Highly continuous models were made of the (semi) discrete data of the planetary peak signal profile cuts. These were then used to track the movement of the data reduction artifact. The movement was plotted for various observations; none could be modeled with a simple linear regression, but some were fitted well with a low-order polynomial, while others would require more advanced fitting or regression methods.

## 5.2 Outlook

There are plans for the future, and *this* and the research of *others* will continue to expand our body of astronomical knowledge.

### Future investigations – this research

In this work, there are several directions of interest that are worth pursuing in future time.

Beta Pictoris is a useful system to analyze, as it has two known exoplanets: one that has great visibility from the data analyzed, and another that is mixed in with the speckle noise from its host star. The myriad of other systems are well worth investigating, and with the knowledge of what PCAs are useful in detecting Beta Pictoris b, we have a starting point to base such future searches. Furthermore, doing PCA on other targets would expand the statistics beyond optimal detections based on orbital position, and into the realm of optimal detections around the particular types or sizes of exoplanets and host stars.

One other particularly promising target is 51 Eri b. Though it was not thoroughly discussed in this thesis, it was a pillar of the foundational work that went into this project Kiefer et al. [2021]. Continued work on this project would include an in-depth analysis of it. In the long run, well after other improvements in instrumentation and technology occur, the opportunity to have sensitivities which could detect large satellites or moons around exoplanets may be directly imaged. Pérez et al. [2019] has shown that there is little opacity from small ( $\leq 1mm$ ) dust grain content in the region of 51 Eri b's orbit; suggesting that grain growth has occurred quickly and that "moonetesimals" of  $\geq 1m$  sizes have very possibly already developed in this (and other) young stellar systems. Still other systems of interest are tabulated in 5.1

Various data reductions result in unusual images. For example, in Figure 5.1, we find a large black (negative) signal in between two strong positive signals of our exoplanet. Intuition might suggest to us that this is a planet-moon system where each has comparable masses and there is a substantial gap between them, but this has been deemed highly unlikely. Assuming then that this is one planet or a "one planet system" (a planet with normal small and close moons), there are several approaches that research can take to determine an optimal signal for this kind of data reduction.

The first approach is if the model of an upside-down bell-shaped curve passes a goodness of fit test for a wavelength channel, then that part of the data would be omitted, or inverted to a normal bell-shaped curve. The second approach would be to find where is the point of greatest increase, the derivative of the function is maximized, or the second derivative is zero, and use there as a new location model of the planet. These approaches as well as others are topics for future research.

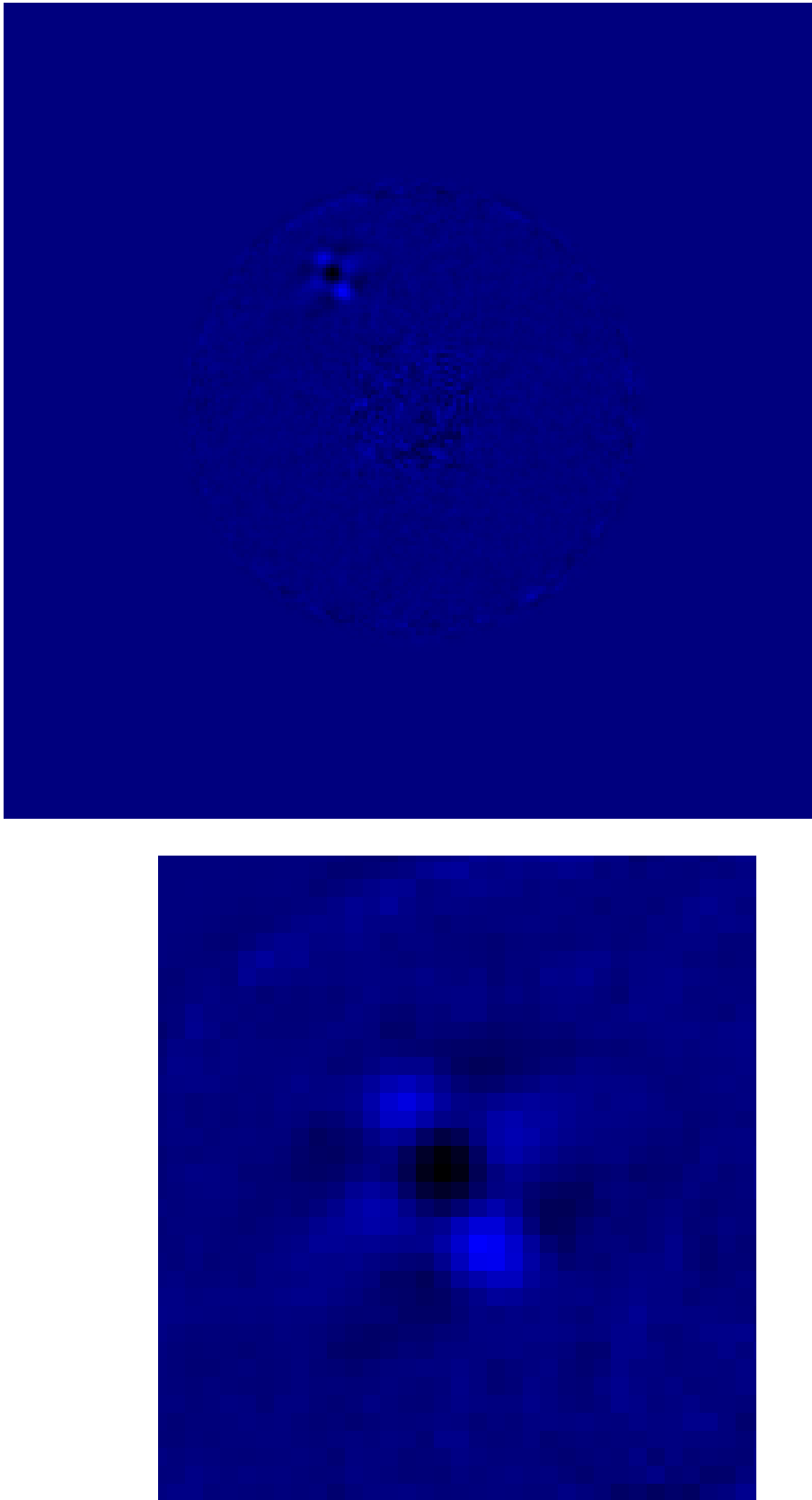


Figure 5.1: Data reduced direct image of Beta Pictoris. The opposite of a normal detection is manifest, as the planet is expected to create signal (white) instead of consuming it (black), but it appears to be consuming it in this reduced image

Targets of interest			
Beta Pic	HIP 65426	PDS 70	HD 10180
55 Cancri	HD 141569A	HD 33632	Gliese 1252
HD 8799	nu And	Kepler 16	Gliese 876
51 Eri	HD 33636	HD 40307	Eps Eri

Table 5.1: Potential Targets of research. Though only the first target listed (Beta Pictoris) was investigated, the applicability of our research might extend to a range of exoplanetary systems that can be discovered with additional time.

Not surprisingly, there seems to be a range in the star-planet separation where this model of planetary signal is accurate, and then another part where it is inaccurate. Determining this drop-off in accuracy with respect to angular separation would be a natural follow-up to the research done for this thesis.

## Future investigations – aggregate astronomical research

In going beyond the narrow confines of the work accomplished in this thesis, we have recognized some overarching patterns in astronomical research. Some of the great leaps and bounds that come in the field of astronomy occur with the advent of a new telescope. Either one that is sensitive to a new wavelength range of light or one that is larger than any of its predecessors. ESA is one of the pioneers in this field and have shown their commitment to studying the science of exoplanets with previous and future missions. A timeline is available for viewing in Figure 5.2

This timeline has led some to anticipate the discovery of tens of thousands of exoplanets from multiple different detection methods [Christiansen, 2022]. Consider the detections methods introduced in the beginning of this thesis (section 1.3): More innovative solutions are needed for Direct Imaging to make vastly more detections, but the continued success of the transit method, and the rise of the gravitational microlensing method will lead within the field of exoplanetary detections.

### Detection via Direct Imaging

Though none have been designed, built, and launched into space, yet one promising area for future exoplanet detections is with the use of star shades (or external occulters). This type of instrument has been wonderfully described in Flamary and Aime [2014], Janson et al. [2021], and Glassman et al. [2009]. The latter [Glassman et al., 2009] contains insightful figures (i.e., 5.3) and invaluable comparisons for design trade-offs that will change the sensitivity to various planetary parameters. One key parameter that will have to be decided on during the design process will weigh the two important goals of large stellar light suppression and small inner working angle viewing. A generous fiscal budget would allow for the development of

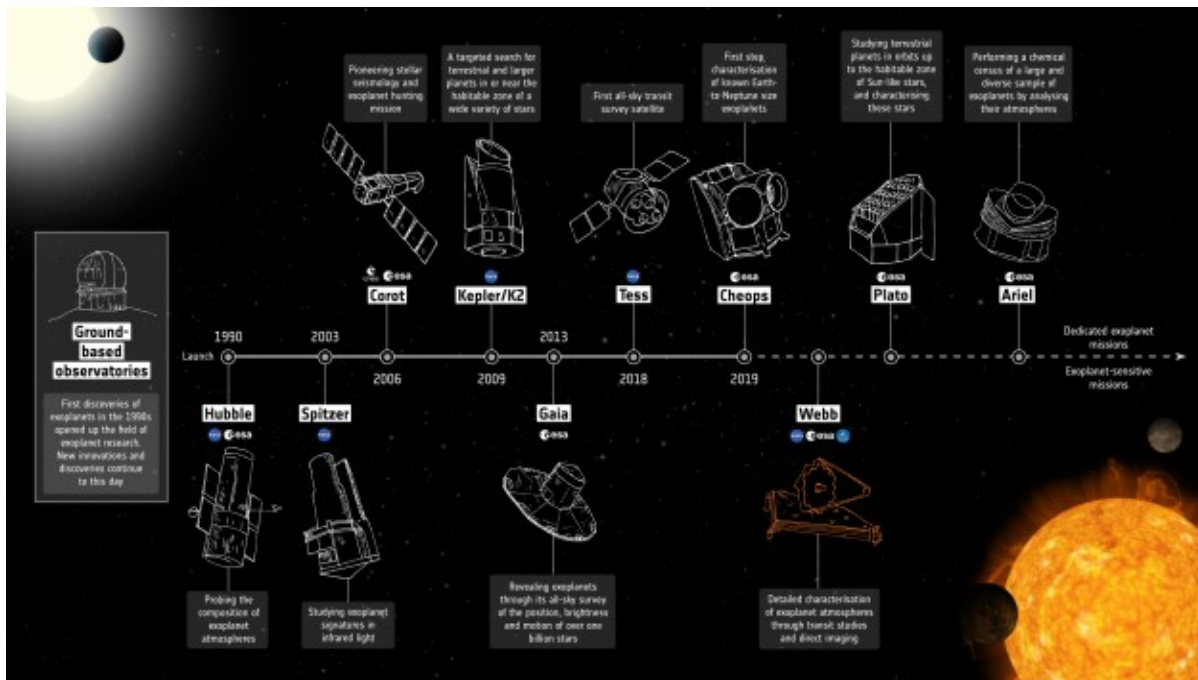


Figure 5.2: ESA Mission Timeline. The recent and upcoming space missions are shown on a timeline. A more up-to-date figure would show a solid line between Cheops and Webb, as the latter was launch at the end of 2021. Currently, Plato and Ariel are planned for launch in 2026 and 2029 respectively. Figure Credit: esa [2020]

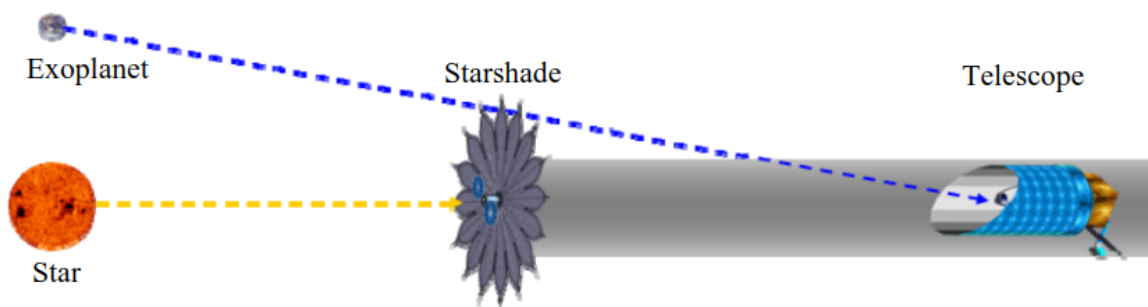


Figure 5.3: A diagram of a star shade. The (unlabeled) details of the figure (i.e., telescope diameter, starshade diameter, telescope-starshade separation, planet-star separation or "inner working angle", wavelength sensitivity range, etc.) will determine what kind of planets will be detectable by the system. Figure Credit: Glassman et al. [2009]

a large star shade with sufficient propellant (or possibly solar sails) to perform operations at far distances, but after sufficient design limits are imposed, as a star shade-telescope system improves either its light suppression or its inner working angle, the other's capabilities worsen. The debut of a scientifically valuable star shade will not be soon, but research is going into connecting one to any of the ACCESS, NWO, JWST, and ATLAST missions [Glassman et al., 2009].

### Detection via Radial Velocity

Future investigations in the field of radial velocity measurements will also push the frontiers of knowledge. Because the radial velocity method is most effective in detecting large mass and small orbit exoplanets, improvements in this technique will lead to the detection of ever smaller and ever more separate exoplanets. Figure 5.4 shows the detection limit (line) and distribution of known and predicted exoplanets for the HARPS, ESPRESSO, and CODEX instruments. The highlighted box at the bottom of each plot shows the area of would-be planets with characteristics (separation, which suggests temperature and mass) similar to that of earth. Though the ESPRESSO instrument has been predicted to approach the mass and separation of earth-like exoplanets, it is believed that only after the much larger ETL and CODEX (or similar spectrograph working with the ELT) comes online will we be able to probe into the parameter space that allows for the detection of earth-like planets.

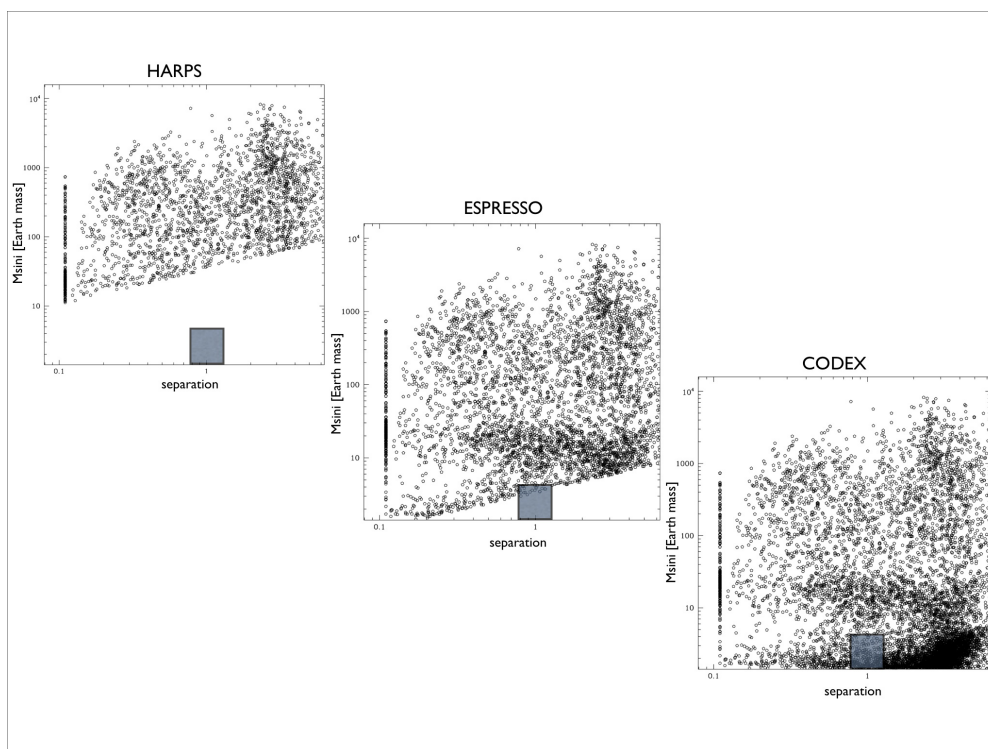


Figure 5.4: Simulated planet population of what is expected to be detected by radial velocity. Plots are after application of observational limits with the spectrographs HARPS/3.6 m (precision of 1 m/s) in the left panel, ESPRESSO/VLT (precision of 10 cm/s) in the middle panel, and CODEX/E-ELT (precision of 1 cm/s) in the right panel. Figure Credit: [Haehnelt and Pasquini, 2010]

## Detection via Transits

**Transiting Exoplanet Survey Satellite – TESS** The Transiting Exoplanet Survey Satellite (TESS) mission has followed on the success of the Kepler and K-2 missions. It also uses the transit method of detection to find new exoplanets; but instead of looking at a small sector of the sky for years at a time and gathering data on comparatively distant exoplanets, TESS is observing the entire sky for nearby exoplanets. This immensely greater degree of breadth does some with a loss of depth (or observing distance range) as planets not in Kepler's line of sight that orbit around smaller stars with distances that Kepler could see at its limits will not be given sufficient integration time for TESS to make conclusive detections [Adkins, 2016].

TESS launched in April 2018, had first light in August 2018, and concluded its primary mission in July 2020. From then until now, it has been performing its first extended mission, which was scheduled to end around the beginning of this autumn academic semester. Plans of observations are publicly available at Guerrero [2022]. This is the current mission to look for exciting press releases about, but there are even better ones in the works.

**PLANetary Transits and Oscillations of stars – PLATO** The PLANetary Transits and Oscillations of stars (PLATO) mission is a space telescope in development by the European Space Agency (ESA). It has been designed and optimized to detect and characterize telluric exoplanets orbiting solar-type stars. Mission planning has emphasized targeting planets residing in their host star's habitable zone. While Kepler was a forerunner of space-based exoplanetary detection, and TESS is the all-sky surveyor for such, the PLATO instrument will be able to characterize exoplanets while its targeting resembles both previous instruments. PLATO will accomplish this with precise, long-term, and continuous photometric monitoring of many bright stars. The light curves obtained are predicted to detect many planetary transits, which will yield planetary radii [Team and Aerts], [the, 2017]. Many of the key contributors of this project are from our very own institute. And for the past 8 years approximately there has even been a simulator available on the IvS website (<http://ivs-kuleuven.github.io/PlatoSim3/>) that you may use to generate predictions of what PLATO will find.

## Detection via Astrometry

The work done by Perryman et al. [2014] indicates that the final data release of GAIA will have ample information on astrometry. It is predicted to be sensitive enough to find classical Jupiter-like planets. This will be useful for comparisons of the other "hot-Jupiters" that have been easier to find with other detection techniques. Though its release date is not predicted on the ESA website, there is information currently stating that Gaia data release 4 will be based on 5.5 years of data, consist of An exoplanet list (among other things), and that pending mission extension approvals, more releases will take place Agency [2022].

## Detection via Gravitational Microlensing

Gravitational Microlensing is expected to provide a wealth of planetary detections in a range that is far from the current most-popular practices. Figure 5.6 shows the sensitivity range of the upcoming Nancy Grace Roman Space Telescope (formerly WFIRST); detecting planets

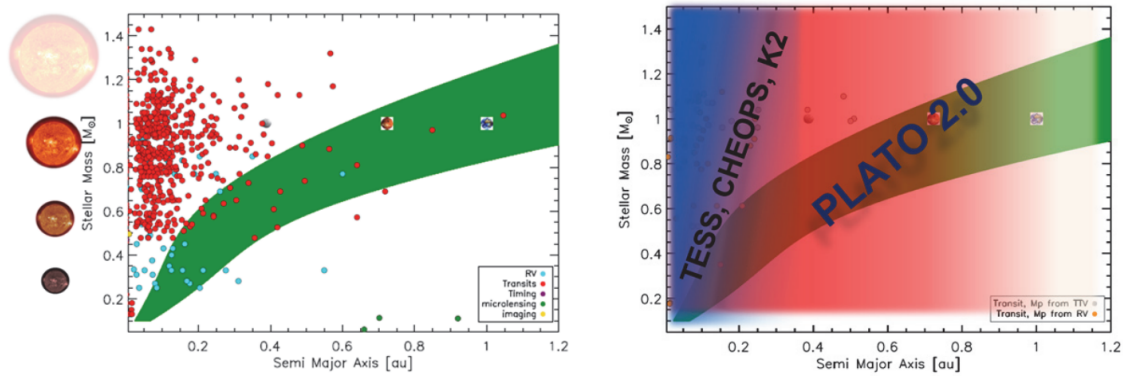


Figure 5.5: PLATO’s designed sensitivity range. The left plot shows the left plot shows known (as of 2016) exoplanets and the habitable zone of semi major axes, given a stellar mass. There have already been exoplanets detected in habitable zones around other stars, but in comparison to the number of hot and small semi major axis planets, there are few known in habitable zones. The right figure shows the parameter space able to be investigated by PLATO, and how it is mostly distinct, but partially overlaps other space missions (i.e. TESS and K2). Figure Credit: the [2017]

with large semi-major axis and especially those with small mass will shed much light on worlds that have been outside of Kepler’s observational capability.

### Characterization: Going beyond detection

Curiosity leads one to ask, "what is it?" after learning "yes" to the question, "does it exist?" So exoplanetary characterization naturally falls on the heels of detection. Keriedburg describes three methods of exoplanetary characterization of atmospheres in Kreidberg [2018]: transmission spectroscopy, emission and reflection spectroscopy, and full-orbit phase curve observations. Transmission spectroscopy is listed and discussed first because of its widespread popularity in the field. An explanatory diagram is shown in Figure 5.7.

The method of Spectral Differential Imaging (SDI) investigated in this research will continue to be useful in this and other applications. It is capable of improving planetary signal in post-process data reduction techniques; which, in the best-case scenario, means a signal below a detection threshold is pushed up to detection because of SDI. So far, this method has been paired with low-resolution detectors which might be able to detect broadband absorption curves (for example water or carbon dioxide atmospheres). Future observations may have higher resolution SDI, and the line spectra of species in the atmospheres or on the surfaces of planets might be characterized in this way.

## 5.3 Ending thoughts

This is the beginning, as there is much more work to do on the many aspects of this project that were considered, but not pursued. Time is of greatest importance as it has allowed for the invaluable understanding gained from this thesis and also limited the scope of the research. It is with gratitude that I end this thesis.

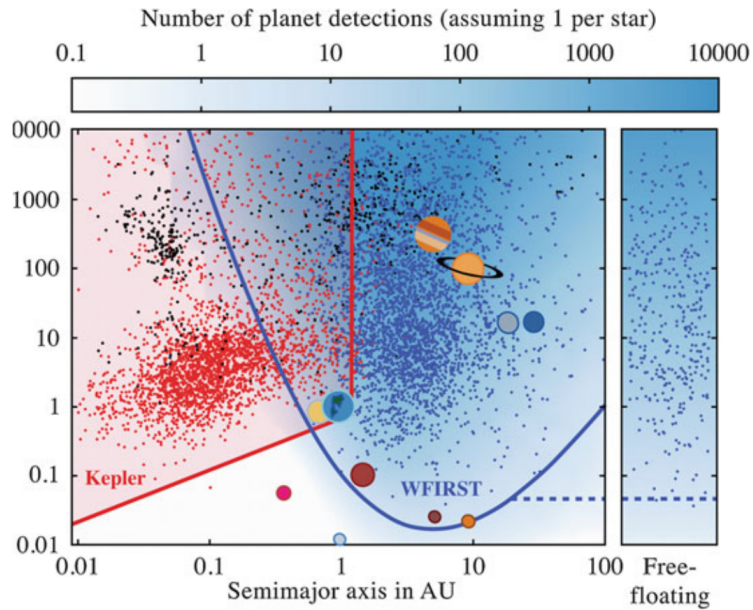


Figure 5.6: Future Roman telescope’s exoplanet detection range (previously named WFIRST), with Kepler range as reference. Y-axis is Planet Mass. Figure Credit: Batista [2018]

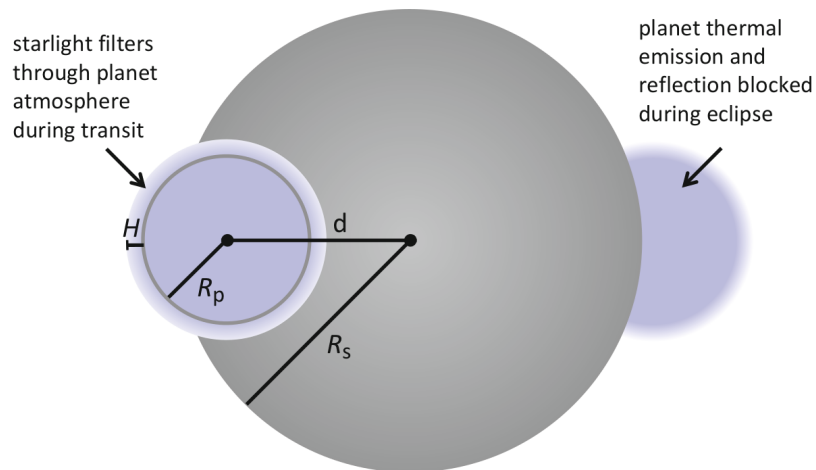


Figure 5.7: Transmission Spectroscopy Diagram: Transit and eclipse geometry showing how in more opaque atmosphere wavelengths (due to absorption by atoms or molecules), the planet blocks slightly more stellar flux. Figure Credit: Kreidberg [2018]

The future is bright as we design, develop, and launch the next generation of telescopes that will allow for greater clarity in exoplanet observations, and for the entire field of Astronomy & Astrophysics in general. This research has confidently shown that there are dedicated and competent people ready to stand on the shoulders of giants, and look deeper into and discover more of the wonders of the cosmos.

# Bibliography

- Kepler-20e the smallest exoplanet. URL <https://exoplanets.nasa.gov/resources/91/kepler-20e-the-smallest-exoplanet-artists-concept>.
- Plato revealing habitable worlds around solar-like stars, Apr 2017. URL [https://sci.esa.int/documents/33240/36096/1567260308850-PLATO\\_Definition\\_Study\\_Report\\_1\\_2.pdf](https://sci.esa.int/documents/33240/36096/1567260308850-PLATO_Definition_Study_Report_1_2.pdf).
- Exoplanet mission timeline, Dec 2020. URL <https://sci.esa.int/web/exoplanets/-/60649-exoplanet-mission-timeline>.
- Jamie Adkins. Tess - transiting exoplanet survey satellite, Jun 2016. URL <https://www.nasa.gov/tess-transiting-exoplanet-survey-satellite>.
- European Space Agency. Navigation, 2022. URL <https://www.cosmos.esa.int/web/gaia/release>.
- Adam Amara and Sascha P. Quanz. Pynpoint: an image processing package for finding exoplanets. *Monthly Notices of the Royal Astronomical Society*, 427:948–955, Dec 2012. ISSN 0035-8711. doi: 10.1111/j.1365-2966.2012.21918.x. ADS Bibcode: 2012MNRAS.427..948A.
- Virginie Batista. *Finding Planets via Gravitational Microlensing*. Jan 2018. doi: 10.1007/978-3-319-55333-7\_120. URL <https://ui.adsabs.harvard.edu/abs/2018haex.bookE.120B>. ADS Bibcode: 2018haex.bookE.120B.
- Jean-Philippe Berger, Richard Hook, and Information@eso.org. Light from all four vlt unit telescopes combined for the first time, Apr 2011. URL <https://www.eso.org/public/unitedkingdom/announcements/ann11021/>.
- J.-L. Beuzit, A. Vigan, D. Mouillet, K. Dohlen, R. Gratton, A. Boccaletti, J.-F. Sauvage, H. M. Schmid, M. Langlois, C. Petit, A. Baruffolo, M. Feldt, J. Milli, Z. Wahhaj, L. Abe, U. Anselmi, J. Antichi, R. Barette, J. Baudrand, P. Baudoz, A. Bazzon, P. Bernardi, P. Blanchard, R. Brast, P. Bruno, T. Buey, M. Carbillet, M. Carle, E. Cascone, F. Chapron, J. Char-ton, G. Chauvin, R. Claudi, A. Costille, V. De Caprio, J. de Boer, A. Delboulbé, S. Desidera, C. Dominik, M. Downing, O. Dupuis, C. Fabron, D. Fantinel, G. Farisato, P. Feautrier, E. Fedrigo, T. Fusco, P. Gigan, C. Ginski, J. Girard, E. Giro, D. Gisler, L. Gluck, C. Gry, T. Henning, N. Hubin, E. Hugot, S. Incorvaia, M. Jaquet, M. Kasper, E. Lagadec, A.-M. Lagrange, H. Le Coroller, D. Le Mignant, B. Le Ruyet, G. Lessio, J.-L. Lizon, M. Llored, L. Lundin, F. Madec, Y. Magnard, M. Marteaud, P. Martinez, D. Maurel, F. Ménard,

- D. Mesa, O. Möller-Nilsson, T. Moulin, C. Moutou, A. Origné, J. Parisot, A. Pavlov, D. Perret, J. Pragt, P. Puget, P. Rabou, J. Ramos, J.-M. Reess, F. Rigal, S. Rochat, R. Roelfsema, G. Rousset, A. Roux, M. Saisse, B. Salasnich, E. Santambrogio, S. Scuderi, D. Segransan, A. Sevin, R. Siebenmorgen, C. Soenke, E. Stadler, M. Suarez, D. Tiphène, M. Turatto, S. Udry, F. Vakili, L. B. F. M. Waters, L. Weber, F. Wildi, G. Zins, and A. Zurlo. Sphere: the exoplanet imager for the very large telescope. *Astronomy and Astrophysics*, 631:A155, Nov 2019. ISSN 0004-6361. doi: 10.1051/0004-6361/201935251.
- Henri Bonnet, Ralf Conzelmann, Bernhard Delabre, Robert Donaldson, Enrico Fedrigo, Norbert N. Hubin, Markus Kissler-Patig, Jean-Louis Lizon, Jerome Paufique, Silvio Rossi, Stefan Stroebele, and Sebastien Tordo. First light of sinfoni ao-module at vlt. In *Advancements in Adaptive Optics*, volume 5490, page 130–138. SPIE, Oct 2004. doi: 10.1117/12.551187. URL <https://www.spiedigitallibrary.org/conference-proceedings-of-spie/5490/0000/First-light-of-SINFONI-AO-module-at-VLT/10.1117/12.551187.full>.
- William Borucki, David Koch, Gibor Basri, Natalie Batalha, Timothy Brown, Douglas Caldwell, Jørgen Christensen-Dalsgaard, William Cochran, Edward Dunham, Thomas N. Gautier, John Geary, Ronald Gilliland, Jon Jenkins, Yoji Kondo, David Latham, Jack J. Lissauer, and David Monet. Finding earth-size planets in the habitable zone: the kepler mission. In Yi-Sui Sun, Sylvio Ferraz-Mello, and Ji-Lin Zhou, editors, *Exoplanets: Detection, Formation and Dynamics*, volume 249, page 17–24, May 2008. doi: 10.1017/S174392130801630X.
- F. Cantalloube, D. Mouillet, L. M. Mugnier, J. Milli, O. Absil, C. A. Gomez Gonzalez, G. Chauvin, J.-L. Beuzit, and A. Cornia. Direct exoplanet detection and characterization using the andromeda method: Performance on vlt/naco data. *Astronomy Astrophysics*, 582:A89, Oct 2015. ISSN 0004-6361, 1432-0746. doi: 10.1051/0004-6361/201425571.
- Eleazar Rodrigo Carrasco. Observando con gemini desde el óptico al infrarrojo medio. *Boletín de la Asociación Argentina de Astronomía La Plata Argentina*, 01 2009.
- Alexander Chaushev, Stephanie Sallum, Julien Lozi, Frantz Martinache, Jeffrey Chilcote, Tyler Groff, Olivier Guyon, N. Jeremy Kasdin, Barnaby Norris, and Andrew Skemer. Spectral differential imaging using kernel phase with charis/scexao: technique performance and current limitations. In Antoine Mérand, Stephanie Sallum, and Joel Sanchez-Bermudez, editors, *Optical and Infrared Interferometry and Imaging VIII*, volume 12183, page 121831L. SPIE, 2022. doi: 10.1117/12.2629558. URL <https://doi.org/10.1117/12.2629558>. Backup Publisher: International Society for Optics and Photonics.
- Jingjing Chen and David Kipping. Probabilistic Forecasting of the Masses and Radii of Other Worlds. , 834(1):17, January 2017. doi: 10.3847/1538-4357/834/1/17.
- Jeffrey Chilcote, Laurent Pueyo, Robert J. De Rosa, Jeffrey Vargas, Bruce Macintosh, Vanessa P. Bailey, Travis Barman, Brian Bauman, Sebastian Bruzzone, Joanna Bulger, Adam S. Burrows, Andrew Cardwell, Christine H. Chen, Tara Cotten, Daren Dillon, Rene Doyon, Zachary H. Draper, Gaspard Duchêne, Jennifer Dunn, Darren Erikson, Michael P. Fitzgerald, Katherine B. Follette, Donald Gavel, Stephen J. Goodsell, James R. Graham, Alexandra Z. Greenbaum, Markus Hartung, Pascale Hibon, Li-Wei Hung, Patrick Ingraham, Paul Kalas, Quinn Konopacky, James E. Larkin, Jérôme Maire, Franck Marchis, Mark S.

- Marley, Christian Marois, Stanimir Metchev, Maxwell A. Millar-Blanchaer, Katie M. Morzinski, Eric L. Nielsen, Andrew Norton, Rebecca Oppenheimer, David Palmer, Jennifer Pantienc, Marshall Perrin, Lisa Poyneer, Abhijith Rajan, Julien Rameau, Fredrik T. Rantakyro, Naru Sadakuni, Leslie Saddlemyer, Dmitry Savransky, Adam C. Schneider, Andrew Serio, Anand Sivaramakrishnan, Inseok Song, Remi Soummer, Sandrine Thomas, J. Kent Wallace, Jason J. Wang, Kimberly Ward-Duong, Sloane Wiktorowicz, and Schuyler Wolff. 1 to 2.4 micron near-ir spectrum of the giant planet  $\beta$  pictoris b obtained with the gemini planet imager. *The Astronomical Journal*, 153(4):182, Mar 2017. ISSN 1538-3881. doi: 10.3847/1538-3881/aa63e9. arXiv:1703.00011 [astro-ph].
- V. Christiaens, S. Casassus, O. Absil, F. Cantalloube, C. Gomez Gonzalez, J. Girard, R. Ramirez, B. Pairet, V. Salinas, D. J. Price, C. Pinte, S. P. Quanz, A. Jordán, D. Mawet, and Z. Wahhaj. Separating extended disc features from the protoplanet in pds 70 using vlt/sinfoni. *Monthly Notices of the Royal Astronomical Society*, 486:5819–5837, Jul 2019. ISSN 0035-8711. doi: 10.1093/mnras/stz1232. ADS Bibcode: 2019MNRAS.486.5819C.
- Jessie L. Christiansen. The rise and rise of exoplanets at the nasa exoplanet archive. In David S. Adler, Robert L. Seaman, and Chris R. Benn, editors, *Observatory Operations: Strategies, Processes, and Systems IX*, volume 12186, page 1218602. SPIE, 2022. doi: 10.1117/12.2646876. URL <https://doi.org/10.1117/12.2646876>. Backup Publisher: International Society for Optics and Photonics.
- R. U. Claudi, M. Turatto, R. G. Gratton, J. Antichi, M. Bonavita, P. Bruno, E. Cascone, V. De Caprio, S. Desidera, E. Giro, D. Mesa, S. Scuderi, K. Dohlen, J. L. Beuzit, and P. Puget. Sphere ifs: the spectro differential imager of the vlt for exoplanets search. 7014: 70143E, Jul 2008. doi: 10.1117/12.788366. ADS Bibcode: 2008SPIE.7014E..3EC.
- Alex De Koter. *Formation of Stars and Planetary Systems*. Astronomical Institute Anton Pannekoek University of Amsterdam P.O. Box 94249, 1090 GE Amsterdam, The Netherlands and Instituut voor Sterrenkunde, KU Leuven Celestijnenlaan 200D, 3001, Leuven, Belgium. Prof. dr.
- Hans J. Deeg and Roi Alonso. Transit photometry as an exoplanet discovery method. In *Handbook of Exoplanets*, pages 633–657. Springer International Publishing, 2018. doi: 10.1007/978-3-319-55333-7\_117. URL [https://doi.org/10.1007/978-3-319-55333-7\\_117](https://doi.org/10.1007/978-3-319-55333-7_117).
- Frank Eisenhauer, Roberto Abuter, Klaus Bickert, Fabio Biancat-Marchet, Henri Bonnet, Joar Brynnel, Ralf D. Conzelmann, Bernard Delabre, Robert Donaldson, Jacopo Farinato, Enrico Fedrigo, Reinhard Genzel, Norbert N. Hubin, Christof Iserlohe, Markus E. Kasper, Markus Kissler-Patig, Guy J. Monnet, Claudia Roehrl, Juergen Schreiber, Stefan Stroebele, Matthias Tecza, Niranjana A. Thatte, and Harald Weisz. Sinfoni: integral field spectroscopy at 50-milli-arcsecond resolution with the eso vlt. In *Instrument Design and Performance for Optical/Infrared Ground-based Telescopes*, volume 4841, page 1548–1561. SPIE, Mar 2003. doi: 10.1117/12.459468. URL <https://www.spiedigitallibrary.org/conference-proceedings-of-spie/4841/0000/SINFONI--integral-field-spectroscopy-at-50-milli-arcsecond-resolution/10.1117/12.459468.full>.
- information@eso.org European Southern Observatory. Beta pictoris as seen in infrared light - annotated, a. URL <https://www.eso.org/public/images/eso0842b/>.

- Operations Helpdesk European Southern Observatory. Eso science archive facility: Observational raw data query interface, b. URL [http://archive.eso.org/eso/eso\\_archive\\_main.html](http://archive.eso.org/eso/eso_archive_main.html).
- Webteam@eso.org European Southern Observatory. Esoreflex, Nov 2021a. URL <https://www.eso.org/sci/software/esoreflex/>.
- Webteam@eso.org European Southern Observatory. Instrument description, Jan 2021b. URL <https://www.eso.org/sci/facilities/paranal/instruments/sphere/inst.html#:~:text=The%20SPHERE%20integral%20field%20spectrograph,filters%20for%20accurate%20detector%20calibrations.>
- Fabo Feng, R. Paul Butler, Steven S. Vogt, Matthew S. Clement, C. G. Tinney, Kaiming Cui, Masataka Aizawa, Hugh R. A. Jones, J. Bailey, Jennifer Burt, B. D. Carter, Jeffrey D. Crane, Francesco Flammini Dotti, Bradford Holden, Bo Ma, Masahiro Ogihara, Rebecca Oppenheimer, S. J. O'Toole, Stephen A. Shectman, Robert A. Wittenmyer, Sharon X. Wang, D. J. Wright, and Yifan Xuan. 3-d selection of 167 sub-stellar companions to nearby stars. *The Astrophysical Journal Supplement Series*, 262(1):21, Sep 2022. ISSN 0067-0049, 1538-4365. doi: 10.3847/1538-4365/ac7e57. arXiv:2208.12720 [astro-ph].
- Rémi Flamary and Claude Aime. Optimization of starshades: Focal plane versus pupil plane. *Astronomy Astrophysics*, 569, Jul 2014. doi: 10.1051/0004-6361/201423680.
- Olivier Flasseur, Loïc Denis, Éric Thiébaud, and Maud Langlois. Paco asdi: an algorithm for exoplanet detection and characterization in direct imaging with integral field spectrographs. *Astronomy and Astrophysics*, 637:A9, May 2020. ISSN 0004-6361. doi: 10.1051/0004-6361/201937239.
- Olivier Flasseur, Samuel Thé, Loïc Denis, Éric Thiébaud, and Maud Langlois. Multispectral image reconstruction of faint circumstellar environments from high contrast angular spectral differential imaging (asdi) data. In Laura Schreiber, Dirk Schmidt, and Elise Vernet, editors, *Adaptive Optics Systems VIII*, volume 12185, page 121853U. SPIE, 2022. doi: 10.1117/12.2630362. URL <https://doi.org/10.1117/12.2630362>. Backup Publisher: International Society for Optics and Photonics.
- W. Freudling, M. Romaniello, D. M. Bramich, P. Ballester, V. Forchi, C. E. García-Dablo, S. Moehler, and M. J. Neeser. Automated data reduction workflows for astronomy. the eso reflex environment. *Astronomy and Astrophysics*, 559:A96, Nov 2013. ISSN 0004-6361. doi: 10.1051/0004-6361/201322494.
- Gaia Collaboration. VizieR Online Data Catalog: Gaia EDR3 (Gaia Collaboration, 2020). *VizieR Online Data Catalog*, art. I/350, November 2020.
- Clio Gielen. The hermes spectrograph, Jan 2023. URL <https://fys.kuleuven.be/ster/instruments/the-hermes-spectrograph>. People involved: Gert Raskin, Saskia Prins, Wim Pessemier, Florian Merges, Hans Van Winckel, Christoffel Waelkens.
- Tiffany Glassman, Amy Lo, Jonathan Arenberg, Webster Cash, and Charley Noecker. Starshade scaling relations. *Proc SPIE*, 7440, Aug 2009. doi: 10.1117/12.825033.

- +61 2 9372 4310 (fax); jurisdiction=Commonwealth abstractNote=(UCB) with IRCAL on the Lick Observatory 3m Graham, James R; corporateName=CSIRO Australia Telescope National Facility; scheme=AGLSTERMS.AglsAgent address=PO Box 76 Epping NSW 1710 Australia; contact=+61 2 9372 4100 (phone), Jul 2022. URL [https://www.atnf.csiro.au/outreach/education/senior/astrophysics/adaptive\\_optics.html](https://www.atnf.csiro.au/outreach/education/senior/astrophysics/adaptive_optics.html).
- Natalia Guerrero. Tess - transiting exoplanet survey satellite, Sep 2022. URL <https://tess.mit.edu/>.
- O. Guyon, E. A. Pluzhnik, M. J. Kuchner, B. Collins, and S. T. Ridgway. Theoretical limits on extrasolar terrestrial planet detection with coronagraphs. *The Astrophysical Journal Supplement Series*, 167(1):81–99, nov 2006. doi: 10.1086/507630. URL <https://doi.org/10.1086%2F507630>.
- Carlos A Gómez. Applications of pca and low-rank plus sparse decompositions in high-contrast exoplanet imaging. Feb 2016.
- M Haehnelt and L. Pasquini. E-elt programme codex phase a - iac.es, Jan 2010. URL [https://www.iac.es/proyecto/codex/media/codex\\_files/C001\\_Science\\_Case.pdf](https://www.iac.es/proyecto/codex/media/codex_files/C001_Science_Case.pdf).
- Markus Janson, Thomas Henning, Sascha P. Quanz, Ruben Asensio-Torres, Lars Buchhave, Oliver Krause, Enric Pallé, and Alexis Brandeker. Occulter to earth: prospects for studying earth-like planets with the e-elt and a space-based occulter. *Experimental Astronomy*, Aug 2021. ISSN 0922-6435, 1572-9508. doi: 10.1007/s10686-021-09792-y. URL <https://link.springer.com/10.1007/s10686-021-09792-y>.
- Michele Johnson. Mission overview, Apr 2015. URL [http://www.nasa.gov/mission\\_pages/kepler/overview/index.html](http://www.nasa.gov/mission_pages/kepler/overview/index.html).
- S. Kiefer, A. J. Bohn, S. P. Quanz, M. Kenworthy, and T. Stolker. Spectral and angular differential imaging with SPHERE/IFS. Assessing the performance of various PCA-based approaches to PSF subtraction. *Astronomy & Astrophysics*, 652:A33, August 2021. ISSN 0004-6361, 1432-0746. doi: 10.1051/0004-6361/202140285. URL <http://arxiv.org/abs/2106.05278>. arXiv: 2106.05278.
- Laura Kreidberg. Exoplanet atmosphere measurements from transmission spectroscopy and other planet star combined light observations. In *Handbook of Exoplanets*, pages 2083–2105. Springer International Publishing, 2018. doi: 10.1007/978-3-319-55333-7\_100. URL [https://doi.org/10.1007%2F978-3-319-55333-7\\_100](https://doi.org/10.1007%2F978-3-319-55333-7_100).
- A.-M. Lagrange, A. Boccaletti, M. Langlois, G. Chauvin, R. Gratton, H. Beust, S. Desidera, J. Milli, M. Bonnefoy, A. Cheetham, M. Feldt, M. Meyer, A. Vigan, B. Biller, M. Bonavita, J.-L. Baudino, F. Cantalloube, M. Cudel, S. Daemgen, P. Delorme, V. D’Orazi, J. Girard, C. Fontanive, J. Hagelberg, M. Janson, M. Keppler, T. Koypitova, R. Galicher, J. Lannier, H. Le Coroller, R. Ligi, A.-L. Maire, D. Mesa, S. Messina, A. Müller, S. Peretti, C. Perrot, D. Rouan, G. Salter, M. Samland, T. Schmidt, E. Sissa, A. Zurlo, J.-L. Beuzit, D. Mouillet, C. Dominik, T. Henning, E. Lagadec, F. Ménard, H.-M. Schmid, M. Turatto, S. Udry, A. J. Bohn, B. Charnay, C. A. Gomez Gonzales, C. Gry, M. Kenworthy, Q. Kral, C. Mordasini, C. Moutou, G. van der Plas, J. E. Schlieder, L. Abe, J. Antichi, A. Baruffolo, P. Baudoz, J. Baudrand, P. Blanchard, A. Bazzon, T. Buey, M. Carbillet,

- M. Carle, J. Charton, E. Cascone, R. Claudi, A. Costille, A. Deboulbe, V. De Caprio, K. Dohlen, D. Fantinel, P. Feautrier, T. Fusco, P. Gigan, E. Giro, D. Gisler, L. Gluck, N. Hubin, E. Hugot, M. Jaquet, M. Kasper, F. Madec, Y. Magnard, P. Martinez, D. Maurer, D. Le Mignant, O. Möller-Nilsson, M. Llored, T. Moulin, A. Origné, A. Pavlov, D. Perret, C. Petit, J. Pragt, J. Szulagyi, and F. Wildi. Post-conjunction detection of beta pictoris b with vlt/sphere. *Astronomy Astrophysics*, 621:L8, Jan 2019. ISSN 0004-6361, 1432-0746. doi: 10.1051/0004-6361/201834302.
- A. M. Lagrange, P. Rubini, M. Nowak, S. Lacour, A. Grandjean, A. Boccaletti, M. Langlois, P. Delorme, R. Gratton, J. Wang, O. Flasseur, R. Galicher, Q. Kral, N. Meunier, H. Beust, C. Babusiaux, H. Le Coroller, P. Thebault, P. Kervella, A. Zurlo, A.-L. Maire, Z. Wahhaj, A. Amorim, R. Asensio-Torres, M. Benisty, J. P. Berger, M. Bonnefoy, W. Brandner, F. Cantalloube, B. Charnay, G. Chauvin, E. Choquet, Y. Clénet, V. Christiaens, V. Coudé du Foresto, P. T. de Zeeuw, S. Desidera, G. Duvert, A. Eckart, F. Eisenhauer, F. Galland, F. Gao, P. Garcia, R. Garcia Lopez, E. Gendron, R. Genzel, S. Gillessen, J. Girard, J. Hagelberg, X. Haubois, T. Henning, G. Heissel, S. Hippler, M. Horrobin, M. Janson, J. Kammerer, M. Kenworthy, M. Keppler, L. Kreidberg, V. Lapeyrère, J.-B. Le Bouquin, P. Léna, A. Mérand, S. Messina, P. Mollière, J. D. Monnier, T. Ott, G. Otten, T. Paumard, C. Paladini, K. Perraut, G. Perrin, L. Pueyo, O. Pfuhl, L. Rodet, G. Rodriguez-Coira, G. Rousset, M. Samland, J. Shangguan, T. Schmidt, O. Straub, C. Straubmeier, T. Stolker, A. Vigan, F. Vincent, F. Widmann, J. Woillez, and the GRAVITY Collaboration. Unveiling the beta pictoris system, coupling high contrast imaging, interferometric, and radial velocity data. *Astronomy Astrophysics*, 642:A18, Oct 2020. ISSN 0004-6361, 1432-0746. doi: 10.1051/0004-6361/202038823.
- Rainer Lenzen, Markus Hartung, Wolfgang Brandner, Gert Finger, Norbert N. Hubin, Francois Lacombe, Anne-Marie Lagrange, Matthew D. Lehnert, Alan F. M. Moorwood, and David Mouillet. Naos-conica first on sky results in a variety of observing modes. 4841:944–952, Mar 2003. doi: 10.1117/12.460044. ADS Bibcode: 2003SPIE.4841..944L.
- B. Loyt. Photographie de la couronne solaire en dehors des eclipses. 1931, a. *Compt. Rend.* 191, 834-837.
- B. Loyt. A study of the solar corona and prominences without eclipses. 1939, b. *Mon. Not. Roy. Astron. Soc.* 99, 580-594.
- Fabien Malbet and Alessandro Sozzetti. Astrometry as an Exoplanet Discovery Method. In Hans J. Deeg and Juan Antonio Belmonte, editors, *Handbook of Exoplanets*, page 196. 2018. doi: 10.1007/978-3-319-55333-7\_196.
- C Marois, C Correia, R Galicher, et al. Adaptive optics systems iv. In *Proc. SPIE*, volume 9148, page 91480, 2014.
- Christian Marois, David Lafreniere, Rene Doyon, Bruce Macintosh, and Daniel Nadeau. Angular Differential Imaging: A Powerful High-Contrast Imaging Technique. *The Astrophysical Journal*, 641(1):556–564, April 2006. ISSN 0004-637X, 1538-4357. doi: 10.1086/500401. URL <https://iopscience.iop.org/article/10.1086/500401>.
- Michel Mayor and Didier Queloz. A Jupiter-mass companion to a solar-type star. , 378(655): 355–359, November 1995. doi: 10.1038/378355a0.

- D. Mesa, R. Gratton, A. Zurlo, A. Vigan, R. U. Claudi, M. Alberi, J. Antichi, A. Baruffolo, J.-L. Beuzit, A. Boccaletti, M. Bonnefoy, A. Costille, S. Desidera, K. Dohlen, D. Fantinel, M. Feldt, T. Fusco, E. Giro, T. Henning, M. Kasper, M. Langlois, A.-L. Maire, P. Martinez, O. Moeller-Nilsson, D. Mouillet, C. Moutou, A. Pavlov, P. Puget, B. Salasnich, J.-F. Sauvage, E. Sissa, M. Turatto, S. Udry, F. Vakili, R. Waters, and F. Wildi. Performance of the vlt planet finder sphere - ii. data analysis and results for ifs in laboratory. *Astronomy Astrophysics*, 576:A121, Apr 2015. ISSN 0004-6361, 1432-0746. doi: 10.1051/0004-6361/201423910.
- NASA. the NASA Exoplanet Archive, 2022. This research has made use of the NASA Exoplanet Archive, which is operated by the California Institute of Technology, under contract with the National Aeronautics and Space Administration under the Exoplanet Exploration Program.
- F. et. al Ochsenbein. *The\_vizier\_database\_of\_astrophysical\_catalogues*.
- Marc Ollivier, Françoise Roques, Fabienne Casoli, Thérèse Encrenaz, and Franck Selsis. *Detection Methods*, page 21–68. Astronomy And Astrophysics Library. Springer, Berlin, Heidelberg, 2009. ISBN 978-3-540-75748-1. doi: 10.1007/978-3-540-75748-1\_2. URL [https://doi.org/10.1007/978-3-540-75748-1\\_2](https://doi.org/10.1007/978-3-540-75748-1_2).
- Fabian Pedregosa, Gaël Varoquaux, Alexandre Gramfort, Vincent Michel, Bertrand Thirion, Olivier Grisel, Mathieu Blondel, Peter Prettenhofer, Ron Weiss, Vincent Dubourg, Jake Vanderplas, Alexandre Passos, David Cournapeau, Matthieu Brucher, Matthieu Perrot, and Édouard Duchesnay. Scikit-learn: Machine learning in python. *Journal of Machine Learning Research*, 12(85):2825–2830, 2011. ISSN 1533-7928.
- Michael Perryman. *The Exoplanet Handbook*. 2018.
- Michael Perryman, Joel Hartman, Gáspár Á. Bakos, and Lennart Lindegren. ASTROMETRIC EXOPLANET DETECTION WITH GAIA/i. *The Astrophysical Journal*, 797(1):14, nov 2014. doi: 10.1088/0004-637x/797/1/14. URL <https://doi.org/10.1088/0004-637x/797/1/14>.
- Sebastián Pérez, Sebastián Marino, Simon Casassus, Clément Baruteau, Alice Zurlo, Christian Flores, and Gaël Chauvin. Upper limits on protolunar disc masses using alma observations of directly-imaged exoplanets. *Monthly Notices of the Royal Astronomical Society*, 488(1):1005–1011, Sep 2019. ISSN 0035-8711, 1365-2966. doi: 10.1093/mnras/stz1775. arXiv:1906.11774 [astro-ph].
- Gert Raskin, Christian Schwab, Bart Vandenbussche, Joris De Ridder, Cyprien Lanthermann, Jesus Pérez Padilla, Andrew Tkachenko, Hugues Sana, Pierre Royer, Saskia Prins, Leen Decin, Denis Defrère, Jacob Pember, David Atkinson, Alistair Glasse, Don Pollacco, Giovanna Tinetti, Manuel Güdel, Julian Stürmer, Ignasi Ribas, Alexis Brandeker, Lars Buchhave, Samuel Halverson, Gerardo Avila, Johan Morren, and Hand Van Winckel. Marvel, a four-telescope array for high-precision radial-velocity monitoring. (arXiv:2012.08121), Dec 2020. doi: 10.48550/arXiv.2012.08121. URL <http://arxiv.org/abs/2012.08121>. arXiv:2012.08121 [astro-ph].
- C. Reylé, K. Jardine, P. Fouqué, J. A. Caballero, R. L. Smart, and A. Sozzetti. The 10 parsec sample in the gaia era, Apr 2021. URL <https://gruze.org/10pc/The10pcSample.ReadMe.txt>.

- George R. Ricker, Joshua N. Winn, Roland Vanderspek, David W. Latham, Gaspar A. Bakos, Jacob L. Bean, Zachory K. Berta-Thompson, Timothy M. Brown, Lars Buchhave, Nathaniel R. Butler, R. Paul Butler, William J. Chaplin, David Charbonneau, Jorgen Christensen-Dalsgaard, Mark Clampin, Drake Deming, John Doty, Nathan De Lee, Courtney Dressing, E. W. Dunham, Michael Endl, Francois Fressin, Jian Ge, Thomas Henning, Matthew J. Holman, Andrew W. Howard, Shigeru Ida, Jon Jenkins, Garrett Jernigan, John Asher Johnson, Lisa Kaltenegger, Nobuyuki Kawai, Hans Kjeldsen, Gregory Laughlin, Alan M. Levine, Douglas Lin, Jack J. Lissauer, Phillip MacQueen, Geoffrey Marcy, P. R. McCullough, Timothy D. Morton, Norio Narita, Martin Paegert, Enric Palle, Francesco Pepe, Joshua Pepper, Andreas Quirrenbach, S. A. Rinehart, Dimitar Sasselov, Bun'ei Sato, Sara Perryman., Alessandro Sozzetti, Keivan G. Stassun, Peter Sullivan, Andrew Szentgyorgyi, Guillermo Torres, Stephane Udry, and Joel Villaseñor. The transiting exoplanet survey satellite. *Journal of Astronomical Telescopes, Instruments, and Systems*, 1(1):014003, Oct 2014. ISSN 2329-4124. doi: 10.1117/1.JATIS.1.1.014003. arXiv:1406.0151 [astro-ph].
- Gerard Rousset, Francois Lacombe, Pascal Puget, Norbert N. Hubin, Eric Gendron, Thierry Fusco, Robin Arsenault, Julien Charton, Philippe Feautrier, Pierre Gigan, Pierre Y. Kern, Anne-Marie Lagrange, Pierre-Yves Madec, David Mouillet, Didier Rabaud, Patrick Rabou, Eric Stadler, and Gerard Zins. Naos, the first ao system of the vlt: on-sky performance. 4839: 140–149, Feb 2003. doi: 10.1117/12.459332. ADS Bibcode: 2003SPIE.4839..140R.
- M. Samland, P. Mollière, M. Bonnefoy, A.-L. Maire, F. Cantalloube, A. C. Cheetham, D. Mesa, R. Gratton, B. A. Biller, Z. Wahhaj, J. Bouwman, W. Brandner, D. Melnick, J. Carson, M. Janson, T. Henning, D. Homeier, C. Mordasini, M. Langlois, S. P. Quanz, R. van Boekel, A. Zurlo, J. E. Schlieder, H. Avenhaus, J.-L. Beuzit, A. Boccaletti, M. Bonavita, G. Chauvin, R. Claudi, M. Cudel, S. Desidera, M. Feldt, T. Fusco, R. Galicher, T. G. Kopytova, A.-M. Lagrange, H. Le Coroller, P. Martinez, O. Moeller-Nilsson, D. Mouillet, L. M. Mugnier, C. Perrot, A. Sevin, E. Sissa, A. Vigan, and L. Weber. Spectral and atmospheric characterization of 51 eridani b using vlt/sphere. *Astronomy Astrophysics*, 603:A57, Jul 2017. ISSN 0004-6361, 1432-0746. doi: 10.1051/0004-6361/201629767.
- M. Samland, T. D. Brandt, J. Milli, P. Delorme, and A. Vigan. Spectral cube extraction for the vlt/sphere ifs - open-source pipeline with full forward modeling and improved sensitivity. *Astronomy Astrophysics*, 668:A84, Dec 2022. ISSN 0004-6361, 1432-0746. doi: 10.1051/0004-6361/202244587.
- S. Seager. *Exoplanets*. 2010. URL <https://ui.adsabs.harvard.edu/abs/2010exop.book.....S>.
- B. A. Smith and R. J. Terile. A circumstellar disk around beta pictoris. *Science*, 226: 1421–1424, Dec 1984. ISSN 0036-8075. doi: 10.1126/science.226.4681.1421. ADS Bibcode: 1984Sci...226.1421S.
- Rémi Soummer, Laurent Pueyo, and James Larkin. Detection and characterization of exoplanets and disks using projections on karhunen-loève eigenimages. *The Astrophysical Journal*, 755: L28, Aug 2012. ISSN 0004-637X. doi: 10.1088/2041-8205/755/2/L28. ADS Bibcode: 2012ApJ...755L..28S.

- David J. Stevenson. Jupiter's interior as revealed by juno. *Annual Review of Earth and Planetary Sciences*, 48:465–489, May 2020. ISSN 0084-6597. doi: 10.1146/annurev-earth-081619-052855. ADS Bibcode: 2020AREPS..48..465S.
- T. Stolker, M. J. Bonse, S. P. Quanz, A. Amara, G. Cugno, A. J. Bohn, and A. Boehle. Pynpoint: a modular pipeline architecture for processing and analysis of high-contrast imaging data. *Astronomy Astrophysics*, 621:A59, Jan 2019. ISSN 0004-6361, 1432-0746. doi: 10.1051/0004-6361/201834136.
- O. Struve. Proposal for a project of high-precision stellar radial velocity work. *The Observatory*, 72:199–200, October 1952.
- Jean Surdej. Birefringent achromatic phase shifters for nulling interferometry, 2021. URL [http://www.aeos.ulg.ac.be/upload/Heidelberg\\_mawet.pdf](http://www.aeos.ulg.ac.be/upload/Heidelberg_mawet.pdf).
- ESA PLATO Science Advisory Team and Conny Aerts. plato. URL <https://sci.esa.int/web/plato>.
- Webteam@eso.org The European Southern Observatory, Feb 2019. URL <https://www.eso.org/sci/facilities/paranal/instruments/sphere/overview.html>.
- A. Vigan, Cecile Gry, Graeme Salter, Dino Mesa, Derek Homeier, C. Moutou, and F. Allard. High-contrast imaging of sirius a with vlt/sphere: Looking for giant planets down to one astronomical unit. *Monthly Notices of the Royal Astronomical Society*, 454, 08 2015. doi: 10.1093/mnras/stv1928.
- A. Wolszczan and D. A. Frail. A planetary system around the millisecond pulsar PSR1257 + 12. , 355(6356):145–147, January 1992. doi: 10.1038/355145a0.

# Appendices

# Appendix A

## Additional Results Plots and Figures

All calculations, code, and plots are freely available at <https://github.com/dcpetit/Astronomy>. You can obtain the FITS files from ESO and the flow described in the introduction or emailing me directly at: [david.petit@student.kuleuven.be](mailto:david.petit@student.kuleuven.be).

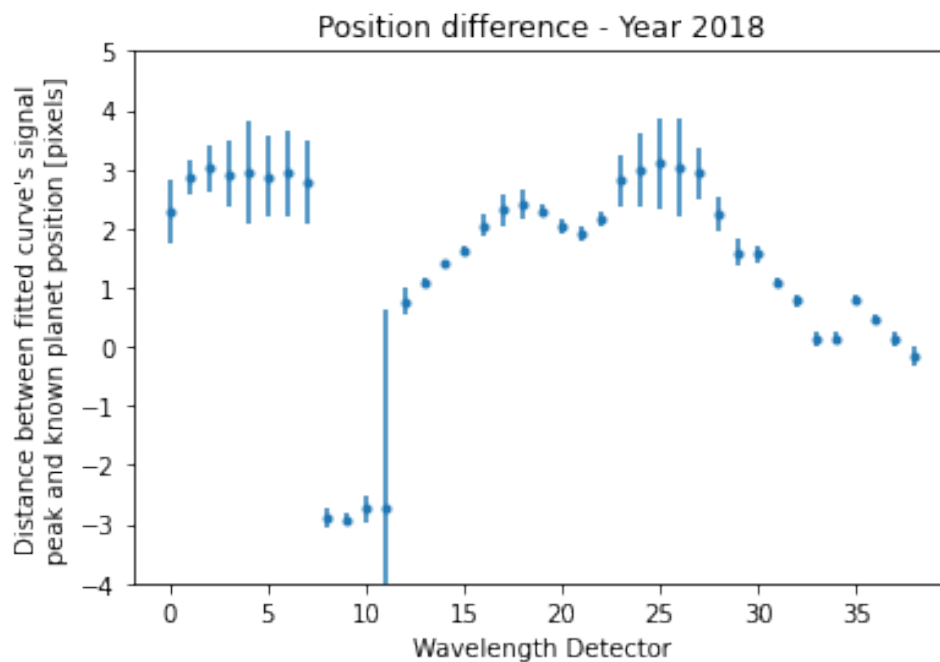


Figure A.1: Difference between fitted smooth curve peak models with literature value position of Beta Pic b for the 2018 observation.

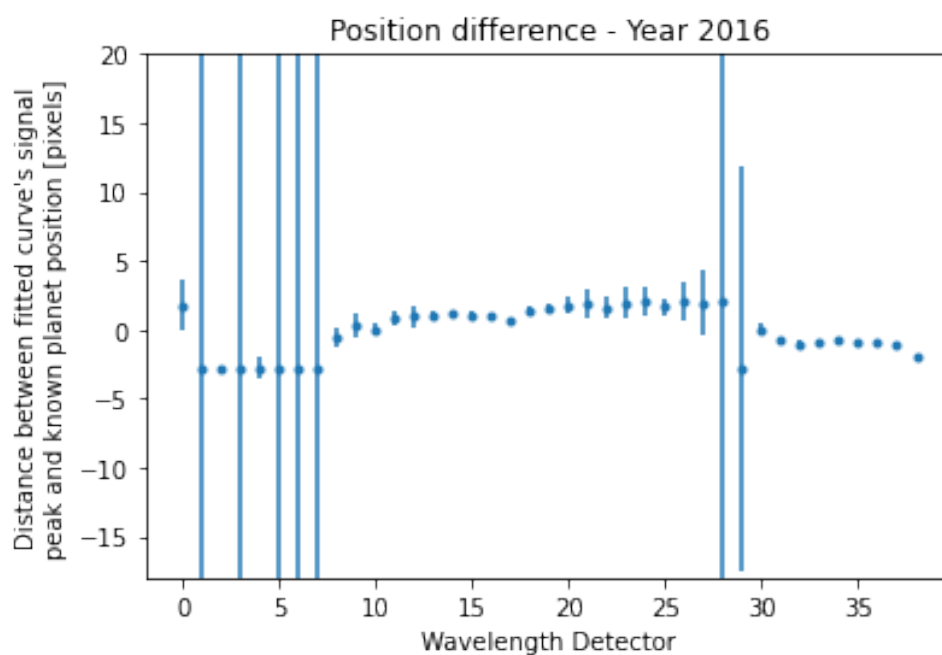


Figure A.2: Difference between fitted smooth curve peak models with literature value position of Beta Pic b for the 2016 observation.

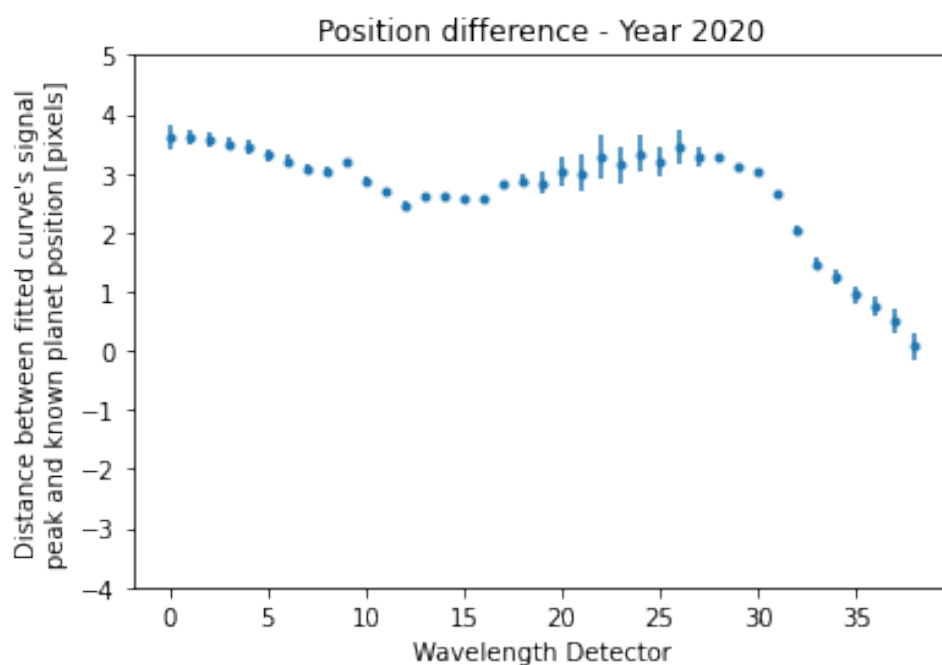


Figure A.3: Difference between fitted smooth curve peak models with literature value position of Beta Pic b for the 2020 observation.

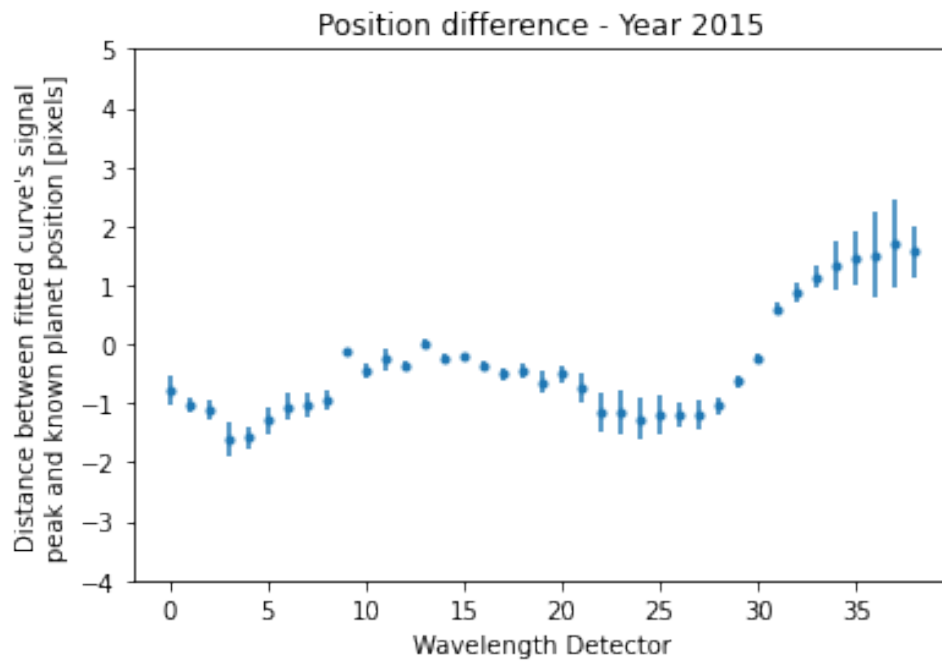


Figure A.4: Difference between fitted smooth curve peak models with literature value position of Beta Pic b for the 2015 observation.

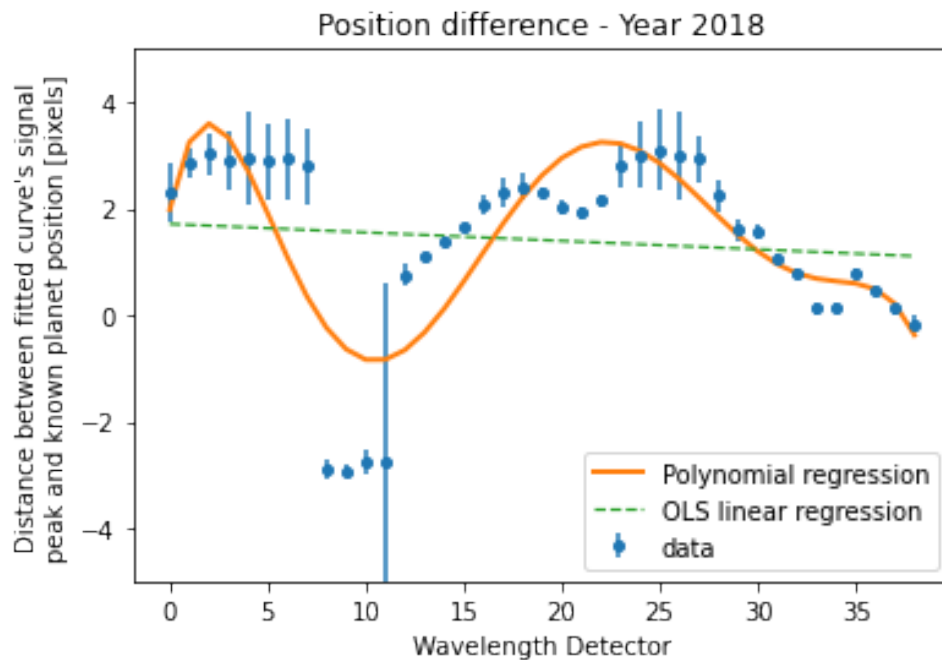


Figure A.5: 6th order polynomial regression of 2018 observation. Difference between fitted smooth curve peak models with literature value position of Beta Pic b for the 2018 observation.

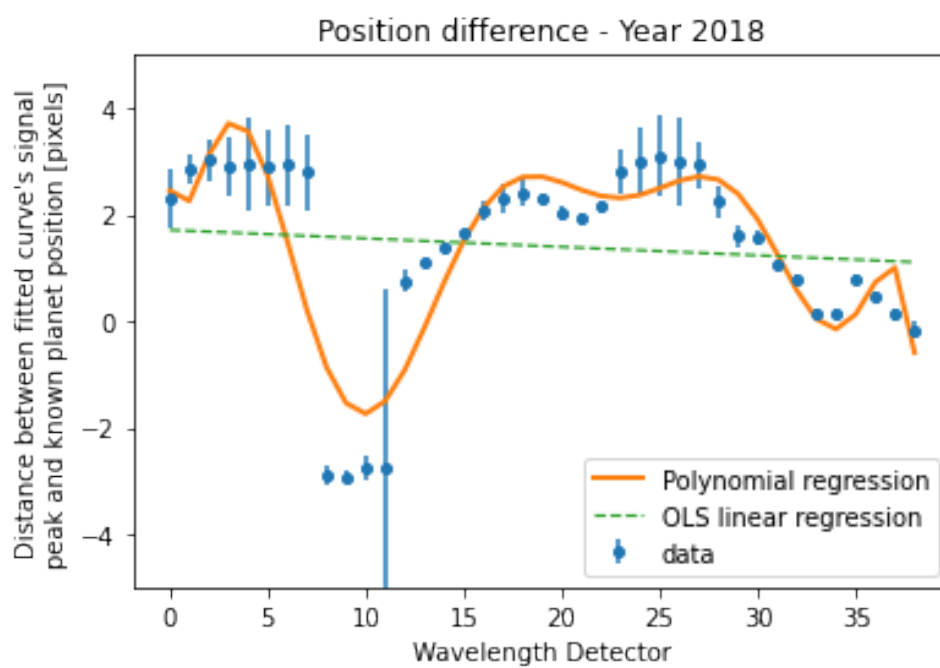


Figure A.6: 9th order polynomial regression of 2018 observation. Difference between fitted smooth curve peak models with literature value position of Beta Pic b for the 2018 observation.

# Appendix B

## Additional Exoplanet Detection Method Diagrams

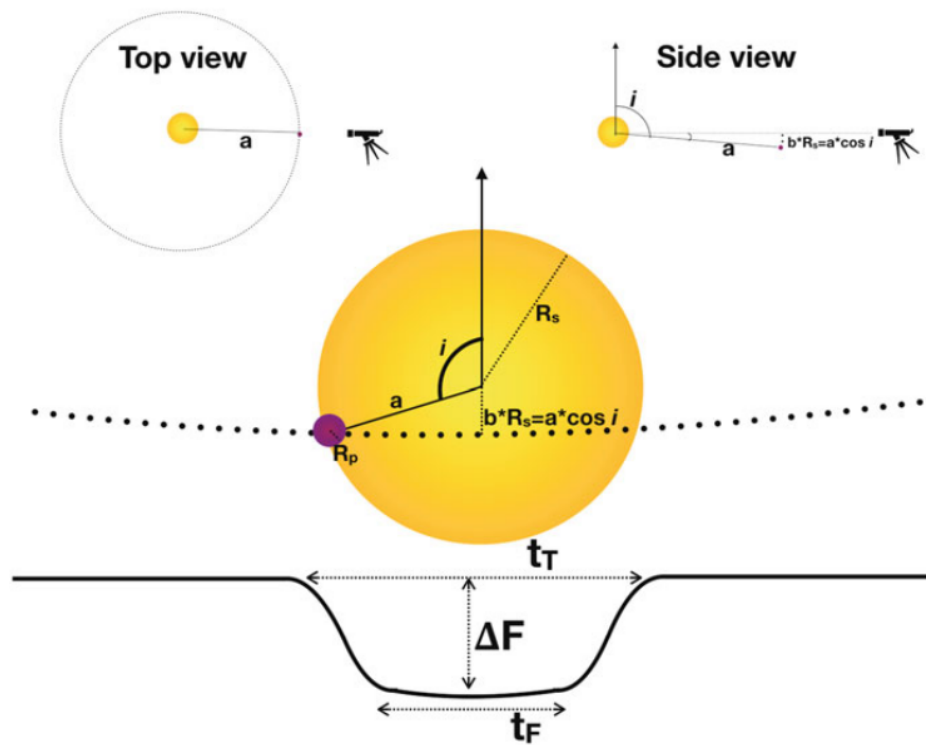


Figure B.1: Diagram of the Transit method of exoplanetary detection. Figure Credit: Deeg and Alonso [2018]

# Appendix C

## ALMA Based Research

Knowledge was obtained while attending the 2022 ALMA Science Archive School in Bologna, Italy over the summer. Though a real pertinent connection between the material learned there and the work done here was not made; general information about the Beta Pictoris system and surrounding debris (circumstellar) disk was learned in a high level of detail. One result of this advanced training is Figure C.1. The oval or cigar shape is due to the edge-on orientation

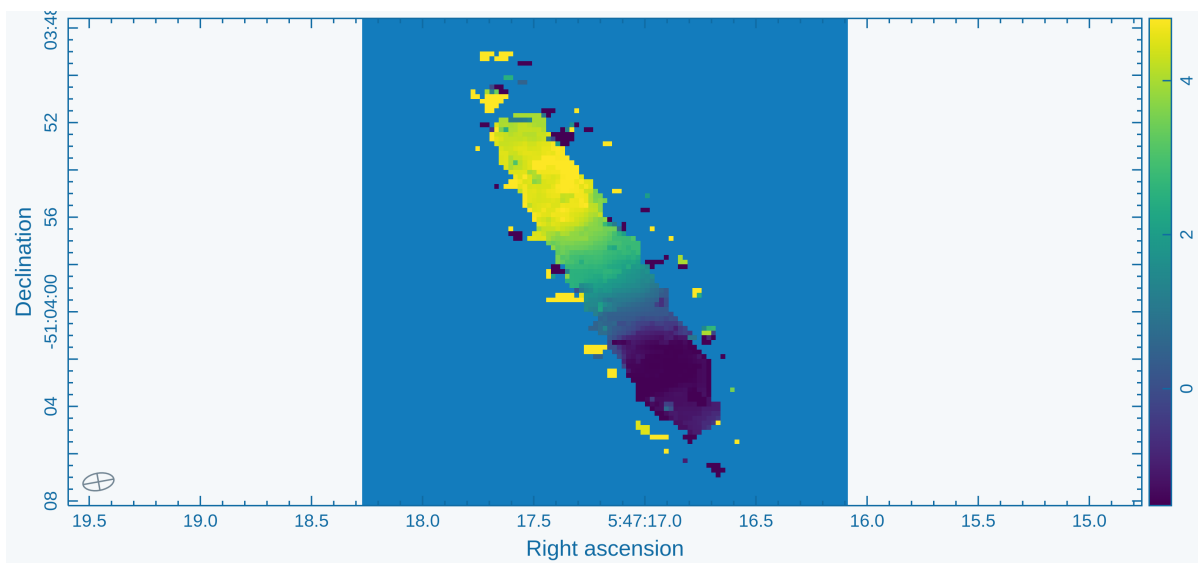


Figure C.1: Radial Velocity heat map of the visible material of the Beta Pictoris system. This paper makes use of ALMA data

of the system from our line of sight. The changing color gradient demonstrates the relative orbit of the debris disk, as well as hints at the redshift of the entire system. The yellow tip near the top left corner is increasing in radius or distance to us observers, while the dark portion in the lower right corner is moving towards us. Because the yellow (and green, aqua, and blue) region(s) have positive radial velocities and are substantially more massive than the purple region, we can intuitively grasp that the center of the system (and the whole system if considered for a long enough time duration) is moving away from us. This is supported by the literature as well [Ochsenbein].

*This paper makes use of the following ALMA data: ADS/JAO.ALMA#2011.0.01234.S. ALMA is a partnership of ESO (representing its member states), NSF (USA) and NINS (Japan), together with NRC (Canada), MOST and ASIAA (Taiwan), and KASI (Republic of Korea), in cooperation with the Republic of Chile. The Joint ALMA Observatory is operated by ESO, AUI/NRAO and NAOJ.*



**Institute of Astronomy**

Celestijnenlaan 200D bus 2401

3001 LEUVEN, BELGIË

tel. + 32 16 37 46 28

fax + 32 16 32 79 99

[www.kuleuven.be](http://www.kuleuven.be)

